2024

The characterization and nanomechanical properties of microstructurally complex systems

Kerry Ann Baker
University of Kentucky, kaba265@uky.edu
Digital Object Identifier: https://doi.org/10.13023/etd.2024.03

STUDENT AGREEMENT:

I represent that my thesis or dissertation and abstract are my original work. Proper attribution has been given to all outside sources. I understand that I am solely responsible for obtaining any needed copyright permissions. I have obtained needed written permission statement(s) from the owner(s) of each third-party copyrighted matter to be included in my work, allowing electronic distribution (if such use is not permitted by the fair use doctrine) which will be submitted to UKnowledge as Additional File.

I hereby grant to The University of Kentucky and its agents the irrevocable, non-exclusive, and royalty-free license to archive and make accessible my work in whole or in part in all forms of media, now or hereafter known. I agree that the document mentioned above may be made available immediately for worldwide access unless an embargo applies.

I retain all other ownership rights to the copyright of my work. I also retain the right to use in future works (such as articles or books) all or part of my work. I understand that I am free to register the copyright to my work.

REVIEW, APPROVAL AND ACCEPTANCE

The document mentioned above has been reviewed and accepted by the student's advisor, on behalf of the advisory committee, and by the Director of Graduate Studies (DGS), on behalf of the program; we verify that this is the final, approved version of the student's thesis including all changes required by the advisory committee. The undersigned agree to abide by the statements above.

Kerry Ann Baker, Student

Dr. T. John Balk, Major Professor

Dr. Fuqian Yang, Director of Graduate Studies

THE CHARACTERIZATION AND NANOMECHANICAL PROPERTIES OF MICROSTRUCTURALLY COMPLEX SYSTEMS

DISSERTATION

A dissertation submitted in partial fulfillment of the
requirements for the degree of Doctor of Philosophy in the
College of Engineering
at the University of Kentucky

By
Kerry Ann Baker
Lexington, Kentucky
Director: Dr. T. John Balk, Professor of Materials Engineering
Lexington, Kentucky
2023

ABSTRACT OF DISSERTATION

THE CHARACTERIZATION AND NANOMECHANICAL PROPERTIES OF MICROSTRUCTURALLY COMPLEX SYSTEMS

Since the dawn of civilization, the use of metals has played an integral role in the evolution of human society. Over the years, and with the introduction of new engineering and science, we have learned how to combine metals to create new metallic systems. We have expanded our understanding of dealloying and chemical reactions, and, in doing so, we created nanoporous metals. Our use of metals has evolved from basic alloys such as bronze and steel to more complex alloys such as multi-principal element alloys. Nanoporous gold is an advanced metallic system that can be created through the dealloying process. Nanoporous gold has a high surface area-to-volume ratio, which, combined with its material properties, makes it a good candidate for catalytic, sensing, and capacitance applications. These applications may require the nanoporous gold to be exposed to elevated temperatures. As elevated temperatures affect nanoporous gold's structure and ligament size, this work studies the coarsening of nanoporous gold. In order to test the mechanical behavior of nanoporous gold via nanoindentation, the optimal ratio of the indent spacing to indent depth (*d/h*) must be found. It was found that for nanoporous gold with different microstructures, the optimal *d/h* ratio was 10. The coarsening of nanoporous gold was performed *in-situ* with an SEM heating stage to note any changes within the microstructure. The rate of growth was found to be higher than predicted by previous work due to the influence of the electron beam while coarsening. Multi-principal element alloys have high-temperature resistance, increased harness, and complex microstructures that make them useful in numerous applications, such as jet engines, submarines, and projectiles. Their complex microstructure can result in multi-phase compositions that have various mechanical behaviors which influence the overall bulk mechanical behavior. This work will focus on the mechanical behavior of W-Mo-Fe-Ni alloys and the individual phases found within this system. This dissertation explores the characteristics and mechanical behavior of newer, complex metallic systems such as nanoporous gold and multi-principal element alloys.

KEYWORDS: [Nanoporous, Multi-Principal Element Alloys, Nanoindentation, Mechanical Properties, Microstructure]

Kerry Ann Baker
(Name of Student)

11/28/2023
Date

THE CHARACTERIZATION AND NANOMECHANICAL PROPERTIES OF MICROSTRUCTURALLY COMPLEX SYSTEMS

By
Kerry Ann Baker

Dr. T. John Balk
Director of Dissertation

Dr. Fuqian Yang
Director of Graduate Studies

11/28/2023
Date

ACKNOWLEDGMENTS

I would like to start by thanking my advisor, Dr. T. John Balk, for his guidance and support throughout the course of my research and Ph.D.

I would also like to thank my committee members, Dr. Matthew Beck, Dr. Paul Rottmann, and Dr. Todd Hastings for their time and assistance.

I would like to acknowledge the financial support provided by the U.S. Department of Energy, Office of Science, Basic Energy Sciences, under Award # DE-SC0019402 and by the Army Research Laboratory under Award # 3210001940

I would also like to acknowledge that portions of this work were performed in part at the U.K. Electron Microscopy Center, a member of the National Nanotechnology Coordinated Infrastructure (NNCI), which is supported by the National Science Foundation (NNCI-2025075).

Many thanks to my fellow lab partner and colleagues who helped support this work. This work could not have been completed without the help of Alexandra Allamon, Alyssa Stubbers, Mujan Seif, Michael Detisch, David Starr, Riya Barua, and Zahidur Rahman.

Finally, thank you to my family for their continued love and support during this journey.

TABLE OF CONTENTS

LIST OF TABLES

LIST OF FIGURES

CHAPTER 1. INTRODUCTION

The use of metals can be traced back to the Neolithic Era, circa 6000 B.C., with evidence of gold and copper objects found at dig sites in various locations including Iran, Mesopotamia, Syria, Egypt, and Turkey [1, 2]. During this era, we know that copper was used for making fishing hooks, jewelry, and weapons. However, the uses for gold found remain relatively unknown [1]. Historians also refer to the Neolithic Era as the South-East European Copper Age because of the prolific use of copper [1]. It was during the Bronze Age, circa 1600 B.C., following the Copper Age, that the use of alloys, or a combination of two or more metallic elements, was noted [1]. Bronze, an alloy system composed of copper and tin, was used for weapons such as daggers and tools such as axes [1]. These items were most likely forged utilizing primitive smelting techniques and furnaces and molds to combine copper and tin [1]. Through trial and error, the appropriate mixture of tin and copper was perfected for the various uses of bronze [3]. The Iron Age began approximately 400 years after the Bronze Age and, with it, the newfound ability to generate furnace temperatures hot enough to melt iron at 1537 °C [2]. This temperature vastly exceeded the melting point of copper at 1083 °C. The enhanced capability to generate even higher temperature furnaces led to the Steel Age [4]. It has been many years since the creation of the most basic of alloys during the Bronze Age, but with the dawn of modern science, vast improvements in metallurgy have been and will continue to be made [3]. Even though metallurgy has been around for centuries, it was not until the beginning of the 17th century that science and technology began to flourish, and significant improvements to metallurgy were made [3]. Interestingly, though, creating newer and more complex,

metallic systems only requires the basic alloying principles discovered centuries ago. It is the more recent knowledge of how to design metallic systems for specific properties that allows for the creation of more advanced and specialized metallic systems.

Nanoporous gold is one such specialized metallic system, fabricated through dealloying, a process developed by the Incans hundreds of years ago [5, 6]. Dealloying removes the less noble elements from an alloy through corrosion or etching. [5]. In the case of nanoporous gold, gold is combined with a less noble element, such as silver, which is then etched away [5]. The Incans used copper-gold alloys, which they dealloyed for the illusion of pure gold. This process is aptly known as depletion gilding [6, 7]. Depletion gilding was also independently developed in Europe in the Medieval Ages by artisans [6]. Dealloying processes significantly improved in the 1960s, pioneered by Pickering and Swann [6, 8-10]. Additional work performed in the late 1970s by Forty and Durkin employed transmission electron microscopy (TEM) to obtain micrographs of dealloyed gold-silver alloys [5, 11, 12]. The use of TEM revealed the porous structure of a gold-silver alloy after it was placed in an acid bath [5]. Today, nanoporous gold is used in different technical applications such as catalysis, sensing, and filtration [6].

While alloys have existed since the Bronze Age, alloys with multiple principal elements were only introduced some 40 years ago. [13]. There have been many definitional and terminology disputes regarding these more complex systems. The following are some of the terms that have been used in the past 40 years to describe these complex alloy systems: multi-principal element alloys (MPEAs), high entropy alloys (HEAs), medium entropy alloys (MEAs), baseless alloys, and complex concentrated alloys (CCAs) [13]. For this dissertation, the term multi-principal alloy (MPEA) is used as it is broadly used and

generally accepted. Some of the precursory work that led to the development of MPEAs was conducted in 1981 by a research group headed by Brian Cantor [14]. This work was the genesis of the alloy that today is often referred to as the Cantor Alloy [14]. This alloy system is commonly composed of equiatomic CoCrFeMnNi forming a single-phase FCC solid solution [14]. In 2004, Yeh introduced the more complex idea of MPEAs which deviate from equiatomic alloys [15]. Cantor and Yeh's innovations are notably more advanced than the earliest bronze alloy's simplistic mixing of copper with a small amount of tin. The research of MPEAs is still in its infancy. Because MPEAs are comprised of multiple principal elements, the research and testing necessary to establish relationships between their composition and properties is extremely difficult [13]. MPEAs include a wide range of alloy systems and, therefore, have the potential for use in many specific, niche applications. For example, MPEAs are designed for high-temperature applications, low-density structural materials, improved strength, and more [13].

With the aid of microstructural characterization and nanomechanical behavior testing, the work presented in this dissertation furthers the understanding of microstructurally complex systems by thoroughly investigating the structure and properties of np-Au and W-Mo-Fe-Ni alloys, an MPEA system. The main objectives of this work will be to (1) provide an in-depth look into to *in-situ* coarsening of np-Au (2) find the optimal indent spacing to indent depth when using instrumented nanoindentation for np-Au (3) provide understanding into the mechanical properties of W-Mo-Fe-Ni alloys individual phases with the aid of mechanical property mapping.

CHAPTER 2. METHODOLOGIES

This section describes the various methodologies used throughout this dissertation for the characterization and testing of mechanical properties of np-Au and MPEA samples.

2.1 Scanning Electron Microscopy

Scanning electron microscopy (SEM) was used to capture micrographs of various metallic systems to showcase distinctive structures and phases. SEM can magnify features up to 1,000,000x and provide a more intricate grey-scale image than optical microscopy (OM), as OM only reaches a magnification of 1000x [16, 17]. SEMs are composed of the following components, [16] which can be seen in Figure 2-1:

1. Electron source (*i.e.*, electron gun)
2. Electron column which has two or more electromagnetic lenses
3. Deflection system which consists of a scan coil
4. Electron detectors for secondary and backscattered electrons
5. Sample chamber with high vacuum capability
6. Computer control system for imaging and beam control

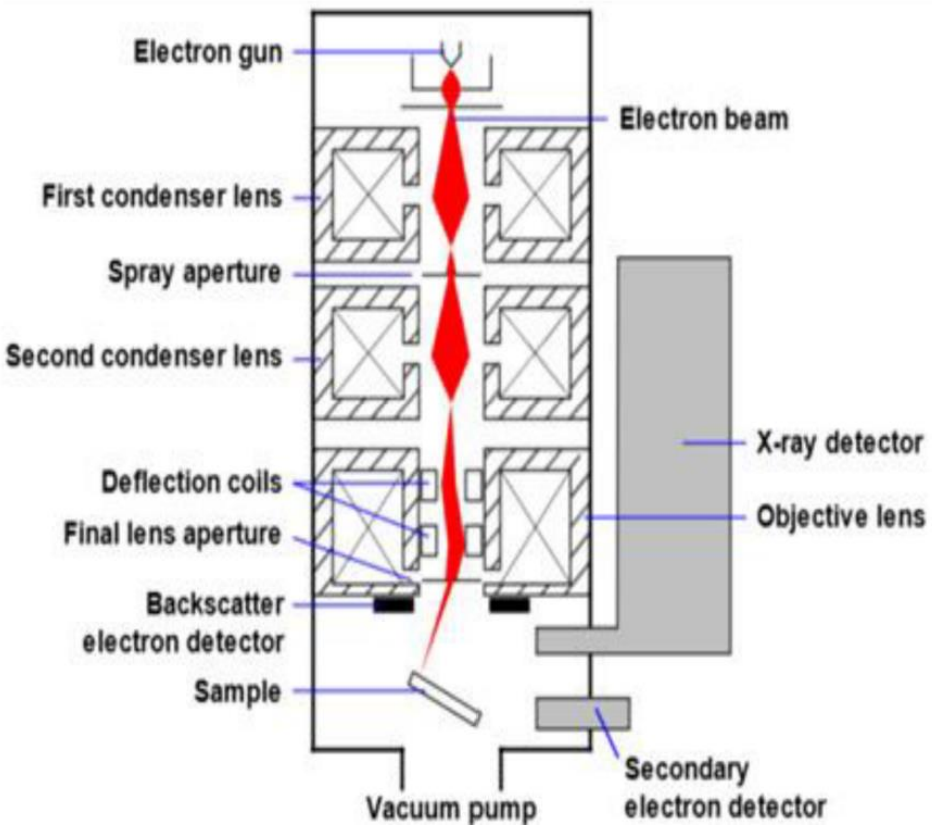

Figure 2-1 Schematic of scanning electron microscope with components labeled (reproduced from [16]).

The SEM detectors (labeled as the backscatter electron detector and the secondary electron detector in Figure 2-1) detect the signal from electrons scattered by the electron beam interacting with the sample and generate an image [16, 17]. This image, or micrograph, which shows the shape, size, and surface texture of the sample, is created when the scattered secondary electrons (SE) and backscatter electrons (BSE) are captured by the detectors [17]. Regions where the detector receives more electrons appear bright and regions with fewer electrons appear dark, thus creating a grey-scale image. The electron gun produces the electron beam where the accelerating voltage of the beam applied to the sample can be controlled [18]. A low accelerating voltage will provide information of the sample surface while a high accelerating voltage will penetrate deeper and be rich in details

below the surface [16]. SEs are created by inelastic scattering as the electron beam contacts the sample [18, 19]. Elastic scattering produces BSE as the electron beam undergoes scattering before escaping the sample's surface [18-20]. The scattering of the BSE allows the electrons to penetrate deeper into the surface than SE penetration (Figure 2-2).

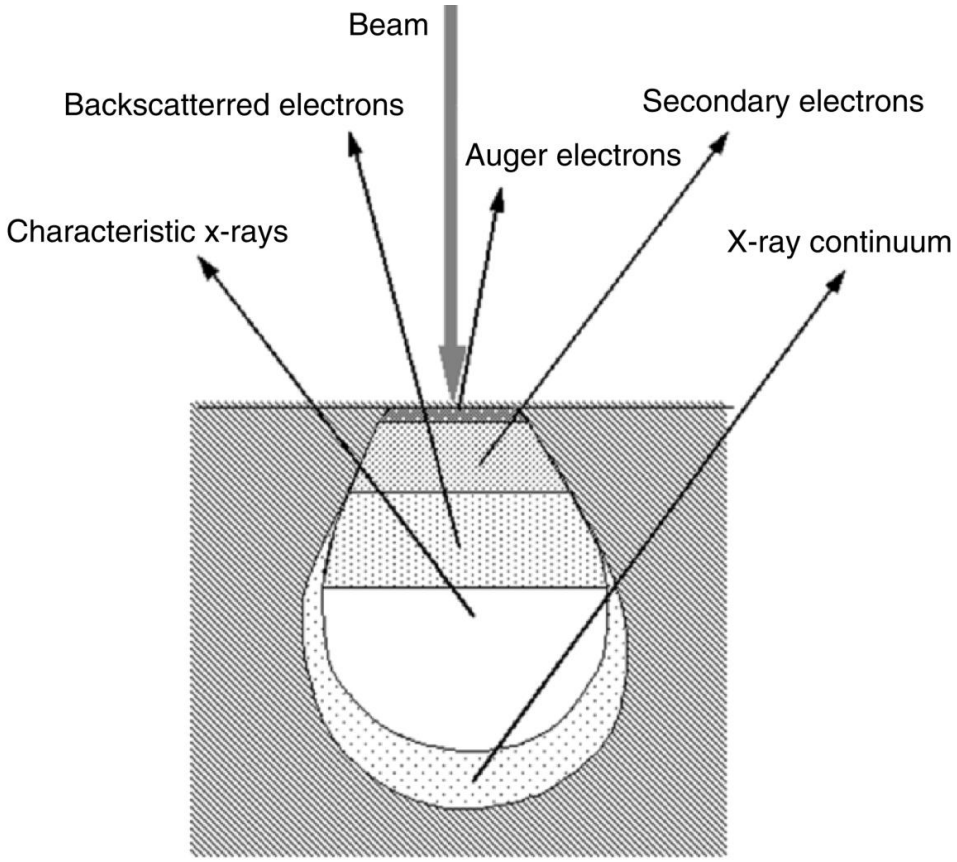

Figure 2-2 Amount of penetration depth of the electron beam through a sample and the type of electrons and X-rays that can be emitted from a sample (reproduced from [17]).

For most SEMs, the spot size produced by the electron beam and compressed by lenses is typically less than 10 nm, with a penetration depth up to 1 μm [16]. The electron beam scans the sample to generate electron signals, which produce an image [16]. Because there are different types of electrons, the SEM has various modes that utilize the different electron signals captured to generate distinct micrographs. SE mode is typically used to

denote differences in topography as inelastic scattering occurs near the surface. Surface features are distinguished based on the variations in surface topography.

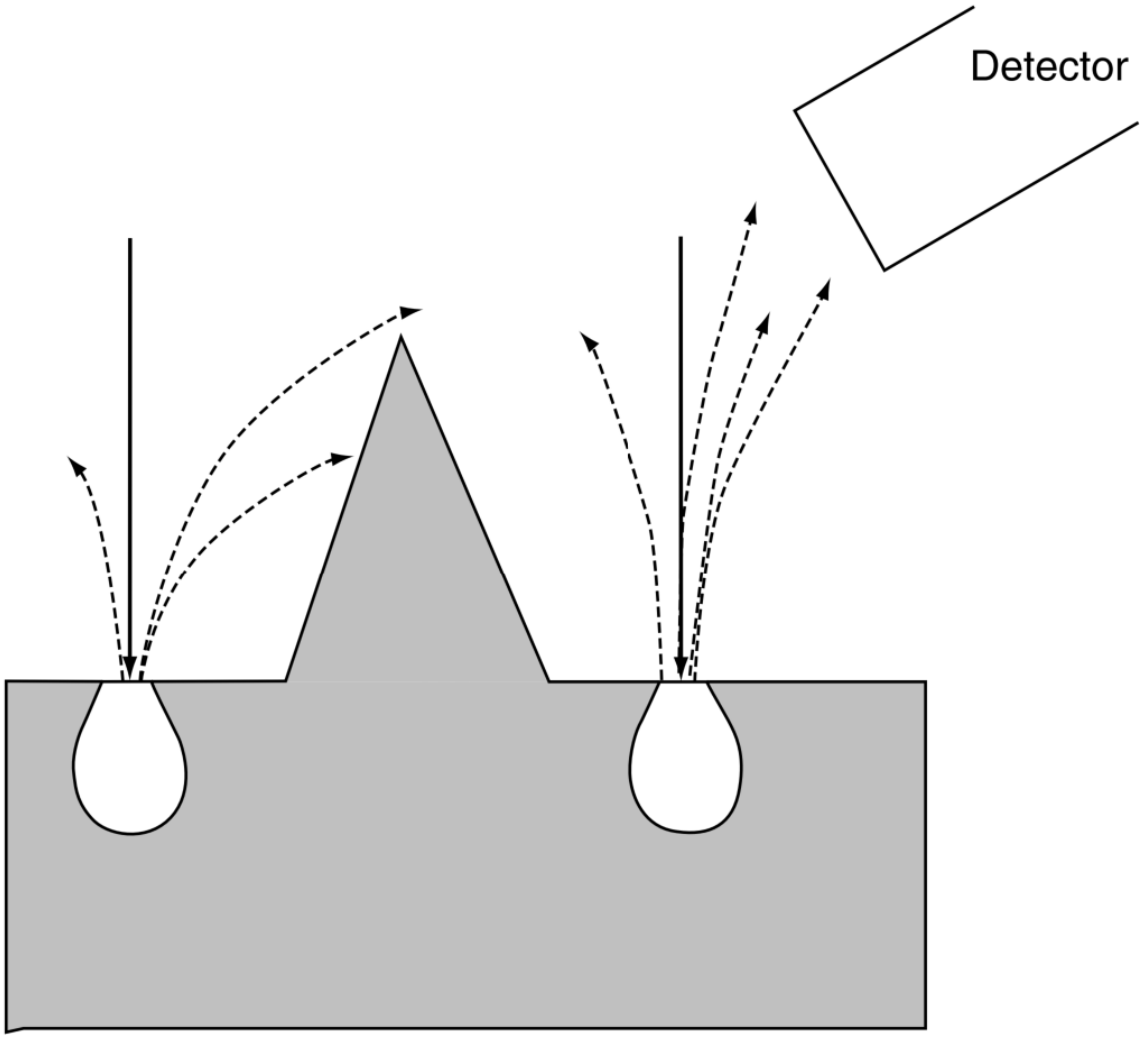

Figure 2-3 Schematic of the effect of surface topography and position of the electron detector on SE detection (reproduced from [17]).

Figure 2-3 shows the electron beam in solid black and the scattered electrons as dotted black lines. Because the SE detector is to the right of the sample and there is a mound in the sample's topography, electrons from the left-hand side of the mound do not reach the detector. This causes the region on the right-hand side of the mound to appear brighter

as more scattered electrons make it to the detector and thus increase the signal strength from that area [17].

BSE mode produces micrographs that show additional contrast based on elements distinguished by their atomic number (Z). Elements with a higher Z value appear brighter due to the additional BSE that escapes the surface [18]. The increase in BSE results from the electron beam's inability to penetrate as deep into the surface of elements with a higher Z, which results in a higher chance of electrons scattering and exiting the surface [18].

The high-resolution imaging presented in this dissertation was performed on an FEI Quanta 250 SEM with a field emission gun and on a FEI Helios Nanolab 660 with dual beams at the University of Kentucky College of Engineering's Electron Microscopy Center (EMC).

To further understand the properties of a sample, the SEM micrograph can be enhanced by employing additional qualitative and quantitative techniques, such as X-ray energy dispersive spectroscopy (EDS), discussed in Section 2.2.

2.2 Elemental Analysis

X-ray energy dispersive spectroscopy (EDS) is an SEM technique that enables an elemental analysis of samples based on their characteristic X-rays, as seen in Figure 2-2 [16, 18, 20]. Characteristic X-rays are generated when enough energy is used to "knock-out" an electron in an atom to create a "free" electron, resulting in an ionized atom [20]. The ionized atom results in an unstable electron configuration, and in order to restore equilibrium, electrons from a higher level fill the empty inner level. The resulting energy differences in the electron shells generate the characteristic X-ray [20, 21]. EDS spectrums are displayed as the intensity of the characteristic X-ray versus the X-ray energy range [20].

Each element has a specific energy related to (i) the characteristic X-ray and (ii) which electron shell the electron was knocked out of [19]. Since most EDS software includes a database of characteristic X-ray energies for all elements, the EDS software can detect which elements are present based on the energy peak position. Once the elemental peaks are identified, a quantitative analysis can be made based on the ratio of peak intensities [18].

EDS was performed with an Oxford EDX detector for elemental analysis attached to the FEI Helios Nanolab 660 in this study.

2.3 Nanoindentation

Nanoindentation is a technique that allows for the probing of mechanical properties of samples on the sub-micron scale [22]. Nanoindentation is similar to classic indentation techniques such as Vickers, Brinell, and Rockwell, however, in comparison, the load applied to the sample is smaller. In classic indentation techniques, the load can be within the range of hundreds of newtons, whereas nanoindentation rarely exceeds one newton. Nanoindentation results in a much smaller contact area between the tip and the sample, enabling the characterization of small volumes of material.

Developed in 1992, the Oliver-Pharr method for nanoindentation serves as the basis for the many more advanced methodologies devised in subsequent decades [22]. Nanoindentation uses the Poisson's ratio, applied load, tip area, and initial unloading stiffness to calculate the hardness and elastic modulus of a sample [22, 23]. Using a combination of Equation 2-1 and 2-2, the reduced elastic modulus can be found given the stiffness (*dP/dh*) and Poisson's ratio of both the indenter tip and sample:

$$S = \frac{dP}{dh} = \frac{2}{\sqrt{\pi}} E_r \sqrt{A} \qquad \text{Equation 2-1}$$

$$\frac{1}{E_r} = \frac{(1-\nu^2)}{E} + \frac{(1-\nu_i^2)}{E_i} \qquad \text{Equation 2-2}$$

where $S=dP/dh$, is the stiffness of the upper portion of the unloading data (see Figure 2-4), E_r is the reduced modulus, A is the area of the tip in contact with the sample during elastic contact, E is the Young's modulus, and ν is the Poisson's ratio [22]. The subscript i indicates parameters for the indenter.

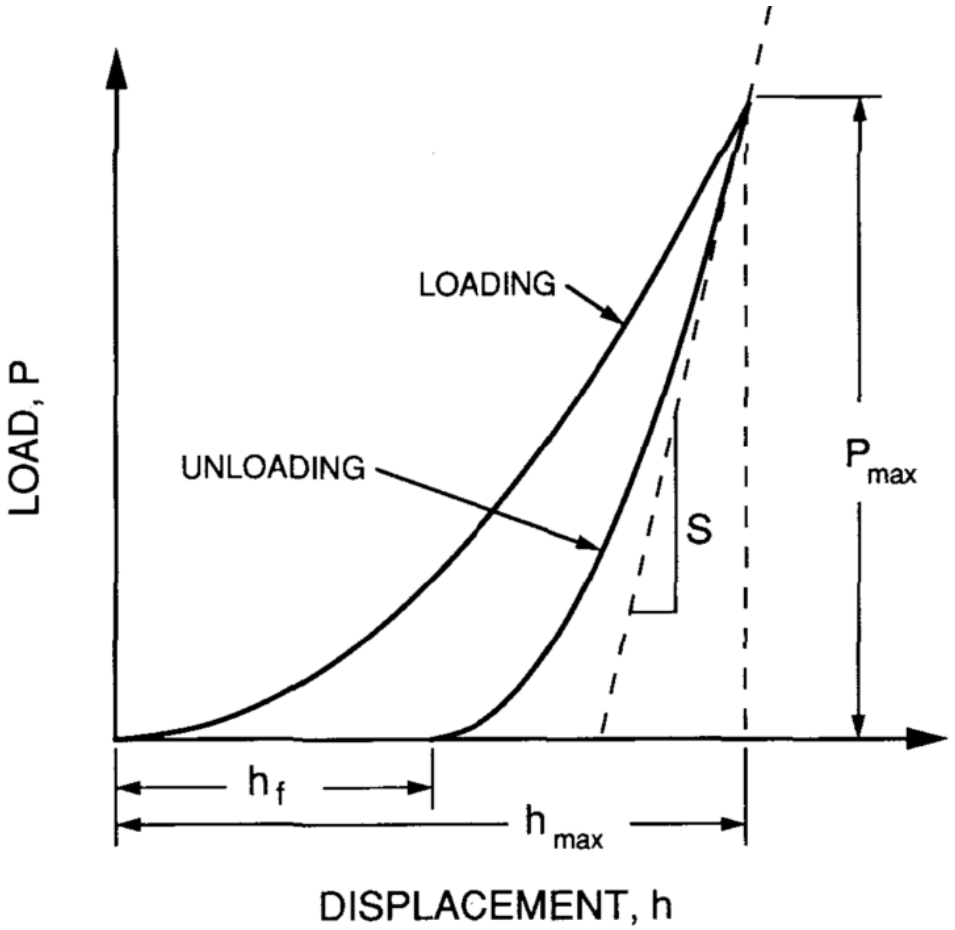

Figure 2-4 Schematic of a load-displacement curve created during nanoindentation (reproduced from [22]).

Note that in Figure 2-4, P_{max} is the maximum load at the maximum displacement (h_{max}), S denotes the stiffness during the initial part of the unloading curve and h_f is the

final depth. By understanding the loading and unloading curve, Equation 2-2 can be rewritten in terms of finding the reduced modulus, *E* (Equation 2-3) which was derived by Sneddon [24].

$$E_r = \frac{\sqrt{\pi}}{2}\frac{S}{\sqrt{A}} \qquad \text{Equation 2-3}$$

Figure 2-5 shows how the surface changes as the indenter probes the sample's surface. It is important to note which depth (*h*) value is referenced as there is the total depth (*h*), contact depth (h_c), final depth (h_f), and displacement of the surface surrounding the tip contact (h_s).

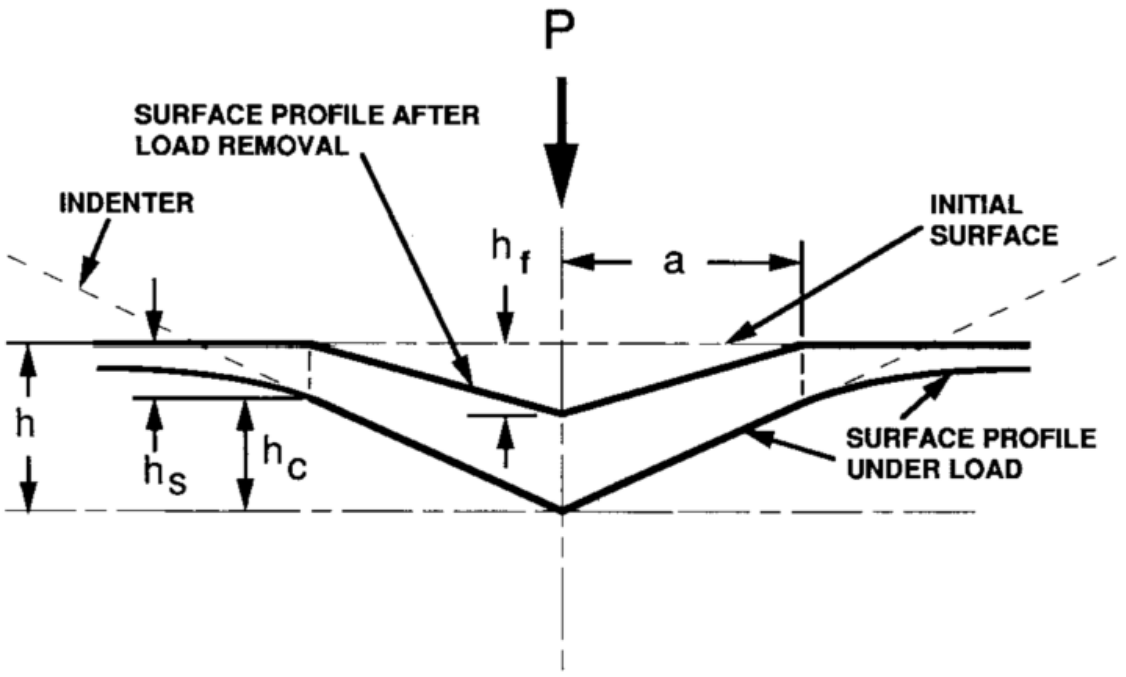

Figure 2-5 Schematic of the cross-sectional view of an indenter tip penetrating the surface of a sample (reproduced from [22]).

The change in the total depth (*h*) versus the final depth (h_f) is due to the elastic and plastic deformation experienced in the sample. When a load is applied to the sample, the tip indents to a total depth (*h*). The total depth (*h*) is the combination of the contact depth (h_c) and the displacement of the surface at the perimeter of the contact (h_s), as shown below.

$$h = h_c + h_s \qquad \text{Equation 2-4}$$

During unloading, the elastic deformation is recovered, and only the plastic deformation remains. This results in a change in the indent depth. The final depth after elastic recovery is h_f. The hardness of the sample can be determined by the maximum load and tip contact area [22]:

$$H = \frac{P_{max}}{A} \qquad \text{Equation 2-5}$$

where H is the hardness. The contact area (A) is determined by the geometry of the indenter tip and the depth of contact (h_c). The geometry of the tip can be described by an area function that relates the cross-sectional area of the tip to the total depth (h) [22]. For experiments presented in this dissertation, a Berkovich tip, a three-sided pyramid with an area-to-depth function similar to a Vickers tip, was utilized [22]. The area function of a Berkovich tip is outlined in Equation 2-6. The tip area was calibrated using a standard sample, fused silica, as its mechanical properties are well-known, [22]:

$$A(h_c) = 24.5h_c \qquad \text{Equation 2-6}$$

$$A(h_c) = \mathrm{C}_0 h_c + C_1 h_c^1 + C_2 h_c^{1/2} + C_3 h_c^{1/4} + \cdots C_8 h_c^{1/128} \qquad \text{Equation 2-7}$$

where C_0 through C_8 are constants fitted from indents on fused silica [22]. Note that Equation 2-6 is the area function for a perfect Berkovich tip and Equation 2-7 includes constants that are used to fit the imperfections or blunting of the tip [22]. Refer to Appendix 2 for the tip contact area and coefficients of the Berkovich tip used in this work. Figure 2-6 shows a schematic representation of a nanoindenter apparatus.

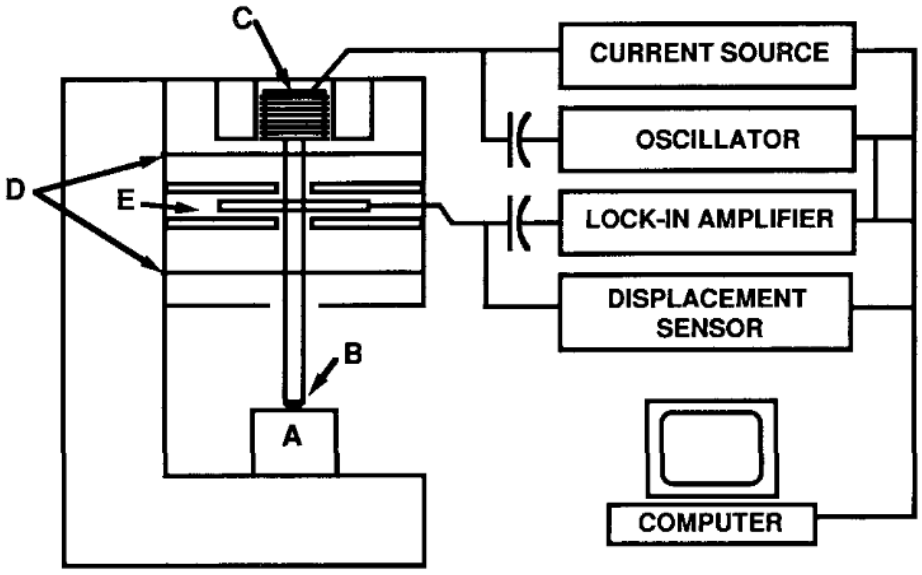

Figure 2-6 Schematic representation of a KLA nanoindenter with the following components: (A) sample, (B) indenter, (C) load application coil, (D) indentation column guide springs, and (E) capacitive displacement sensor (reproduced from [22].

The application coil, guide springs, and displacement sensor (labeled as *A*, *B*, *C*, and *D*, respectively, in Figure 2-6), are required to employ continuous stiffness measurements (CSM) while indenting. CSM is a dynamic technique that can measure mechanical properties as a continuous function of depth [25]. CSM is accomplished by slightly oscillating the tip during indentation [22]. In order to ensure that only elastic deformation occurred during the tip oscillation, the oscillation's amplitude was kept small enough to ensure that the deformation process did not significantly impact the sample during indentation.

Note that the 10% rule should be applied when indenting thin films. That is, the total indent depth should not exceed 10% of the film thickness [26]. Otherwise, the size of the elastic modulus zone will become larger than the film thickness and encapsulate the substrate (Figure 2-7). In 1953, Bückle introduced the 10% rule of thumb for indenting

thicker metallic films with indents on the micro scale [27]. This general rule has been found to also apply to thin film and nanoindentation.

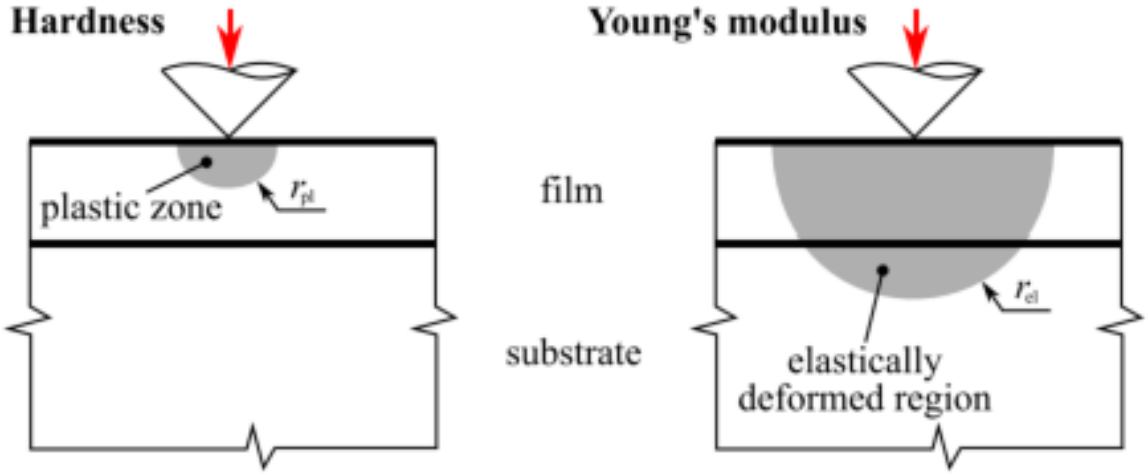

Figure 2-7 Schematic of the plastic zone and elastic zone under and an indenter tip (reproduced from [26]).

At a depth of 10% or less of the film thickness, it is highly unlikely that the elastically deformed region will interact with the substrate. Therefore, the hardness and modulus reported will not be influenced by the substrate. Thin films were used in Part I of this dissertation.

2.3.1 Nanoblitz 3D and 4D

Nanoblitz 3D and Nanoblitz 4D are specific nanoindentation methodologies used to create mechanical property heat maps by implementing high-speed indentation [28]. The test outputs are very similar to those of traditional indents with the addition of mechanical property heat maps [28]. When creating the mechanical property heat maps, it is essential to ensure the indents are spaced at a great enough distance to avoid the overlap of plastic zones while avoiding the need for excessive interpolation and using too much of a sample's surface area.

In the 1950s, Samuels suggested that for macro indentation testing, the indent should be spaced 2.7 times the width, as measured from the center of the indent to the edge of the adjacent impression [29]. This work was based on the elastic-plastic zone created by various indenter tips such as Brinell-ball, Vickers-pyramid (Figure 2-8), non-standard ball, and pyramidal.

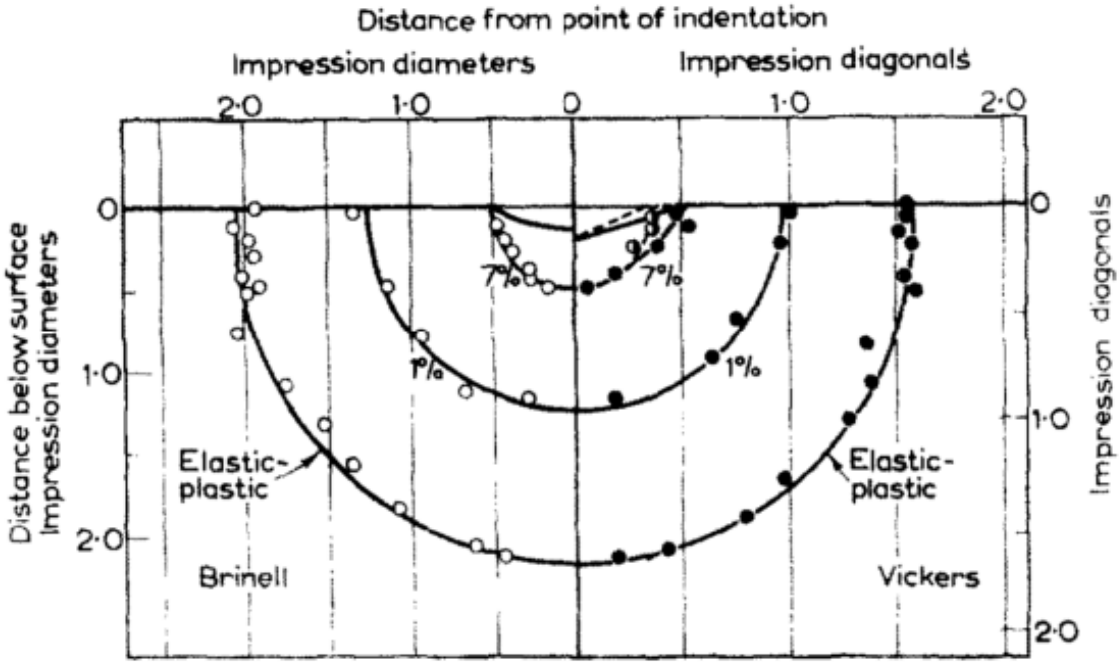

Figure 2-8 Strain boundaries for Brinell-ball (left) and Vickers-pyramid (right) impressions on a semi-infinite structure (reproduced from [29]).

Since then, further investigation into optimal nanoindentation spacing has been conducted. Based on both finite element analysis and experimentation, there is strong evidence that fully dense materials require a minimum indent spacing to indent depth (*d/h*) ratio of 10 [28].

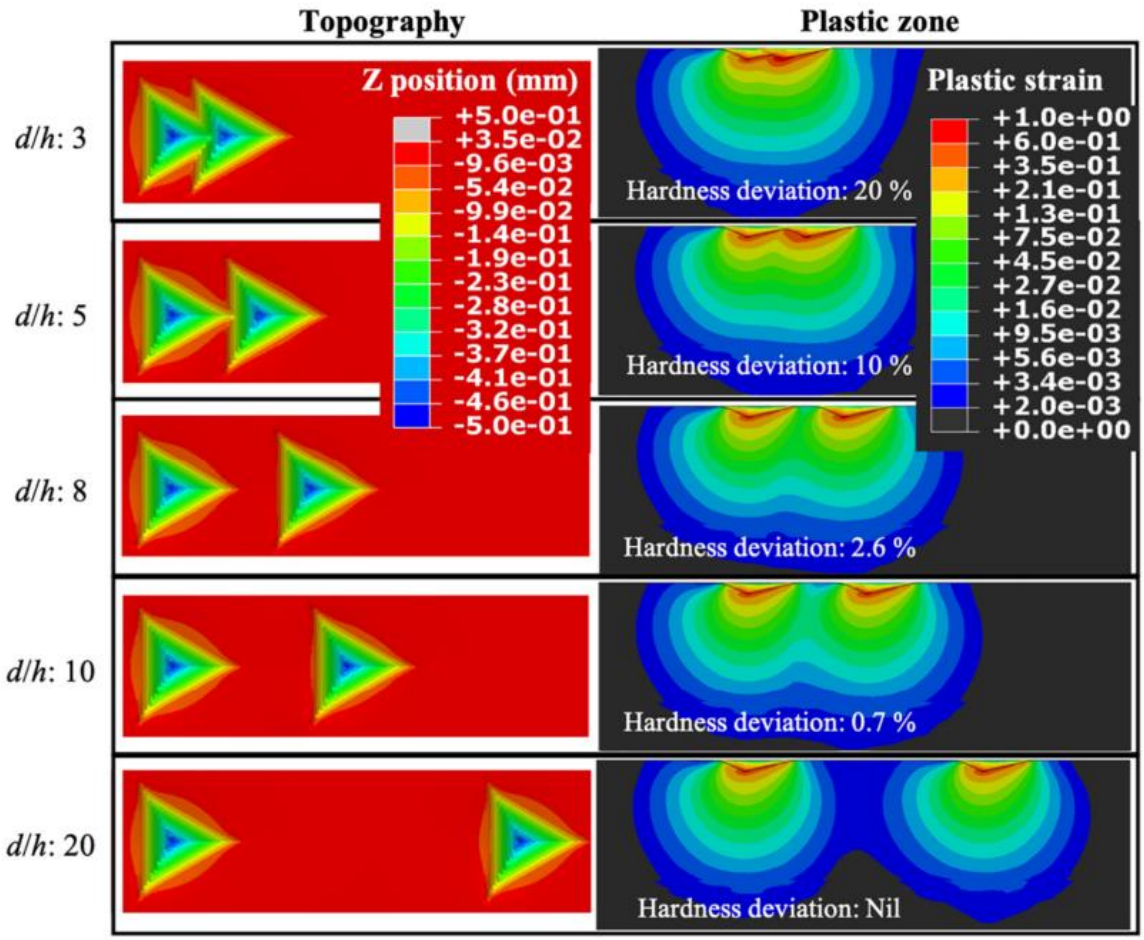

Figure 2-9 Finite element analysis of a Berkovich indent topography and cross-sectional strain contours at various *d/h* ratios (reproduced from [28]).

Figure 2-9 illustrates that at *d/h* ratios above 10, the hardness deviation drops below one percent. When the *d/h* ratio drops below 10, the residual plastic strain from the previous indent influences the neighboring indent. If the *d/h* ratio drops below 5, the indents begin to overlap. The minimum, *d/h* ratio for the system must be known to ensure accurate and precise hardness and modulus values.

Nanoblitz 3D creates a 2D heat map of hardness and modulus at the total contact depth. Nanoblitz 4D creates 2D mechanical property heat maps of hardness and modulus at various depths approaching the total contact depth. For Nanoblitz 4D, the total depth is divided into a specific number of layers as determined by the user. For example, if a user

wants ten layers of indents to a depth of 1000 nm, a hardness and modulus heat map will be created at 100 nm intervals. The addition of the mechanical property heat maps to traditional nanoindentation allows further insight into the sample and where fluctuations in mechanical properties occur.

Nanoindentation was performed using an iNano from KLA, formally Nanomechanics, with a Berkovich tip.

PART I

NANOPOROUS GOLD

CHAPTER 3. BACKGROUND OF NANOPOROUS GOLD

Nanoporous gold (np-Au) falls within the broad category of porous materials and, more specifically, porous metals or metal-air composites [30]. Nanoporous (np) refers to a material with a pore size between 0.1 and 100 nm, porosity greater than 40%, and a high surface-area-to-volume ratio [31]. Np metals have been a focus of recent research due to their ability to encapsulate multiple desirable material characteristics, including high surface areas, mechanical size effects, and high thermal and electrical conductivity [32]. Np metals that demonstrate these material characteristics include np-Cu, Ag, Pd, and Au. Np-Au is one of the more well-researched np materials because it has a relatively straightforward synthesis process and chemical stability [32]. This chapter gives an overview of the mechanical properties of porous materials and np-Au's mechanical properties and applications.

3.1 Overview of Mechanical Properties of Cellular Structure

When discussing porous materials, it is important to understand their cellular structure and mechanical behavior. Gibson and Ashby's research provided the basis for this understanding [33, 34]. They focused on the mechanical properties of materials with a cellular structure. Their overarching ideas about cellular structure can be used to further understand materials like nanoporous gold. Their work began with understanding the linear-elastic response of a two-dimensional honeycomb structure to determine where bending and compression occur when a load is applied (Figure 3-1).

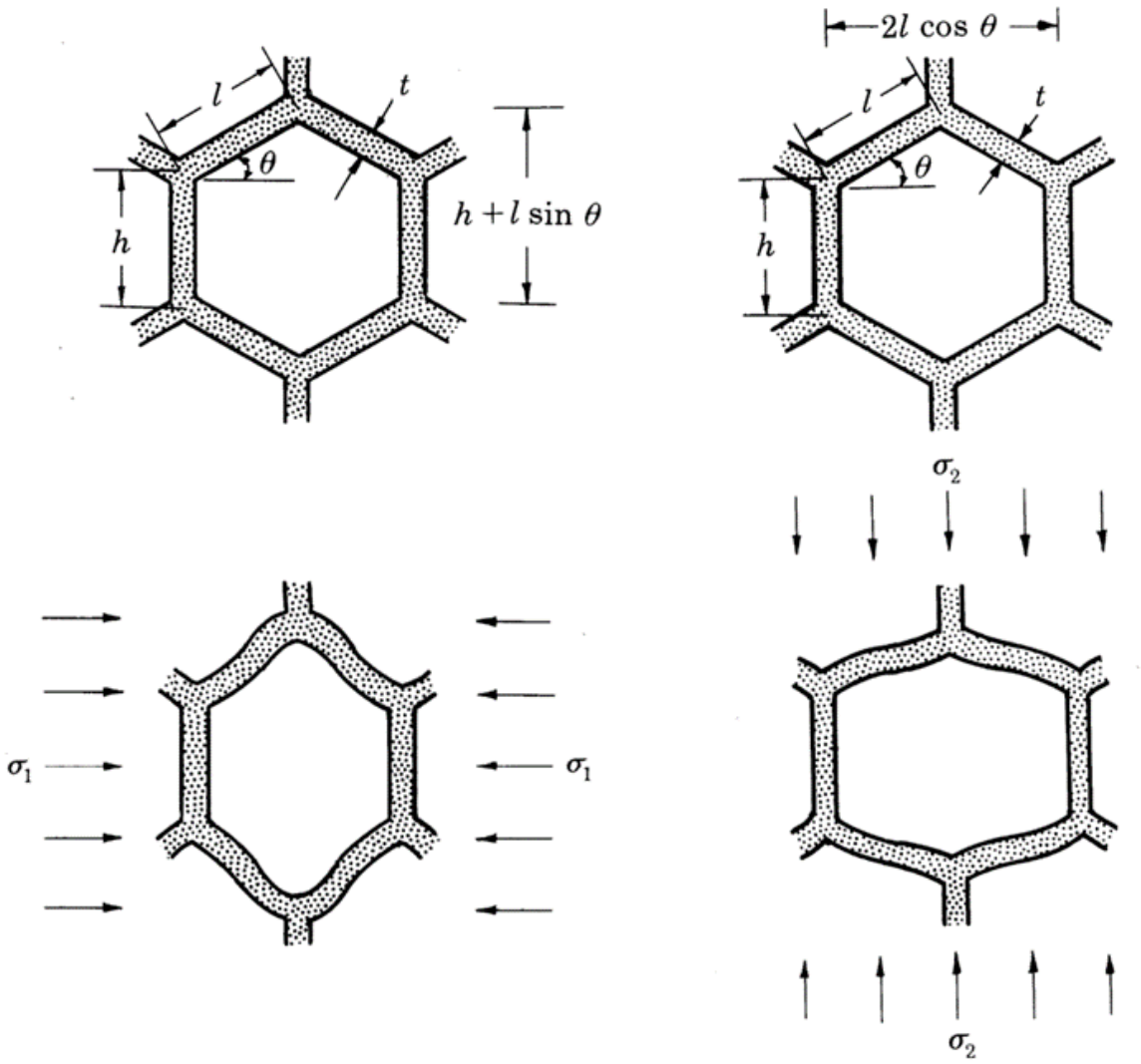

Figure 3-1 Cell deformation of a honeycomb structure with loading in directions 1 and 2 (reproduced from [34]).

The loading force affected both the cell walls and the opening within the cell walls. Figure 3-1 shows the important terminology of a cell's composition, including beam thickness (t), cell wall length (l), cell wall height (h), and the angle between adjoining cell walls (θ). The relative density of the cell can be found with the knowledge of t, l, h, and θ of the cell structure [34]:

$$\frac{\rho}{\rho_s} = \frac{(2+h/l)t/l}{2\cos(\theta)(h/l+\sin(\theta)} \qquad \text{Equation 3-1}$$

where ρ/ρ_s is the relative density of the cell. This equation can be further simplified when we assume that the cell structure is a regular hexagon (θ= 30°) and that height and length of the cell walls are equal (h=l).

$$\frac{\rho}{\rho_s} = \frac{2}{\sqrt{3}} t/l \qquad \text{Equation 3-2}$$

Using beam theory (Equation 3-3), Gibson and Ashby were able to formulate a series of equations to determine the Young's modulus (E) and the reciprocal relationship between the Young's modulus and Poisson's ratio (v) in a two-dimensional structure. They established the following equation [34]:

$$I = \frac{t^4}{12} \qquad \text{Equation 3-3}$$

$$E_1 v_2 = E_2 v_1 = 12 E_s I/l^3 t sin(\theta)\cos(\theta) \qquad \text{Equation 3-4}$$

where I is the moment of inertia, b is the width of the wall, and E_s is the Young's modulus of the structure. Note that Equation 3-3 assumes the width of the beam length (b) and the width of the beam height (h) are equal and, therefore, simplified to one width or thickness, t. The full table of mechanical behavior of two-dimensional cellular materials can be found in Appendix 1.

Beginning with a simple cubic structure, Gibson and Ashby also used the concepts of a two-dimensional honeycomb and applied those concepts to a three-dimensional cellular structure (Figure 3-2).

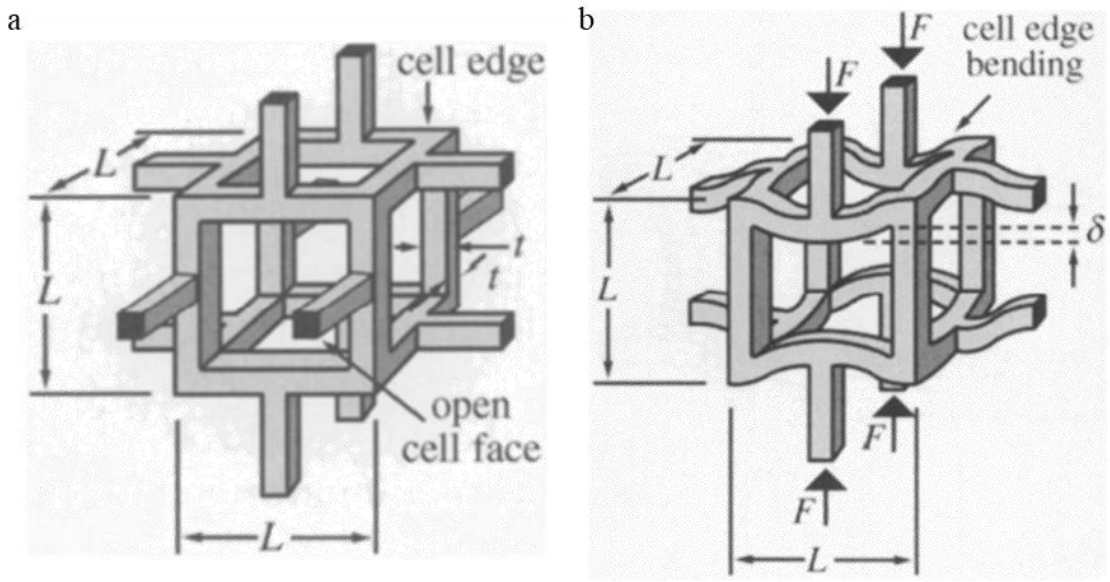

Figure 3-2 Cubic model of a closed-cell cellular model (a) under no load and (b) under load (reproduced from [35]).

Equations 3-2 and 3-4 were modified for a foam, or three-dimensional structure, in order to depict the relative density and the Young's modulus [33]. The three-dimensional foam properties are related to that of the cell wall properties. The modified equations for a closed-cell structure are the following:

$$\frac{\rho}{\rho_s} = \frac{(t/l)^2 + 0.766(t/l)^3}{0.766(1+t/l)^3} \qquad \text{Equation 3-5}$$

$$\frac{E}{E_s} = C_1 \left(\frac{\rho}{\rho_s}\right)^n \qquad \text{Equation 3-6}$$

where ρ/ρ_s is the relative density of the foam, C_1 and n are constants. C_1 is a constant of proportionality (commonly assumed to be 1) when discussing the relative Young's modulus. A summary of all the mechanical behavior formulas derived from Gibson and Ashby's work is presented in Table 3-1.

Table 3-1 Summary of mechanical behavior of three-dimensional cellular materials from the Gibson-Ashby model (reproduced from [33]).

Mechanical Property	C	Final Theoretical Equation	Simplified Equation	ρ/ρ_s law valid for
Relative Density (ρ/ρ_s)	-	$\frac{\left(\frac{t}{l}\right)^2 + 0.766\left(\frac{t}{l}\right)^3}{0.766\left(1+\frac{t}{l}\right)^3}$	$(t/l)^2$	All ρ/ρ_s
Relative Young's modulus	1	$\frac{\left(\frac{t}{l}\right)^2}{1+\frac{t}{l}}\left[\frac{1}{\left(\frac{l}{t}\right)^2+4+\frac{t}{l}}\right]$	$\left(\frac{\rho}{\rho_s}\right)^2$	All ρ/ρ_s
Relative shear modulus, $\frac{G}{E_s}$	0.4	$\frac{0.4\left(\frac{t}{l}\right)^2}{1+\frac{t}{l}}\left[\frac{1}{\left(\frac{l}{t}\right)^2+4+\frac{t}{l}}\right]$	$0.4\left(\frac{\rho}{\rho_s}\right)^2$	All ρ/ρ_s
Relative elastic collapse stress, $\frac{\sigma^*_{el}}{E_s}$	0.03	$\frac{0.03\,(\frac{t}{l})^4}{(1+\frac{t}{l})^2}$	$0.05\left(\frac{\rho}{\rho_s}\right)^2$	$\rho/\rho_s < 0.30$
Relative plastic yield stress, $\frac{\sigma^*_{pl}}{\sigma_y}$	0.30	$\frac{0.30\,(\frac{t}{l})^4}{(1+\frac{t}{l})^2}$	$0.30\left(\frac{\rho}{\rho_s}\right)^{3/2}$	$\rho/\rho_s < 0.63$

Note that while not all Gibson and Ashby's formulas have a dependence on the relative density, those that do are only valid for specific relative densities. For example, the relative elastic collapse stress to be valid, the relative density must be less than 0.3 and for the relative plastic yield stress to be valid, the relative density must be less than 0.63. Since most foams have a relative density between 0.03-0.3, these specific parameters are only critical to a few systems [36].

It has been found that while the mechanical properties of foams are dependent on the ratio of the cell wall thickness to the length, or relative density, most of their mechanical properties are not dependent on absolute cell size [36, 37]. As a result, the moduli of foams are influenced by the relative density of the foam and not by the ligament size [33, 38]. As the relative density increases, the relative Young's modulus increases [36].

While Gibson and Ashby established equations for cell structures with linear walls, most foams composed of metallic elements have curved walls. Due to their curved walls, their mechanical properties were lower mechanical properties than those predicted by the Gibson and Ashby equations. Section 3.2 discussed the mechanical behavior equations derived for np-Au as it is a curved-wall structure.

When a metallic foam is compressed, the stress-strain curve shows three distinct regions: (1) linear elastic (bending) (2) plateau (plastic yielding), and (3) densification (Figure 3-3).

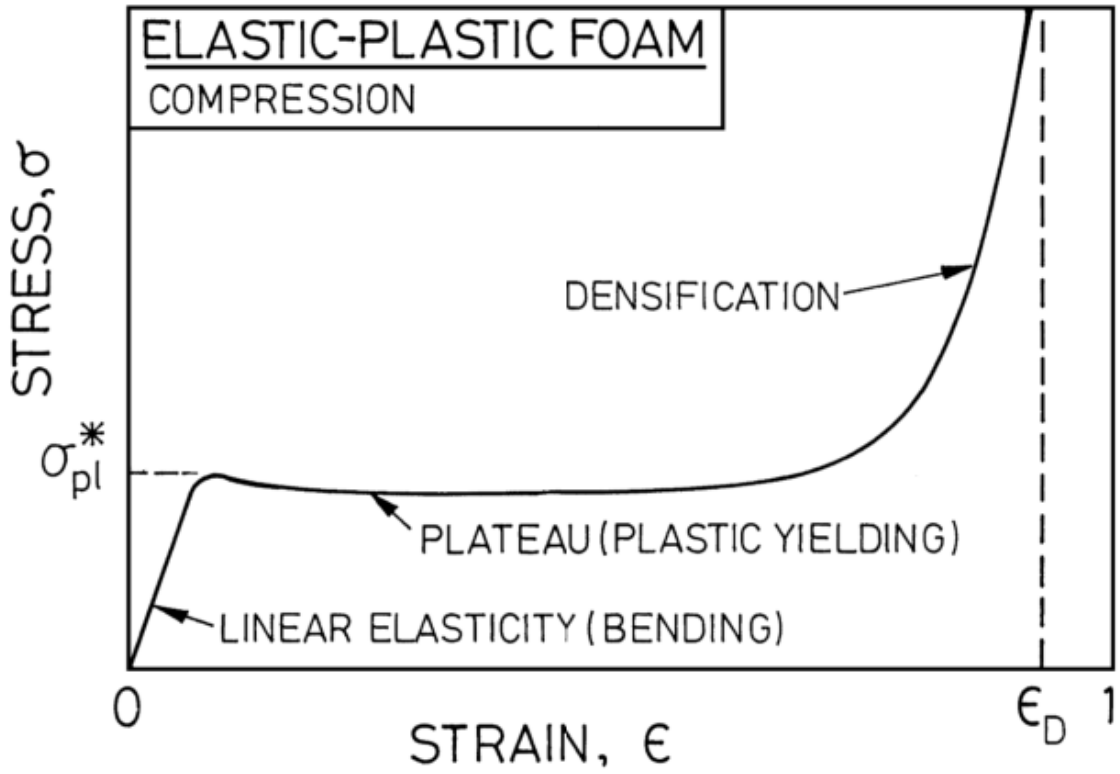

Figure 3-3 Schematic of a compression stress-strain curve for a foam indicating the three main strain regions (reproduced from [39]).

Figure 3-3 shows the initial linear elasticity, the plateau of plastic yielding, and the sharp increase in stress during densification [36, 37]. The linear elastic response relates to the cell edges bending in an open cell [39]. In the following region (plastic yielding), as the stress increases, the cell begins to collapse at a fairly constant load. Depending on the cell wall material, the cell will collapse by elastic buckling, yielding, or fracture [39]. The final region of deformation occurs when all of the cells have collapsed and the cell walls compress against each other [39]. This model of behavior has been successful in modeling metallic foams such as aluminum foam [36]. We can apply this understanding of how porous material deforms to specific structures such as nanoporous gold.

3.2 Nanoporous Gold

Nanoporous gold (np-Au) has a sponge-like structure with a nanoscale network structure composed of ligaments and pores (Figure 3-4). This structure is formed through chemical dealloying to achieve a high surface-area-to-volume ratio [40-43]. Ligaments are randomly oriented during dealloying and vary in size from 10-100 nm without coarsening or heat treatments [44, 45].

Np-Au's high surface-area-to-volume ratio is useful in various applications such as catalyst reactions [46-49], actuators and sensing [5, 46, 50], and electrodes [51, 52]. Np-Au is used in the field of catalysts due to its high electric conductivity, low-temperature CO oxidation, and high surface-area-to-volume ratio [53, 54]. Wittstock has shown that np-Au can be used in actuator/sensor technology by converting chemical energy directly into mechanical work [5]. Additionally, np-Au can be used as electrodes in bioelectric applications due to its conductivity, chemical and mechanical stability, and biocompatibility [55]. These applications typically require a small ligament size to promote a higher surface-area-to-volume ratio, which is characteristic of np-Au. The ligament structure of np-Au is depicted in Figure 3-4.

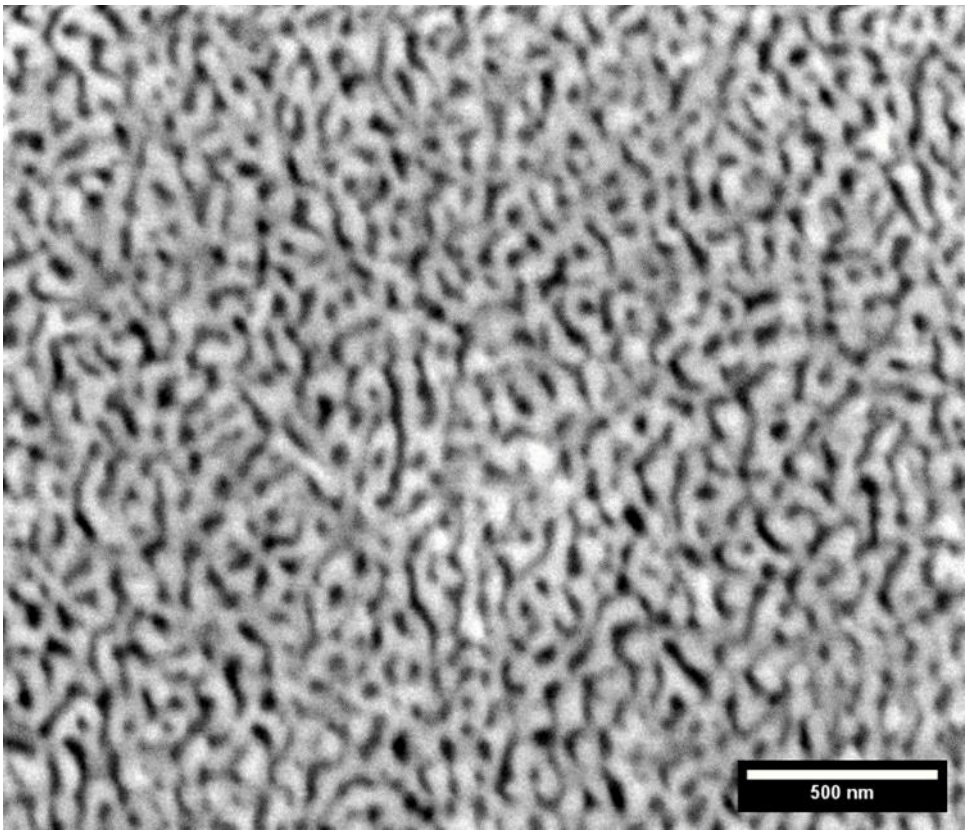

Figure 3-4 SEM micrograph (SE mode) of a typical ligament structure of nanoporous gold, with nanometer-length scale ligaments and pores.

In many applications, np-Au is required to perform at elevated temperatures, which can significantly affect its microstructure [56, 57]. Further, it is important to note that nanoporous structures exhibit changes in mechanical behavior based on changes in their ligament size and relative density [46, 58-60]. Specifically, the hardness decreases as their ligament size increases [46, 61].

Furthering the work by Gibson and Ashby, Briot created a new scaling relationship for np-Au yield strength. Np-Au has ligaments that are shorter in length relative to its diameter, making their ligaments bulkier than most other porous materials. This causes np-Au's relative densities to be higher (ranging between 0.2-0.5) than most foam structures (ranging between 0.03-0.3) [36, 44, 60]. Their higher relative density causes Gibson and

Ashby's equations to predict the mechanical behavior of np-Au incorrectly. The yield strength of foam materials is related to the mechanical properties of its dense material. The equation to find the yield strength of a foam material is the following:

$$\sigma^* = C\sigma_s(\frac{\rho^*}{p_s})^n \quad \text{Equation 3-7}$$

where σ^* is the yield strength for a foam material, σ_s is the yield strength for the dense material, C is a scaling coefficient, and n is the scaling exponent. Through his experiments, Briot derived the scaling coefficient, C, and the scaling exponent, n, for np-Au [44, 60, 62].

The Hall-Petch relationship (Equation 3-8) is used to find the relationship between grain size and yield strength. The relationship shows that a fine-grained alloy exhibits a higher yield strength than the same coarse-grained alloy [63]:

$$\sigma_s = \sigma_i + k_y d^{-1/2} \quad \text{Equation 3-8}$$

where σ_s is the yield strength of the alloy, σ_i is the constant for lattice resistance, k_y is the Hall-Petch coefficient, and d is the average grain diameter [21, 63]. Briot used the foundations of the Gibson and Ashby and the Hall-Petch relationships (Equation 3-7) to derive the following equation for the ligament size effect on the yield strength [44, 62]:

$$\sigma_s \cong kl^{-m} \quad \text{Equation 3-9}$$

where k is the size effect coefficient, l is the ligament size, and m is the size effect exponent. For np-Au, the size effect coefficient is k=0.0328 MPa and the size effect exponent is m=0.551. By substituting the yield strength found in Equation 3-9 into Equation 3-7, a new scaling relationship for the yield strength can be found.

$$\sigma^* = Ckl^{-m}(\frac{\rho^*}{p_s})^n \quad \text{Equation 3-10}$$

Based on the work done by Shaw and Sata, the hardness and yield strength (σ_s) of porous materials are equal and thus assumed in Briot's equation [64]. As the ligament size increases, Equation 3-10 leads to a lower predicted yield strength (or hardness) of np-Au than had the Gibson and Ashby equation been used. Briot's new scaling relationship (Equation 3-10) is used for ligament sizes below 1 μm. As all the tested samples had ligament sizes below half a micron, his scaling system was employed for the work discussed in this dissertation.

3.3 Coarsening

Applying heat to the np structure causes coarsening, or growth in ligament diameter, to occur. As stated previously, it is essential to understand the thermal stability of np-Au and its coarsening behavior under different heating environments. Prior studies showed that although np-Au displayed significant coarsening when dealloyed in air and chemically active diatomic gas (N_2 and O_2), similar coarsening did not occur when dealloyed in a vacuum or inert monoatomic gas (Ar) [58, 59]. This difference in coarsening is attributed to the rate of surface diffusion which is most likely stunted in these environments.

Coarsening of ligaments can be achieved by annealing the samples or varying the duration of dealloying [59]. The coarsening rate of nanoporous materials during dealloying and/or annealing follows a nonlinear relationship similar to isothermal grain growth in polycrystalline materials (Equation 3-11) [58, 65, 66]:

$$d(t)^n = k_0 t exp\left(-\frac{E}{RT}\right) = KtD_s \qquad \text{Equation 3-11}$$

where $d(t)$ is the ligament size at etching time t, n is the coarsening exponent, k_0 and K are constants, E is the activation energy for nanopore formation and coarsening, R is the gas

constant, T is the etching temperature, t is the time, and D_s is the diffusivity. Based on the surface diffusion-controlled coarsening mechanism, the diffusivity (D_s) can be estimated by the following equation [65]:

$$D_s = \frac{d(t)^4 kT}{32\gamma t a^4} \qquad \text{Equation 3-12}$$

where k is the Boltzmann constant, γ is the surface energy, t is the etching time, and a is the lattice parameter. Equations 3-11 and 3-12 can be applied to understand the surface diffusivity when annealing a porous structure.

Equation 3-13 shows the proportionality and scaling relationship between the diameter of the ligament (d) and time as a function of the coarsening exponent ($t^{1/n}$) [67]:

$$d \propto t^{(\frac{1}{n})} \qquad \text{Equation 3-13}$$

where d is the diameter of the ligament, t is the time, and n is the diffusion rate. To find the coarsening exponent (n), the linear relationship between log[d(t)] (found in Equation 3-11) and log(t) can be plotted. The linear slope of log[d(t)] versus log(t) is one over the coarsening exponent. However, it should be noted that most researchers denote the diffusion rate as it corresponds to the slope.

Many researchers have studied the ligament diameter of np-Au as a function of time and have determined the coarsening exponent for various conditions. The most common coarsening rate for np-Au when dealloyed in air is approximately $d \propto t^{0.25}$ [65, 66]. Other studies showed that when dealloyed in nitrogen (N_2), the coarsening rate exponent was closer to $d \propto t^{0.125}$ [68]. Other studies have confirmed that changes in the vacuum level pulled during dealloying impacted the coarsening rate. Work by Lu indicated that not only

did a higher vacuum result in a coarsening rate of $d \propto t^{0.25}$ but that a low vacuum caused the coarsening rate to increase to approximately $d \propto t^{0.33}$ [66].

CHAPTER 4. MATERIALS AND METHODS

The following sections describe the synthesis of np-Au, the annealing of its ligament structure, and the analysis of the resulting ligament diameter. The methodologies discussed in Chapter 2 were used to aid in this characterization and mechanical testing of np-Au.

4.1 Synthesis of Nanoporous Gold through Film Deposition and Dealloying

Nanoporous (np) materials are typically formed by creating a mixture of a more noble and less noble element. The final np structure will be composed of the more noble element once the less noble element is dissolved or etched away [44, 69, 70]. To form np-Au, Au is the more noble element, with Ag as the less noble element, typically [7, 71]. The less noble element is known as the sacrificial element since the intent is for it not to be in the final structure and thus is "sacrificed" to create the pores in the system. Erlenbacher [7, 72] described the additional composition features necessary for a nanoporous structure to form, including:

1. The composition should be rich (at least 50 at%) in the less noble element.
2. The alloy must be homogenous (preferably solid solution) before dealloying.
3. The diffusion of the more noble element must be sufficiently faster than the less noble element.
4. A difference in the potentials required to dissolve/etch the alloy component so that only the less noble element is removed.

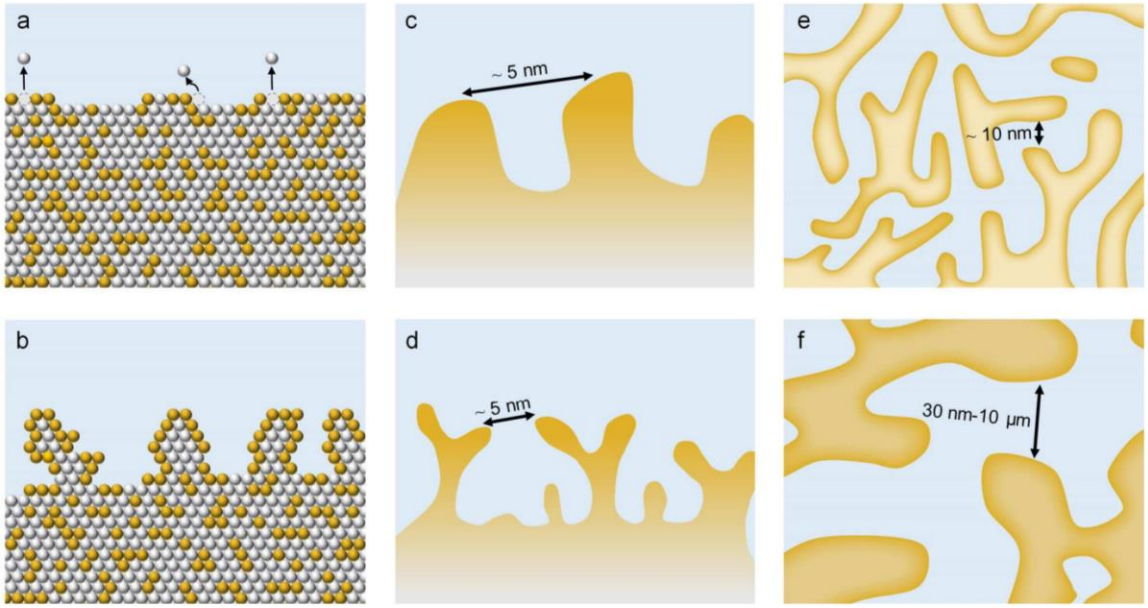

Figure 4-1 Schematic of chemical dealloying of Au-Ag where the Ag is shown in white and Au is shown in yellow. The schematic depicts the steps of dealloying a homogenous alloy in a chemical bath where (a) is the beginning structure with Ag slowly leaving the surface (b) Au is left at the surface as Ag diffuses into the chemical bath c) and (d) depicts ligaments beginning to form € the Au ligaments have fully formed with some Ag still in the center as not all will be diffused to the surface (f) coarsening of the Ag ligaments (reproduced from [73]).

Thin films can be synthesized via physical vapor deposition (PVD). PVD is a plasma-based deposition process that builds films on a substrate [74]. Thin films are sputtered from magnetron sources, which deposit atoms from the source onto the substrate [75]. As seen in the schematic in Figure 4-2, PVD uses targets composed of the element(s) chosen for the film, which are transformed into atomic particles and directed toward the substrate by the use of a vacuum environment and a negative potential on the target [40, 44, 76].

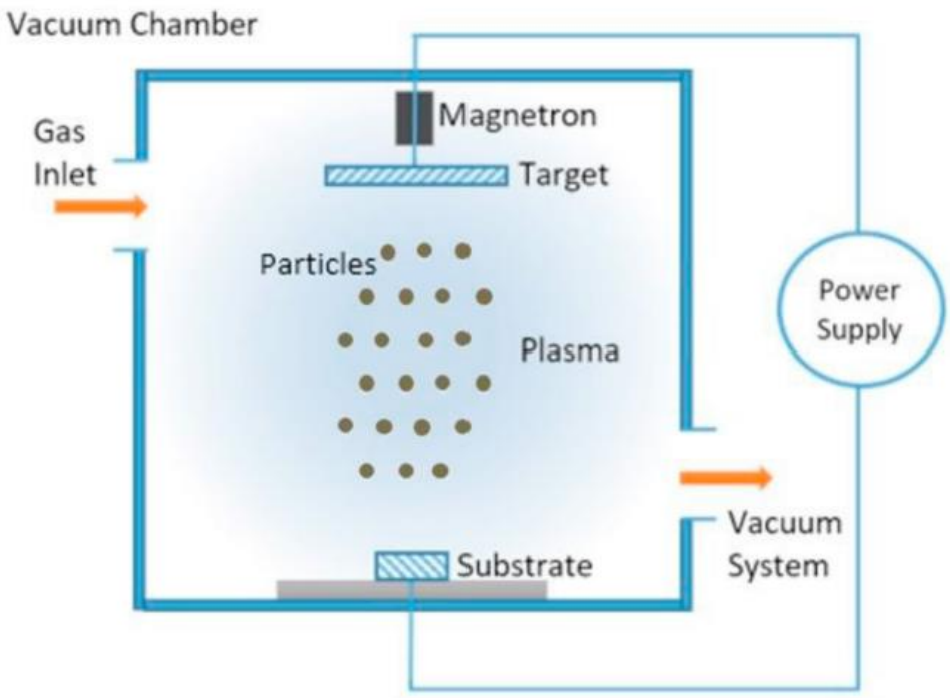

Figure 4-2 Schematic of PVD to sputter particles from the target onto the substrate by applying a power source to the target in a vacuum chamber (reproduced from [76]).

Previous work done by Briot and the Balk group at the University of Kentucky utilized this background knowledge of dealloying and PVD to design a methodology for the fabrication of nanoporous gold [40, 44, 45, 60, 62]. This methodology was followed to create the samples used in this dissertation. The reported range of Au needed to create a nanoporous structure in an Au-Ag precursor is 25-42% [44]. The samples for this work were sputtered via PVD and aimed to contain 37 at% Au and 63 at% Ag. The film was sputtered onto a (001)-oriented silicon wafer until a deposition layer was formed at approximately 1,000 nm. The Au-Ag films were sputtered using magnetron sputtering with an AJA International Orion Inc.'s ATC Orion system at the University of Kentucky.

The Au-Ag thin film was then chemically dealloyed in a nitric acid bath for 20 hours to remove as much of the Ag as possible. The film was then washed in deionized water for

80 minutes. After dealloying, the sample was analyzed with EDS to ensure it was at least 90 at% Au. Once the percentage was confirmed, the sample was coarsened through heat treatments in the SEM or wafer curvature system.

4.2 Coarsening of Nanoporous Gold

Coarsening of np-Au was completed by either a) *in-situ* SEM heating stage or b) in a wafer curvature system (WCS).

4.2.1 *In-situ* Heating

The FEI Quanta 250 Scanning Electron Microscope (SEM) has a heating stage attachment (Figure 4-3) that allows samples to be heated to 1400 °C. The heating stage attachment is not compatible with in a high-vacuum environment as it compatible with the Environmental SEM function, which only images in a low-vacuum environment with nitrogen flowing. Samples in this study were heated to temperatures ranging from 200-600 °C at a heating rate of 20 °C/minute, at a pressure of 0.15 mbar.

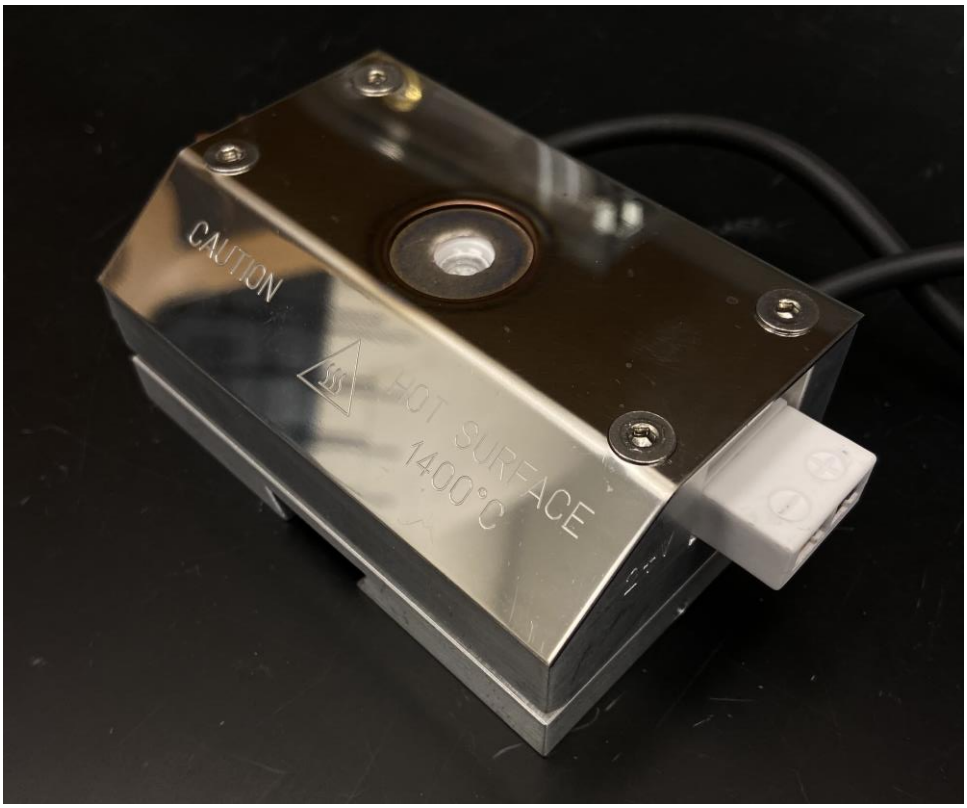

Figure 4-3 Heating stage attachment for the FEI Quanta 250 SEM.

4.2.2 Wafer Curvature System

The WCS, FLX-2320-S Toho Technology, was used to heat and coarsen samples. Samples were coarsened by annealing at 500 °C with N_2 flowing. To ensure samples had varying ligament diameters, the samples were held at temperature for either 10 or 20 minutes.

4.3 Ligament Diameter Determination

The ligament diameter was determined by measuring the average diameter of numerous ligaments. SEM micrographs of samples at various phases of heating were

taken and the ligament diameters were measured using line tools function in ImageJ. Over 50 different ligaments were measured in each sample to determine an accurate average ligament diameter (Figure 4-4).

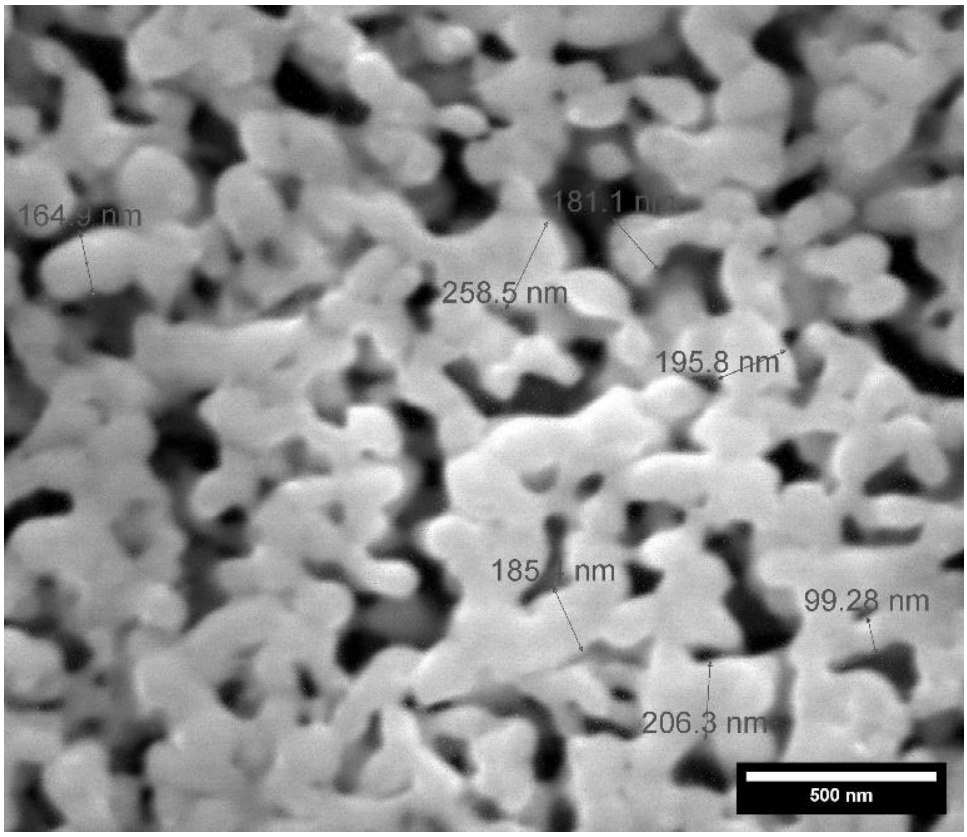

Figure 4-4 SEM micrograph of np-Au after annealing in WCS for 10 minutes at 500 °C with diameter measurements on seven different ligaments.

Figure 4-4 is an example of ligament diameters measured for a np-Au sample annealed at 500 °C for 10 minutes in the WCS. Each sample had a wide range of ligament diameters which can be seen in Figure 4-5.

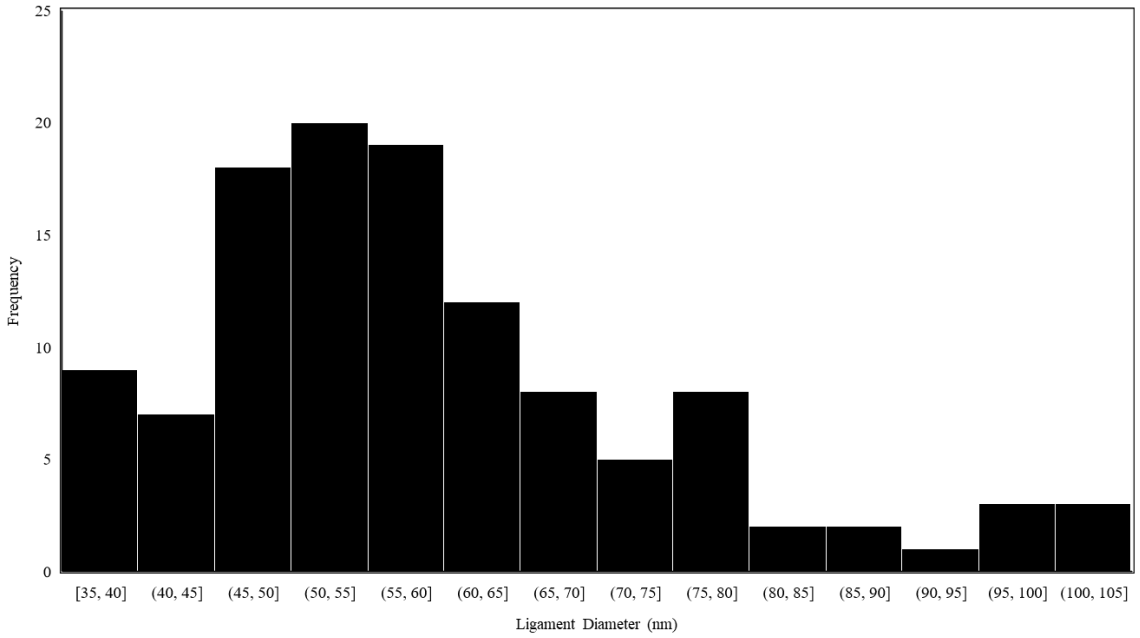

Figure 4-5 Histogram of ligament diameter measurements made for the as-dealloyed sample.

The ligament diameter measurements made for the as-dealloyed sample can be seen in Figure 4-5. These measurements give an average ligament diameter of 60 nm with a standard deviation of 15 nm.

CHAPTER 5. *IN-SITU* COARSENING OF NANOPOROUS GOLD

Previous research has been conducted to understand the structural changes to np-Au when it was dealloyed or annealed at different temperatures and environments [65, 66, 68]. However, further work is necessary as *in-situ* experiments are needed to observe the evolution of ligament growth in real time as this has not been done in SEM. Previous work has shown coarsening *in-situ* with the aid of TEM to demonstrate how coarsening in vacuum stunts ligament growth when compared to coarsening in air with annealing temperature below 400 °C [58]. However, this work did not account for the influence that the electron beam has on coarsening which is discussed in Section 5.1.1. This work demonstrates an SEM, *in-situ*, experiment of np-Au ligament coarsening when annealed on an SEM heating stage up to an annealing temperature of 600 °C. Samples were brought to an elevated temperature and then held at that temperature for 60 minutes. Before heating, each sample started with the same as-dealloyed structure with an average ligament diameter of 60 +/- 15 nm (Figure 5-1).

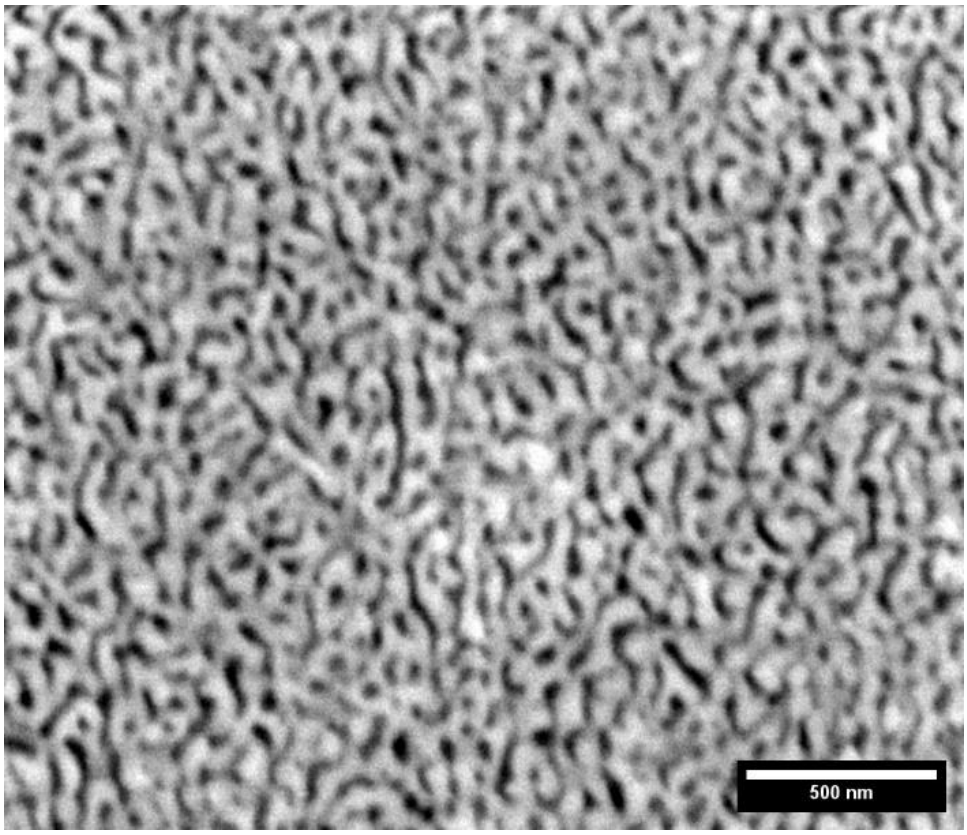

Figure 5-1 As-Dealloyed np-Au with average ligament diameter of 60 +/- 15 nm and relative density of 40%.

5.1 Results and Discussion

To capture the evolution of coarsening over time, micrographs of each np-Au sample were obtained every 2 minutes with an accelerating voltage of 20 kV and a working distance of 15 mm. The ligaments were measured at each stage to determine if any ligament coarsening occurred. Results showed that the np-Au structure was stable at lower temperatures but demonstrated significant ligament growth at higher temperatures. The changes in ligament diameter after 60 minutes of heating can be seen qualitatively in Figure 5-2.

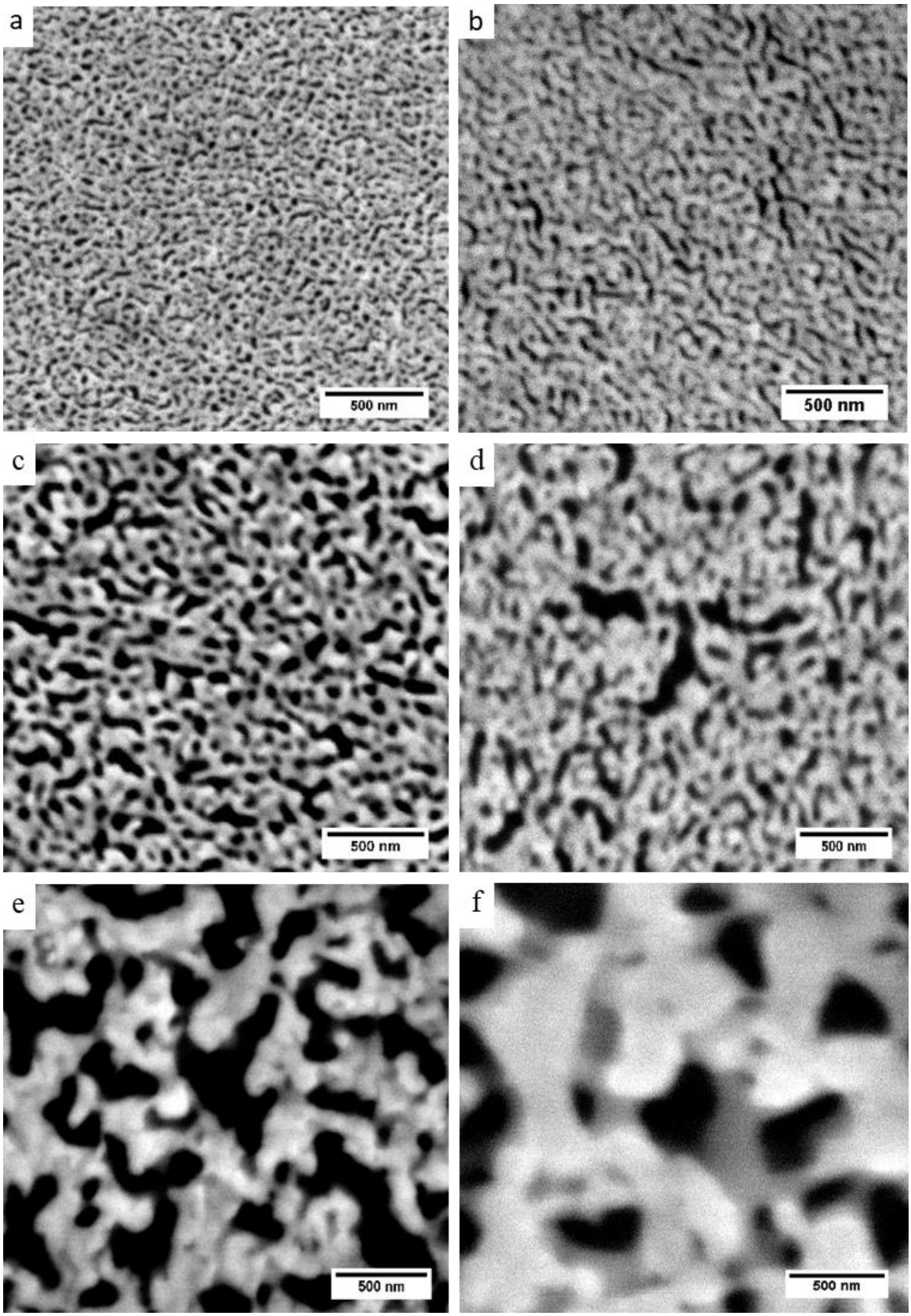

Figure 5-2 SEM micrographs of np-Au (a) as-dealloyed and after 60 minutes of heating at (b) 200 °C (c) 300 °C (d) 400 °C (e) 500 °C and (f) 600 °C.

There was little to no change in the ligament diameter after 60 minutes of heating at 200 °C and 300 °C (Figure 5-2(b) and Figure 5-2(c)) however, there begin to be slight microstructural changes to when the annealing temperature is above 300 °C. More defined microstructural changes in the ligament structure were noticed at annealing temperatures above 400 °C (Figure 5-2(d)). The most noticeable differences in ligament structure were seen after 60 minutes of heating at 600 °C (Figure 5-2(f)). Interestingly, even at 600 °C, the sample coarsened without any cracking in the ligament structure.

Denoted in black in Figure 5-3, the ligament diameter of the as-dealloyed sample was approximately 60 nm. The SEM micrographs in Figure 5-2 depict the average amount of growth after 60 minutes. The changes over those 60 minutes can be seen quantitatively in Figure 5-3.

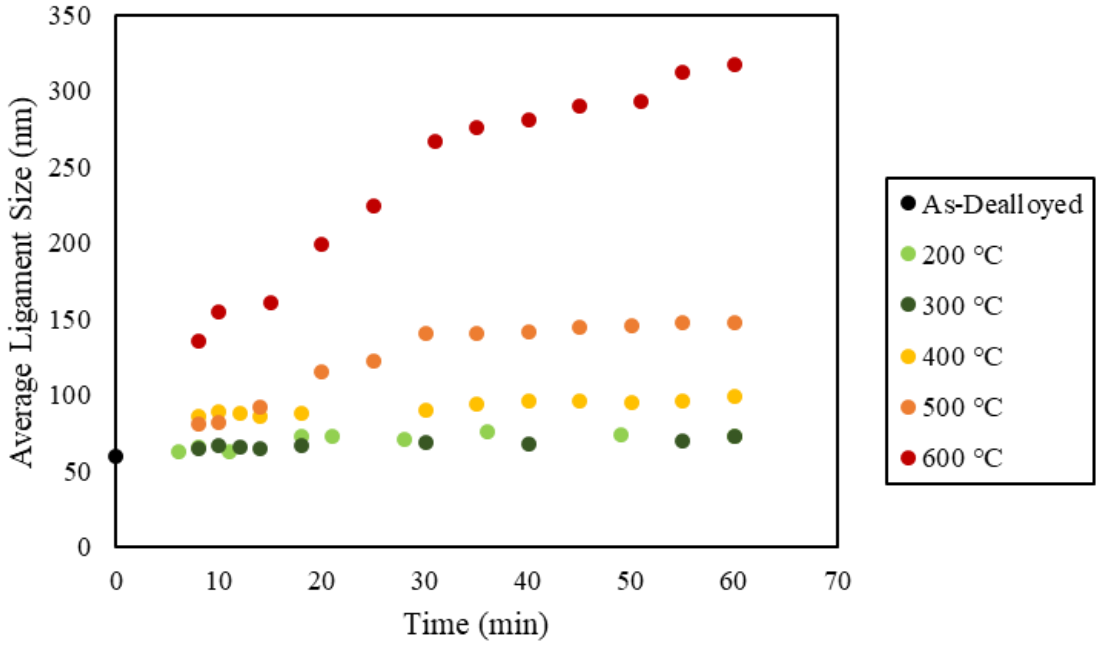

Figure 5-3 Average ligament growth over time at various set heating temperatures in the SEM heating stage.

As noted above, there was little to no growth when coarsened below 300 °C but the average ligament diameter began to change slightly at temperatures above 400 °C. After 60 minutes of heating at temperatures below 300 °C, the average ligament diameter was 72 +/- 22 nm which falls within the standard deviation range of the as-dealloyed average ligament length of 60 +/- 15 nm. Coarsening became more noticeable at temperatures of 400 °C when the ligament diameter coarsened from 60 +/-15 nm to 100 +/- 40 nm. The most significant coarsening occurred at 600 °C, with the average ligament diameter increasing from 60 +/- 15 nm to 317 +/- 130 nm.

A change in growth rate was noted after approximately 30 minutes of heating. The growth rate during the first 30 minutes was higher than the final 30 minutes. After the 30-minute mark, the average ligament diameter began to plateau. To further study this change in growth rate, it was necessary to determine the log of the ligament diameter versus the log of time (Figure 5-4). Due to small changes in coarsening at temperatures below 400 °C, Figure 5-4 only shows the coarsening rates for the heating experiments above 400 °C.

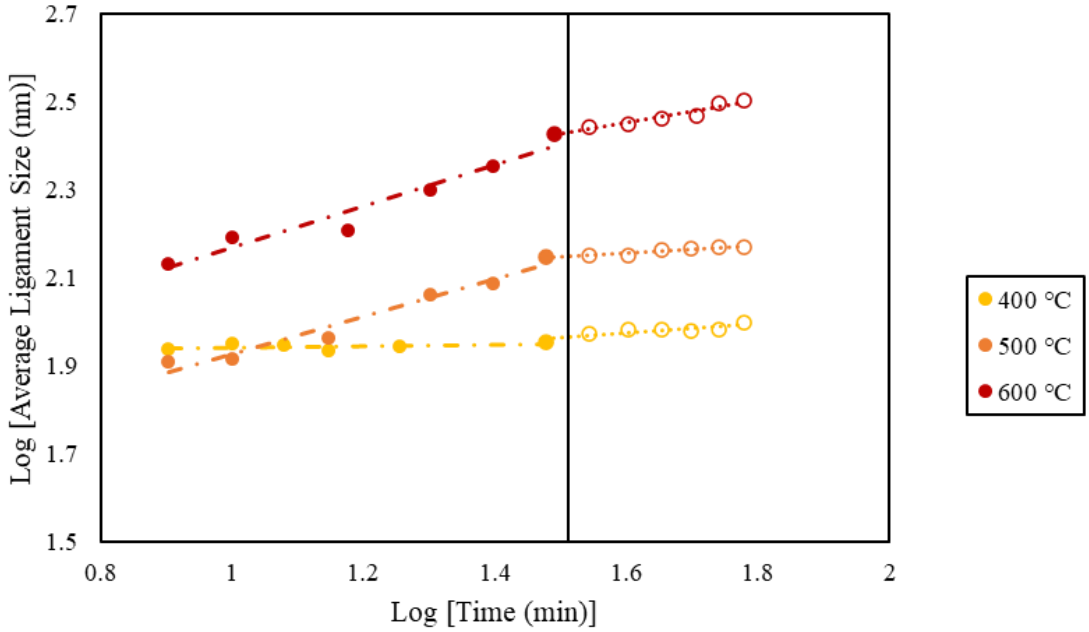

Figure 5-4 Log-log plot of the average ligament diameter versus time with the 30-minute mark denoted with a black line.

The change in the coarsening rate at the 30-minute mark, denoted by the black line in Figure 5-4, is more readily seen on the logarithmic-logarithmic plot. At temperatures above 500 °C, the initial slope was steeper than the final slope, denoting a change in ligament growth rate. The slopes (initial, final, and overall) for these linear fits are in Table 5-1.

Table 5-1 The initial slope of the log-log plot (0-30 minutes) and the final slope of the log-log plot (30-60 minutes).

Temperature	Initial Slope	Final Slope	Overall Slope
400 °C	0.02	0.11	.063
500 °C	0.43	0.08	.34
600 °C	0.47	0.25	.44

The initial slopes, when coarsened at temperatures above 500 °C, were higher than the predicted growth rate of 1/4; however, those slopes decreased in the final 30 minutes of heating. At 600 °C, the final slope was as predicted ($1/n=1/4$); however, at lower temperatures, the final slope was lower than predicted. It was interesting to note that the final slope at both 400 °C and 500 °C was similar to 1/8, which was the growth rate of samples dealloyed in N_2 [68]. It is important to reemphasize that this annealing process occurred in a low vacuum environment as previous studies have shown that the vacuum levels influence the growth rate. Based on these results, it appears that the resulting growth rate may have had other influencing factors (*i.e.*, the electron beam) in addition to the coarsening temperature.

Figure 5-5 shows the SEM micrographs of nanoporous gold as it evolved during the 60-minute heating period at 500 °C. The bright white dot denoted by a red arrow in Figure 5-5 illustrates that the electron beam stayed focused on the same location throughout the heating experiment. The blue arrows denote a region where smaller ligaments were absorbed into larger ones and smaller pores merged to become larger as time elapsed.

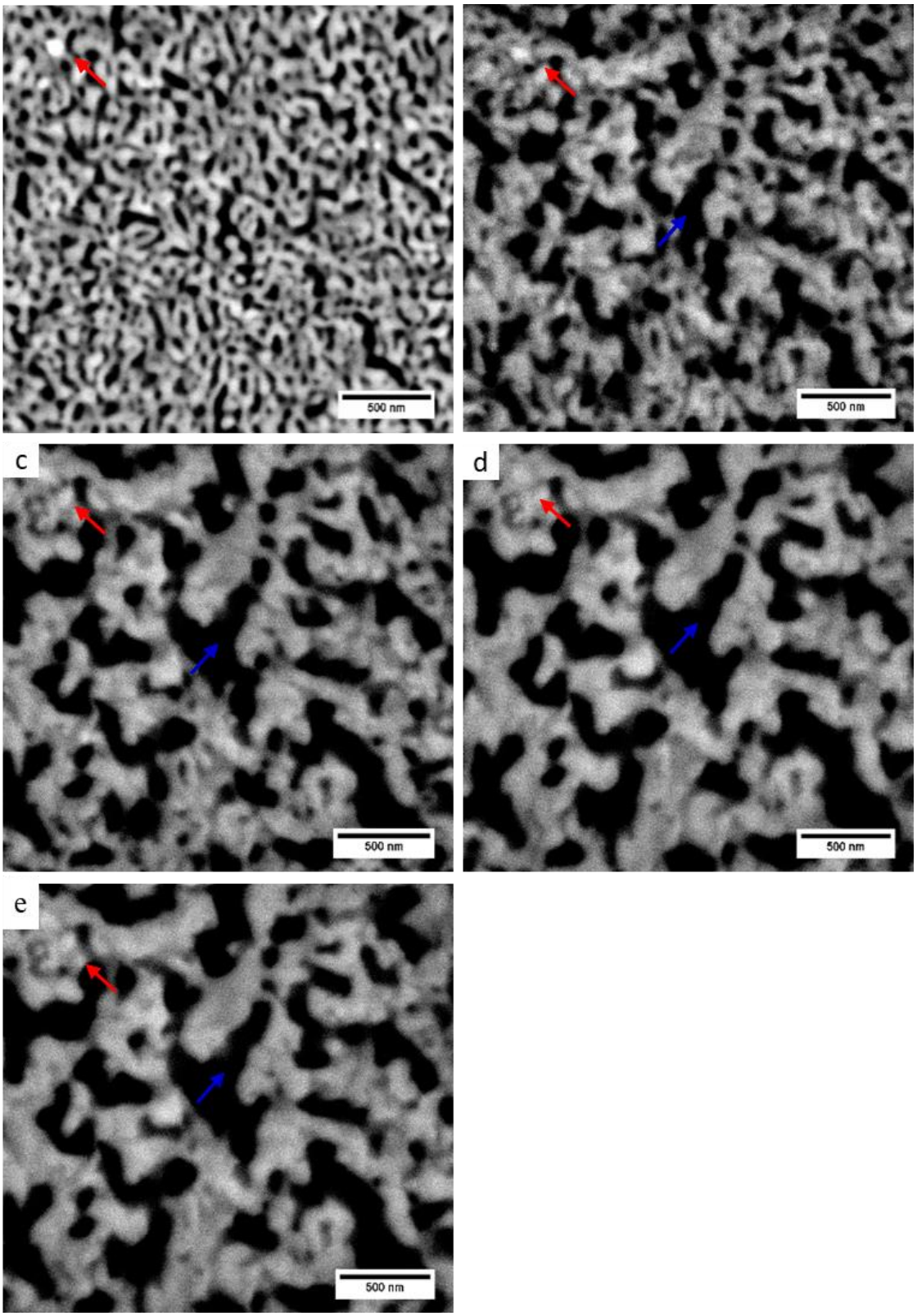

Figure 5-5 Ligament coarsening at 500 °C after (a) 2 minutes (b) 18 minutes (c) 30 minutes (d) 45 minutes and € 60 minutes where the red arrow marks the same spot on each micrograph and the blue arrow points to an area where a pore widens.

The rapid growth of ligament diameter can be seen in Figure 5-5 when comparing the SEM micrograph after 2 minutes (Figure 5-5(a)) and after 18 minutes (Figure 5-5(b)). In Figure 5-5(b), the original ligament structure can no longer be observed, and a larger ligament network has taken its place. After 30 minutes, there is little change to the micrographs (Figure 5-5(c)- Figure 5-5(e)) as most of the larger ligaments and pores had already formed. Most of the change occurred in the ligament structure as the small pores began to close.

It is hypothesized that the resulting higher initial slope above 500 °C may be due to the influence the electron beam had on the sample. Section 5.1.1 discusses the influence the electron beam has on coarsening.

5.1.1 Influence of Electron Beam on Coarsening

In reviewing the heating experiment test results, it was observed that the region of interest within the red box had more coarsening than the surrounding region (Figure 5-6). The red box shown in Figure 5-6 encompasses the area where the scanning electron beam was focused during the heating experiment. As such, there is evidence that the electron beam caused accelerated coarsening.

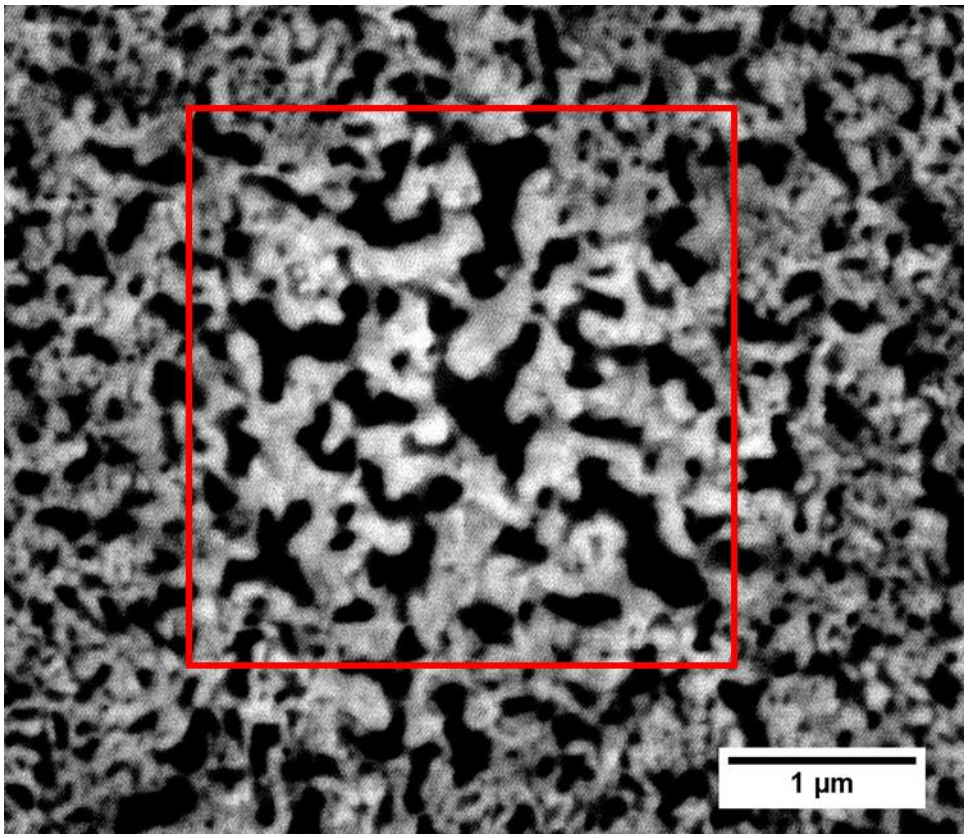

Figure 5-6 Micrograph of np-Au after 60 minutes of heating at 500 °C, where the region enclosed in the red box had the electron beam scanning throughout the experiment.

After completing the heating experiment at 500 °C, a micrograph was captured at lower magnification in order to visually identify the sample location where discrepancies in ligament diameter occurred. The red box highlights the region where the electron beam was focused. The ligaments inside the red box are visibly larger than those outside of the box. The influence of the electron beam has been quantified in Figure 5-7.

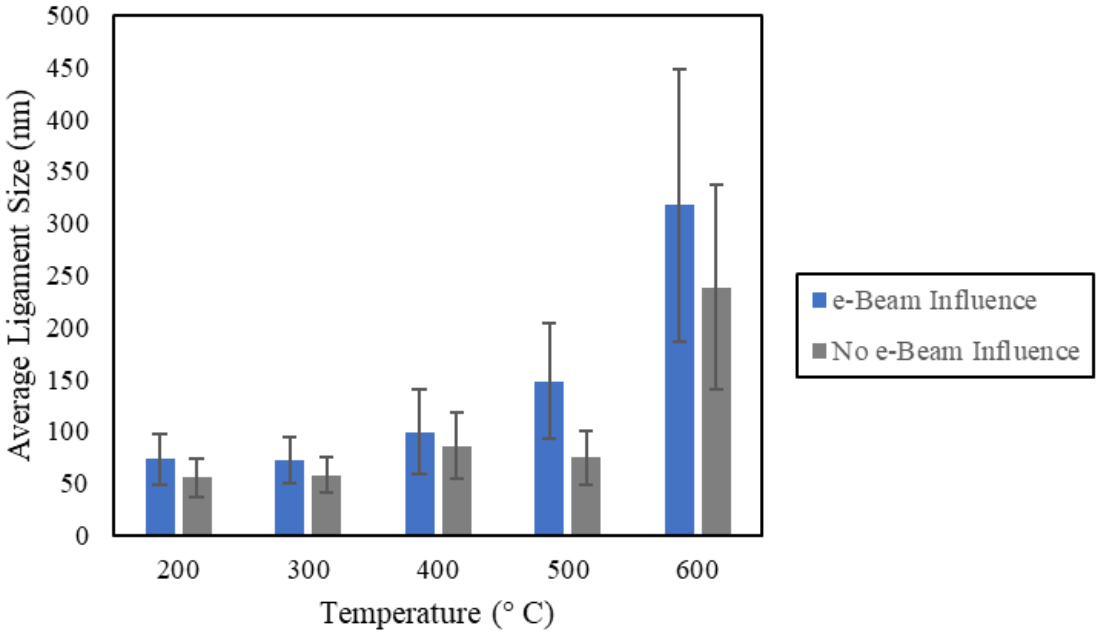

Figure 5-7 Average ligament diameter of np-Au with and without the influence of the SEM electron beam after 60 minutes of heating at various temperatures.

Figure 5-7 depicts the effect of the electron beam after the 60-minute coarsening period. There was little influence of the electron beam under 400 °C, as the average ligament diameter was similar for both regions regardless of the influence of the electron beam. This lack of influence was expected at temperatures below 300 °C since there was little ligament growth at these temperatures. The influence of the electron beam was more pronounced when heating above 500 °C, as there was a significant difference in the average ligament diameter in the region with and without the influence of the electron beam. At 500 °C, the average ligament diameter was 148 nm in the region influenced by the electron beam and only 75 nm in the region unaffected by the electron beam. Similarly, at 600 °C, the average ligament diameter was 317 nm in the region influenced by the electron beam and only 239 nm in the region that was unaffected by the electron beam. It is assumed that

the electron beam added additional energy to the system, which created more surface diffusion and thus further coarsening.

5.2 Conclusion

After 60 minutes of heating at 200 °C and 300 °C, little to no coarsening occurred. Significant ligament coarsening began when the sample was heated above an annealing temperature of 500 °C, with the most significant coarsening occurring at 600 °C. Coarsening with the SEM heating stage allowed for capturing micrographs at scheduled intervals to note changes throughout the 60-minute heating period. These micrographs allowed for a more detailed analysis of the changes that occurred within the np-microstructure compared to *ex-situ* coarsening experiments. The *in-situ* experiment allowed for a concentrated focus on a specific area to denote any growth of ligaments due to the absorption of smaller ligaments and the expansion of pores.

The rate of growth was also determined for heating temperatures above 400 °C. It was found that the initial rate of coarsening at 500 °C and 600 °C was higher than the predicted slope of 1/4; however, the rate of coarsening decreased during the final 30 minutes of the heating experiment to more closely resemble the rate of growth found in previous research. Through SEM imaging of the np-Au samples post-heat treatment, it was found that the electron beam enhanced the amount of ligament coarsening. The enhanced ligament coarsening was most likely caused by the sample's surface diffusion created by the electron beam. The high initial rate of growth, which had not been found in *ex-situ* experiments, is most likely due to electron beam enhancement.

This current work highlights the need to consider the potential impact of the electron beam source when running *in-situ* coarsening experiments that require a constant beam

source. When determining growth rates at one location it, unfortunately, is not practical to turn off the beam during heating. Specifically, the sample will experience thermal drift when the electron beam source is turned off, resulting in the location of interest to drift out of view.

Further work is necessary to understand why the electron beam only influenced coarsening during the initial stage of annealing. In addition, as this work was based on annealing temperatures ranging from 200-600 °C, testing at higher temperatures than 600 °C is necessary to further understand the effect the electron beam has on the growth rate. Also, additional testing with longer annealing times should be conducted to note any other growth rate changes when investigating via *in-situ* coarsening. Further work should also address the activation energies for annealing conditions with and without the influence of the electron beam.

CHAPTER 6. OPTIMAL INDENT SPACING FOR INSTRUMENTED NANOINDENTATION OF NANOPOROUS GOLD

To analyze the impact of indent spacing on nanoporous gold, an iNano, employing KLA's Nanoblitz 3D, a high-speed mapping technique was used. Using the Oliver-Pharr method, Nanoblitz 3D can indent large arrays and create mechanical property heat maps of both hardness and modulus and generate standard indentation data (*i.e.*, hardness, modulus, stiffness, depth, load). This section focuses on the effect the ratio of the indent spacing (*d*) to the indent depth (*h*), more commonly known as the *d/h* ratio, had on the various np-Au samples. The spacing of indents (*d*) is measured from the center of one indent to the center of the adjacent indent (Figure 6-1).

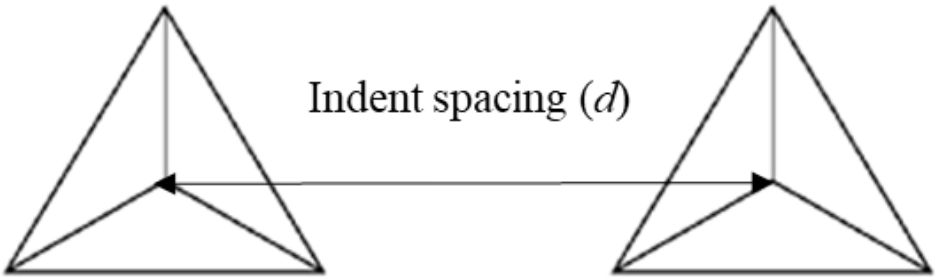

Figure 6-1 Schematic of how to measure the indent spacing (*d*) of two indents.

Current understanding within the nanoindentation community can be summarized as follows: when indents are spaced too closely together, prior indents influence the impact of future indents; if spaced too far apart, interpolation is required between indents [28]. Phani determined that a minimum, or optimal, *d/h* ratio of 10 is necessary for nanoindentation of fully dense materials [28]. However, there is no known optimal *d/h* ratio for porous materials.

For this work, indent arrays of 35x35 were performed on np-Au thin film samples at various depths and *d/h* spacing. For one set of experiments, the indent depth (*h*) was held constant, and the size of the ligament structure was varied. In the second set of experiments, the indent depth (*h*) was varied, and the ligament diameter remained constant. For both sets of experiments, the *d/h* varied between 3-20.

6.1 Results and Discussion

To create np-Au samples with varying ligament diameters, np-Au samples were annealed using a wafer curvature system (WCS). By annealing the as-dealloyed sample at 500 °C for 10 and 20 minutes, three different ligament diameters were generated and tested to determine if ligament diameter affected the optimal *d/h* ratio. These ligament diameters varied from 60-300 nm. Micrographs of the ligament as-dealloyed and after coarsening are presented in Figure 6-2.

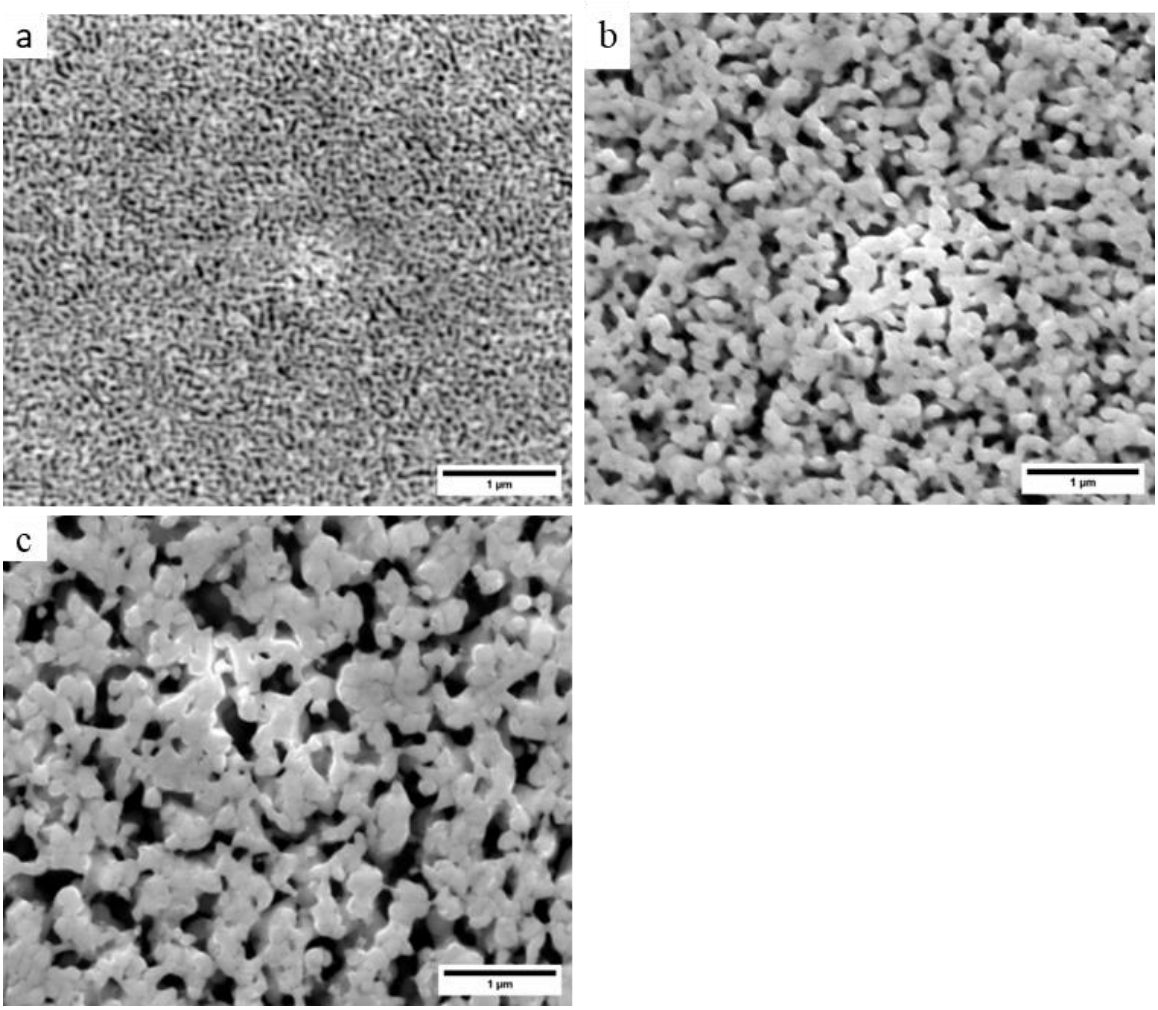

Figure 6-2 SEM micrographs of np-Au (a) as-dealloyed and after being annealed for (b) 10 minutes and (c) 20 minutes.

The original ligament diameter, as-dealloyed, was 60 nm, had a total film thickness of 1100nm, and a relative density of 40%. During heat treatment, the original ligament diameter and relative density increased, and the total film thickness decreased. Annealed for 10 minutes at 500 °C, the sample ligament diameter coarsened to 213 nm, the total film thickness decreased to 930 nm, and the relative density increased to 47%. After 20 minutes of heat treatment, the sample was further coarsened to an average ligament diameter of 300 nm, with a reduced total film thickness of 676 nm and a relative density increase of 65%.

To determine if ligament diameter had any influence on the optimal *d/h* ratio, these three samples were indented to a depth of 200 nm at *d/h* ratios ranging from 3-20 (Figure 6-3).

After the 35x35 Nanoblitz array was completed on each sample, the hardness and modulus were averaged. Any value that did not fall within 3 standard deviations of the average was removed from the data set. The results of these 1,225 indents are plotted in Figure 6-3.

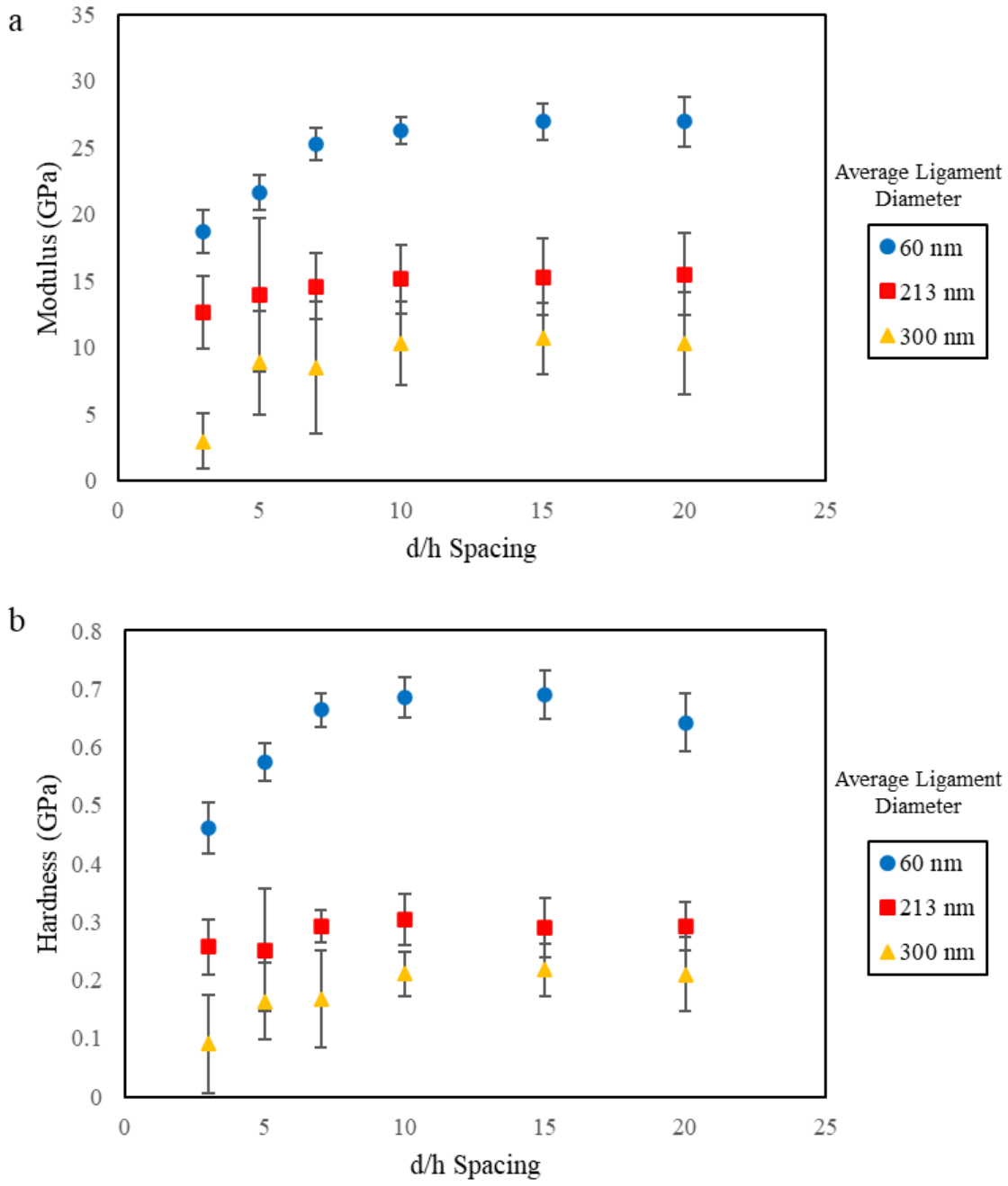

Figure 6-3 Average (a) modulus and (b) hardness of np-Au with differing ligament diameter at various *d/h* spacings. The indent depth (*h*) was held constant at 200 nm while varying the indent depth.

Both the hardness and modulus of the np-Au decreased as the ligament diameter increased. Based on the ligament size-hardness relationship posed by Briot [44], it was

expected that (i) a smaller ligament diameter would cause an increase in hardness and (ii) the ligament diameter would not influence the modulus. However, results showed an unexpected effect in that as the ligament diameter increased, the modulus decreased. It is postulated that the decrease in modulus was most likely related to the change in the relative density of the thin films. The original, as-dealloyed, film thickness was approximately 1100 nm. After 10 minutes of heating in the WCS, the film thickness decreased to 900 nm, and after 20 minutes of heating in the WCS, the film thickness decreased to 650 nm. This decrease in film thickness affected the relative density of the np-Au, and therefore potentially influenced its modulus.

The second set of experiments was conducted to determine if the indent depth influenced the optimal *d/h* ratio. Specifically, to determine the *d/h* ratio that allows for reliable nanomechanical property values and the avoidance of influence of adjacent indents. The as-dealloyed sample was indented with 35x35 arrays to depths between 100-500 nm. The average of these 1,225 indents is plotted in Figure 6-4.

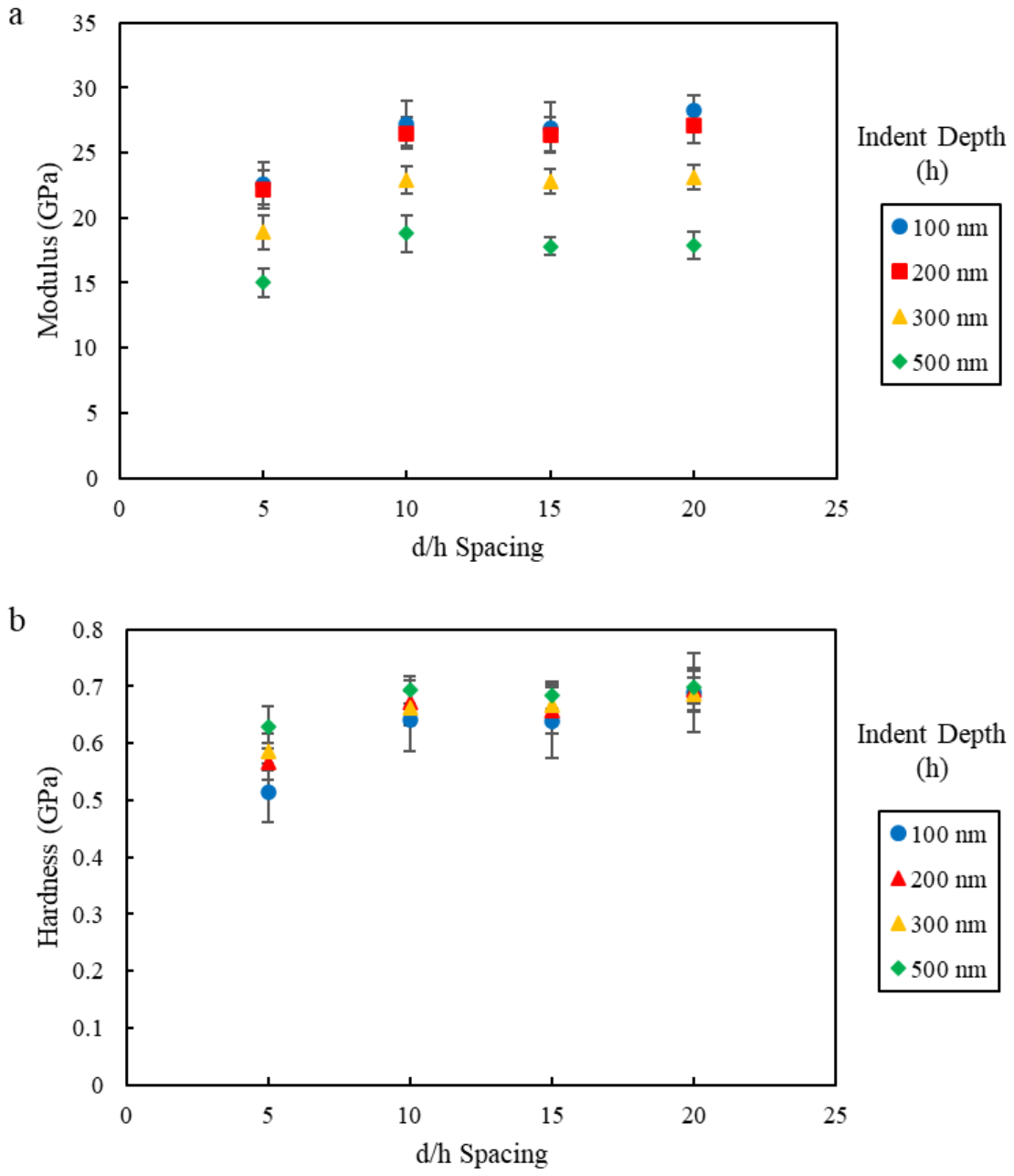

Figure 6-4 Average (a) modulus and (b) hardness of np-Au, ligament diameter of 60 nm, at various *d/h* spacings. The indent depth (*h*) varied over a range of 100-500 nm.

Similar to the results seen in Figure 6-3, there is little evidence that indent depth affects the optimal *d/h* ratio. A *d/h* ratio of 5 caused a decrease in the hardness and modulus. The decrease in these mechanical properties is due to an overlap of indents. At *d/h* ratios

of 10 and above, there was no longer an apparent *d/h* influence, as the hardness and modulus values held constant. A *d/h* spacing of 10 was determined to be the recommended spacing regardless of indent depth.

Note that to accurately determine a thin film's mechanical properties, it should not be indented to past 10% of its thickness [26]. Using the 10% rule, thin films of 1100 nm, like those used in this work, should not surpass 110 nm. However, as seen in Figure 6-4, indents to 500 nm were performed as this work studied the general trends in the hardness and modulus of the thin film. The exact hardness and modulus at each depth were not necessary for this work. Rather, the relative changes at each *d/h* were noted to determine the recommended, optimal *d/h* ratio. In both Figure 6-3 and Figure 6-4, the general trend was that the hardness and modulus values plateaued between a *d/h* ratio of 8-10. In order to better visualize and analyze this phenomenon, the mechanical properties from both sets of experiments were normalized with respect to a *d/h* ratio of 20. Plots of these normalized hardness and modulus values can be seen in Figure 6-5.

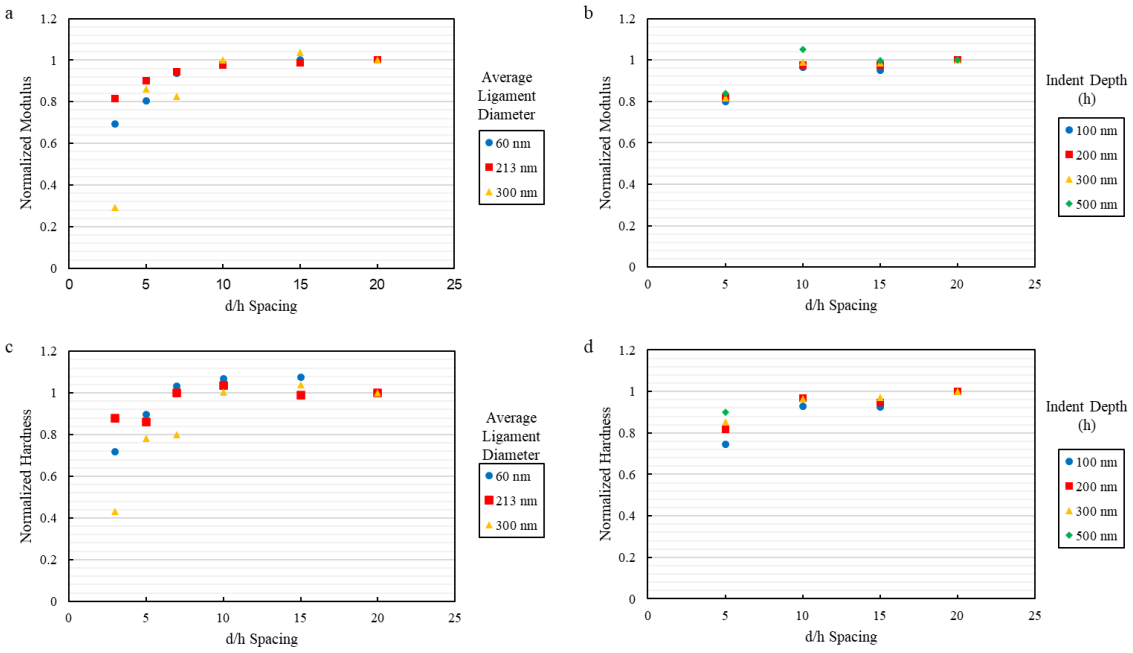

Figure 6-5 Normalized values of (a), (b) modulus and (c), (d) hardness of np-Au of different average ligament diameters and different indent depth (to vary the *d/h* values). Indent depth *h* was held constant at 200 nm while varying the indent spacing in plots (a) and (c). Indent spacing *d* was held constant while the indent depth *h* was varied in plots (b) and (d), while the depth indicated in the legend.

For both sets of experiments, the modulus and hardness were lower (and exhibited higher scatter) at smaller *d/h* ratios compared to higher *d/h* ratios. The mechanical properties at smaller *d/h* ratios increased until the hardness and modulus were independent of the *d/h* ratio. The optimal point at which the *d/h* ratio did not influence hardness and modulus measurements was *d/h* ~10. For *d/h* ratios less than 10, property values either deviated from the plateau observed at higher *d/h* or exhibited significant scatter relative to the plateau value, *e.g.*, as seen in Figure 6-5(a) and Figure 6-5 (b).

For $d/h < 10$, indents either physically overlapped or appeared to experience residual plastic strain from neighboring indents (Figure 6-6(a) and Figure 6-6(c)). For $d/h \geq 10$, mechanical properties exhibited consistent values and appeared unaffected by

adjacent indents. Specifically, mechanical properties were considered consistent and valid if they lay within 10% of the normalized values for *d/h* = 20, which was the case for *d/h* ratios of 10 or higher. It is noted that the appropriate optimal value of the recommended *d/h* ratio was the same for both experiments, *i.e.*, where either ligament diameter or indent depth was varied.

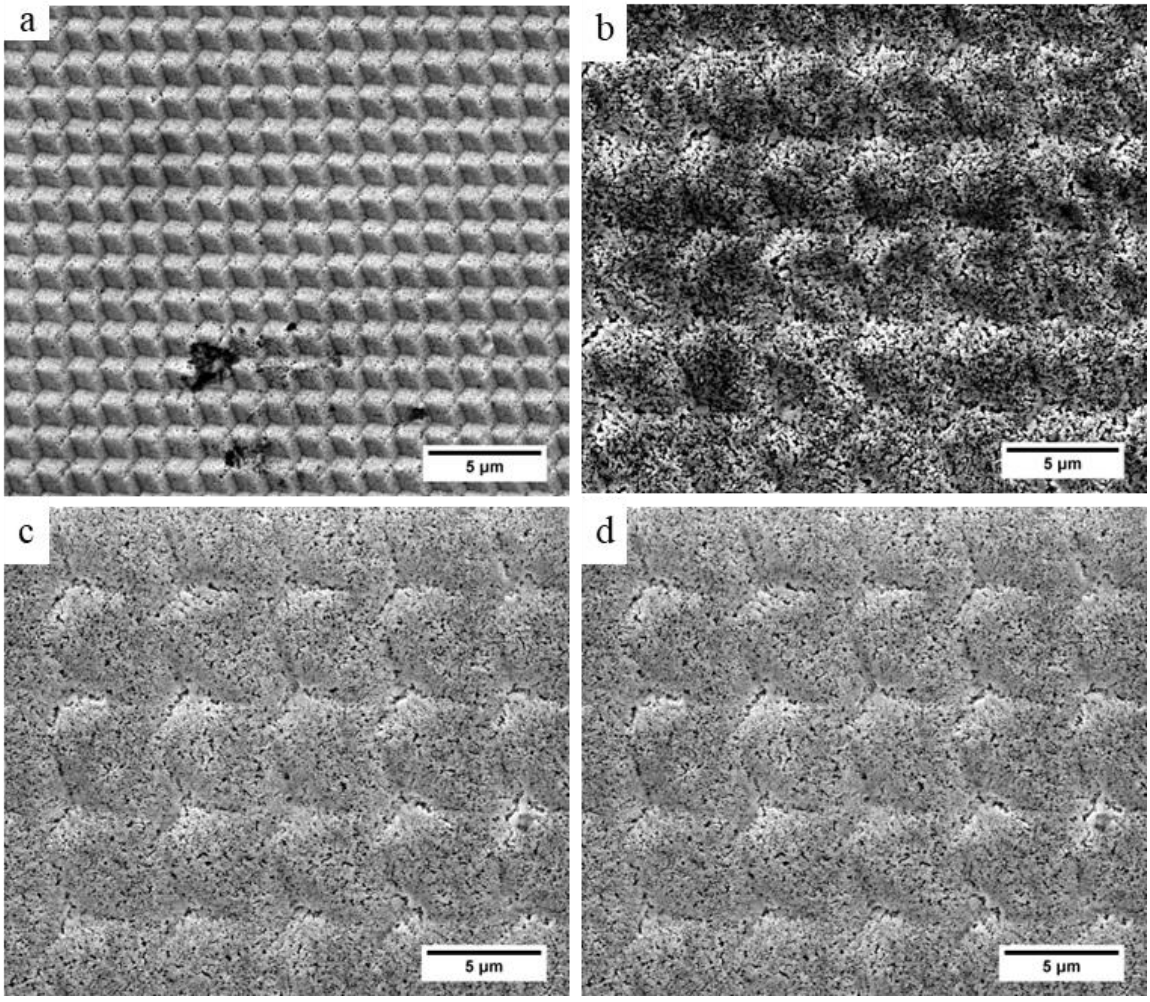

Figure 6-6 SEM micrographs of Berkovich indents with *d/h* spacing of (a) 3, (b) 8, (c) 10, and (d) 20. The indent depth (*h*) was held constant at 500 nm while the spacing between indents varied.

SEM micrographs after indentation at various *d/h* ratios are presented in Figure 6-6. Note that when indenting to a depth of 500 nm, the contact area of the tip was 7.15 μm^2,

with an indent width of 3.52 μm. For *d/h* = 3 (Figure 6-6(a)), the indents overlapped and caused the contact area of the indents to appear artificially smaller. This was caused by the indent spacing (1.5 μm) being smaller than the indent width (3.52 μm). For *d/h* = 8 (Figure 6-6(b)), the indents no longer appeared to overlap because the spacing (4 μm) was similar to the indent width. However, Figure 6-6(c) shows a slight decrease in certain hardness values for *d/h* = 8, which are attributed to an overlap of plastic deformation zones. For *d/h* = 20 (Figure 6-6(d)), the indents were well-spaced, and mechanical properties were consistent with their plateau values. However, this high *d/h* ratio required a larger total area for indentation. Specifically, the *d/h* ratio of 20 required four times the area needed for the same number of indents at a *d/h* ratio of 10 (Figure 6-6(c)). Also, as further discussed in Section 9.1, if the sample has a more complicated, less homogenous microstructure, higher *d/h* ratios would require more interpolation between indents. To minimize overlap and reduce the total area required for indentation mapping, the optimal ratio thus appears to be *d/h* = 10 for all indenting parameters.

6.2 Conclusions

Previous work on fully dense materials concluded that the minimum *d/h* ratio for nanoindentation is 10. As previous work was not performed to evaluate the optimum nanoindentation spacing for np-materials, the current study focused on finding a minimum *d/h* ratio for nanoindentation of np-Au. The optimal *d/h* ratio was determined by finding the minimum *d/h* ratio that could be performed without indents influencing the mechanical properties of adjacent indents. The minimum *d/h* ratio was determined experimentally, requiring hardness/modulus agreement within 10% of the normalized values. Based on a wide range of experiments performed on np-Au, the following conclusions are drawn:

- The optimal *d/h* spacing for np-Au is 10, *i.e.*, the experimentally determined minimum appropriate ratio of indent spacing to indent depth.
- The optimal *d/h* ratio was determined for samples that varied in ligament diameter, film thickness, and relative density. Samples ranged from 60-300 nm ligament diameter, 675-1100 nm film thickness, and 40-65% relative density. For all samples, the optimal *d/h* spacing was 10.
- The optimal *d/h* ratio was determined for indents of various depths. For indent depths between 100-500 nm, the optimal *d/h* ratio was 10.
- The optimal *d/h* ratio for np-Au was the same as Phani's recommended *d/h* ratio for fully dense materials [28].

A *d/h* ratio of 10 resulted in minimum overlap in the plastic deformation zones and minimized the total surface area needed for testing for the np-Au samples, including variations in indent depth and np length scale (ligament diameter, film thickness, the relative density). At larger *d/h* ratios, indent spacing no longer influenced the mechanical properties of np-Au. Nanoblitz 3D indent array measurements indicated that neither ligament diameter nor indent depth influenced the optimal *d/h* spacing for np-Au. This work provides a guideline for nanoindentation spacing of nanoporous (np) materials. However, further work may need to be done on other np samples to ensure this *d/h* ratio is the optimal value for all np materials.

PART II

MULTI-PRINCIPAL ELEMENT ALLOYS

CHAPTER 7. BACKGROUND OF MULTI-PRINCIPAL ELEMENT ALLOYS

Multi-principal element alloys (MPEAs) are a specific subset of alloys, containing three or more principal metallic elements. This chapter describes the basic principles of MPEAs and the material characteristics of a specific MPEA system, W-Mo-Fe-Ni alloys.

7.1 Basic Principals of Multi-Principal Element Alloys

Most alloy systems contain only one principal element, with other elements added to modify the properties of the principal element [14]. MPEAs contain multiple principal elements to improve one or more properties. These properties include, but are not limited to the following [13, 14, 77-83]:

- Elevated- temperature strength
- Elevated-temperature oxidation resistance
- Elevated-temperature low neutron resistance
- Higher impact strength
- Higher electrical resistance and magnetic permeability

These properties are essential for numerous applications, including materials for engines, nuclear equipment, tools, light transportation, structural materials, and high-frequency communication equipment. [13].

Most alloy systems are comprised mainly of one or perhaps two principal elements. The atomic makeup of these alloys is almost entirely comprised of the principal element(s) with the addition of relatively small amounts of other elements [84]. The concept of fabricating alloys containing more than two principal elements is fairly new, thus requiring an evolution of nomenclature and terminology. MPEA is the overarching term for an alloy

system with more than two principal elements, however, there are subsets of alloys within this broad, overarching category. Some researchers categorize alloys with multiple principal elements based on the entropy of mixing introduced into the system. For example, alloys with 3 or 4 principal elements are known as medium entropy alloys (MPEs), and alloys containing 5 or more principal elements are known as high entropy alloys (HEAs) [13, 84, 85]. This work will focus on MPEAs in general.

MPEAs allow for a new strategy of alloy development which increases the number of possible alloy systems. To understand how many possible alloy systems are created when additional principal elements are introduced, the law of combinations (Equation 7-1) can be used [85, 86]:

$$N = \frac{(c+n-1)!}{(c-1)!n!} \qquad \text{Equation 7-1}$$

Where N is the number of possible combinations, c is the number of components, x is the variation specification (*i.e.*, amount of change to the allowed-1%, 0.1%, etc.) for each component, and $n=100/x$. To illustrate the magnitude of possible combinations, a ternary system (3 elements), with 60 elements (or components) to choose from, and a material specification of x=0.1% (n=1000), would result in over 10^{11} different combinations [85].

In addition to the number of principal elements present in MPEAs, there are also three core characteristics of an MPEA: (1) sluggish diffusion, (2) severe lattice distortion, and (3) cocktail effects [87]. Sluggish diffusion refers to the diffusion coefficients of the MPEA being lower than the single elements that comprise the MPEA [87, 88]. It has been proposed that the higher activation energy and slower diffusion in MPEAs are due to the large variation of lattice potential energy (LPE) among lattice sites. Specifically, the low LPE sites act as traps and suppress atomic diffusion [88].

The atomistic size differences in the elements present cause severe lattice distortion. An alloy system with multiple principal elements creates complex crystal structures. Figure 7-1 demonstrates the complexities added when five principal elements are used in body-centered cubic (BCC) and face-centered cubic (FCC) crystal structures.

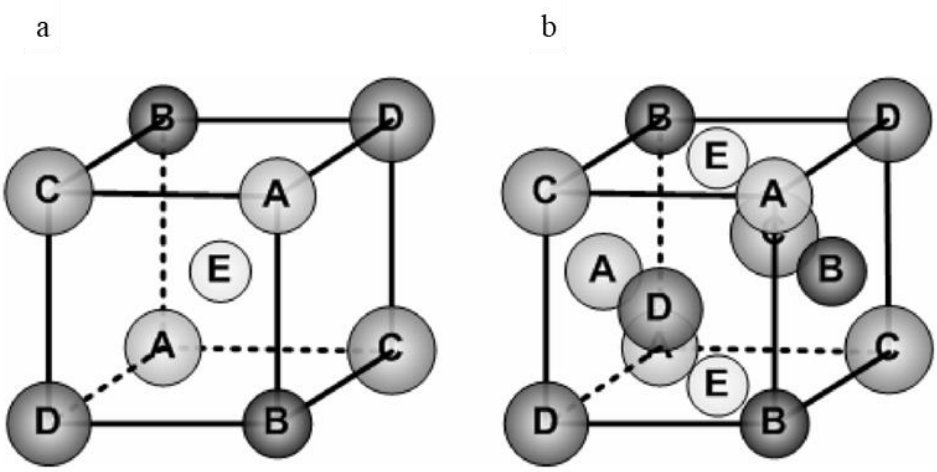

Figure 7-1 Schematic of (a) BCC and (b) FCC crystal structures with five principal elements (reproduced from [89]).

The distortion in the lattice crystal structure occurs because the difference in atomic sizes of the principal elements induces strain to maintain the crystalline configuration.

The complexities and strain within the crystal structure of MPEAs can cause distortion when characterized by X-ray diffraction (Figure 7-2).

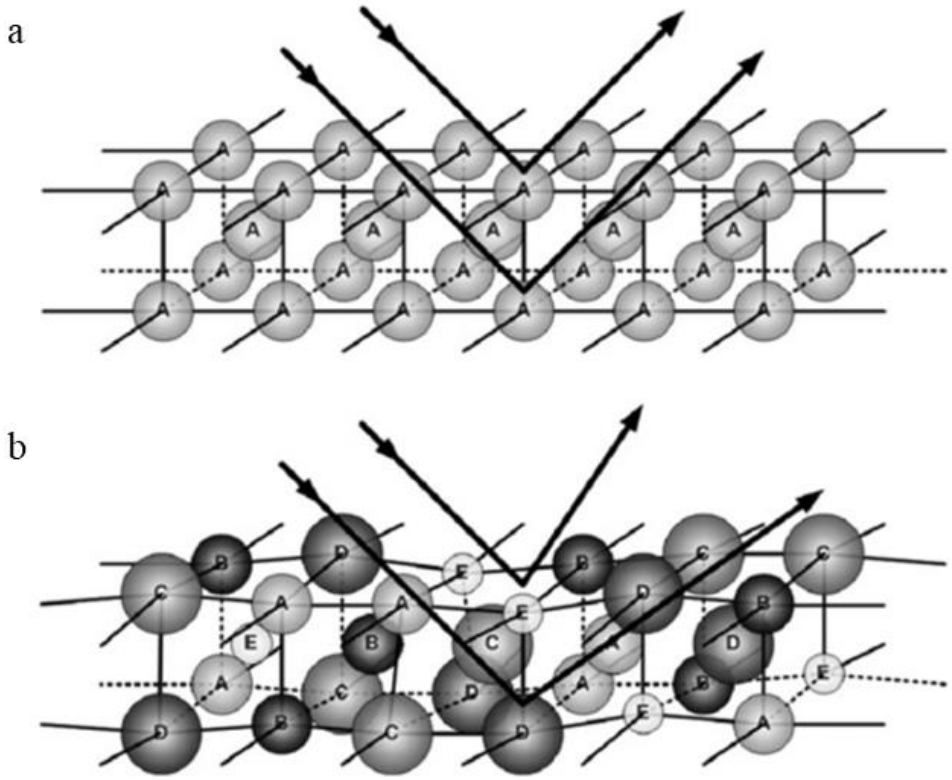

Figure 7-2 Schematic of intrinsic lattice distortion on Bragg's diffraction on (a) a perfect lattice composed of the same atoms and (b) a distorted lattice with five different atoms, all in varying sizes, randomly placed in the crystal lattice (reproduced by [87]).

Figure 7-2 is based on Yeh's 2007 X-ray diffractometry work on the CuNiAlCoCrFeSi alloy system [90]. It is hypothesized that the lattice distortion causes the higher strength and increased brittleness of MPEAs as compared to a single element or a single principal element system [87, 91-93]. The increase in hardness may be attributed to a mismatch in shear modulus between atoms [13]. The lattice distortion also leads to changes in the alloy's thermal, electrical, optical, and chemical behavior [13, 89].

The term cocktail effect is a term borrowed from the field of acoustics. When used in the context of caustics, the term describes one's ability, or rather inability, to focus on a single speaker among a mixture of conversations and background noise [87]. For metallic alloys, the cocktail effect refers to properties found in a mixture that were not present in

the singular elements comprising the alloy [87]. The cocktail effect describes the non-linear and unexpected results that arise from the combination of multiple elements with complex microstructures [13]. The cocktail effect was first mentioned by Ranganathan in 2003 [94] and has been corroborated by subsequent work [92, 95, 96]. One particular cocktail effect is the high specific strength of MPEAs compared to other materials (Figure 7-3)

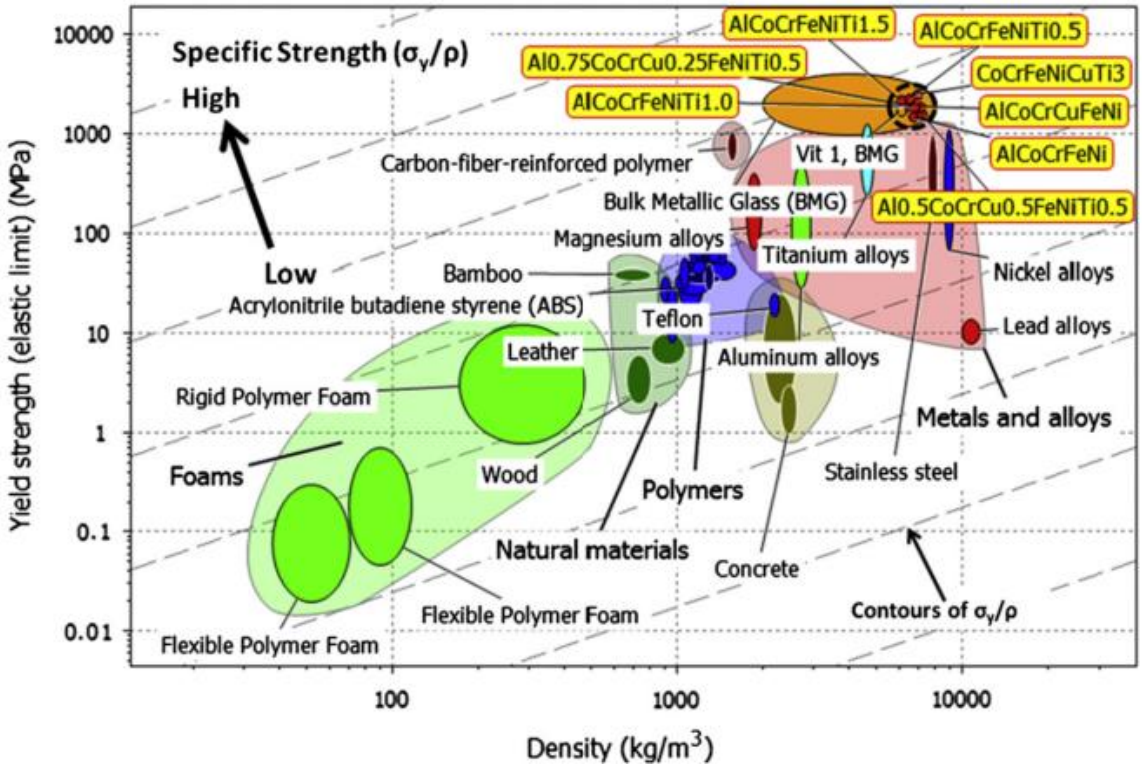

Figure 7-3 Yield strength versus density of MPEAs (black, dashed circle) compared to other materials (reproduced from [87]).

Figure 7-3 demonstrates that MPEAs have the highest specific strength as compared to other materials, including single-element metals and alloys. The MPEA alloys are within the black circle at the top right-hand side of Figure 7-3. Specific MPEA alloy systems are highlighted in yellow.

It should be noted that due to the vast number of possible alloy combinations, MPEAs are under-studied and require additional research to better understand their complexities. However, one of the more famous and well-studied MPEA systems is the single-phase FCC Cantor alloy as it is one of the first documented MPEAs [13].

The Cantor alloy, or equiatomic CrMnFeCoNi, is a single-phase FCC alloy discovered by Vincent and Cantor in the late 1970s/early 1980s [85]. The Cantor alloy is stabilized by its high configuration entropy, the multiplicity and complexity of local atomic configurations, and associated lattice strains [85]. The Cantor alloy has excellent mechanical properties that exceed some of the highest strength steels and Ni superalloys [85]. Mechanical studies have shown that the single-phase FCC Cantor alloy results in higher yield stresses, high and more extended work hardening rates, and delayed necking compared to pure FCC metals [85]. The differences in mechanical behavior have been linked to the local lattice distortion which restricts dislocation nucleation and motion [85].

Because of its high strength, the Cantor alloy and variations of this alloy are the subject of many studies. New alloy systems were created by adding, removing, or replacing a single element of the Cantor alloy (CrMnFeCoNi). Some of these new alloys add to or replace one of the principal elements of the Cantor with Al, Ti, Cu, or Nb [85]. Due to the number of principal elements present, and the slight changes in composition that can be made to the Cantor alloy, millions of alloy systems can be synthesized and studied.

When considering the type of modifications that can be made to an alloy system containing multiple principal elements, it is important to consider the Hume-Rothery rules [83, 85, 97]:

1. Solvent and solute atoms have similar atomic sizes.
2. The atom must have the same crystal structure.
3. Solvent and solute atoms have similar valence.
4. Solvent and solute atoms have similar electronegativity.

Other researchers expand on this list to include the Ω-parameter (Equation 7-2), which correlates to the melting point, the total entropy of mixing, and the total enthalpy of mixing [13, 15, 77, 91, 98]:

$$\Omega = \frac{(\Sigma c_i T_{m,i})(S)}{|H|} \qquad \text{Equation 7-2}$$

where c is the atom fraction, T_m is the melting temperature, S is the entropy of mixing, and H is the enthalpy of mixing. The subscript i denotes the element for the atom fraction and melting temperature.

Adhering to the Hume-Rothery rules increases the probability of solubility between atoms [85]. When a solute and solvent do not obey the Hume-Rothery rules, they will exhibit limited or no solubility, resulting in one or more compounds [85].

To increase solubility, the solvent and solute atomics must be similar in size to minimize the lattice strain [21]. As a general rule, to be considered atomically similar, the solvent and solute must have atomic radii within 15% of each other. The crystal structure must be the same; otherwise, a second phase with a different structure would arise [21]. The valences must also be similar because differences in valence electrons encourage the formation of compounds rather than solutions [21]. Finally, without similar electronegativity, compounds will also be formed. Some researchers combine Hume-Rothery rules 3 and 4 because differences in valence and electronegativity result in the formation of compounds [85].

These rules guide the understanding of how different elements mix or don't mix and form different crystal structures. When there is a small amount of solubility between elements, different phases can form and add to microstructural complexities.

7.2 Multi-Principal Element Alloys in Literature Reviews

As previously discussed, there are millions of potential alloy combinations within the category of MPEA. As a result, multiple authors have put together literature reviews of MPEAs to help understand some of the nuances of multi-principal alloys. A summary of several of the literature reviews is addressed here.

In 2017, Miracle wrote a literature review and compared various MPEA alloy systems to help understand why the research into MPEAs has been, to date, limited [13]. The review considered 408 different and distinct MPEAs composed of 37 different elements. Of those 37 elements, the most common were Al, Co, Cr, Cu, Fe, Mn, Ni, and Ti. These elements appeared in over 100 of the alloy systems under review. Co, Cr, Fe, and Ni appeared in over 70% of the alloy systems [13]. Based on the specific elements and the relative atomic percentages, each of the 408 MPEAs had their own specific complex microstructure. Differences were also noted in the phases of these MPEAs: 33% were single-phased, 45% had two phases present, 16% had three phases present, and the remaining 6% had either four, five, or six phases present [13].

In 2021, Cantor wrote a literature review on multicomponent Cantor alloys (*i.e.*, alloys that are a variant of the original Cantor alloy, CrMnFeCoNi) [85]. This review looked at single-phase FCC alloys made by adding to, replacing, removing, and/or reducing the elements found in the original Cantor alloy [85]. The variations included making an alloy system that is equiatomic with four or six elements (*i.e.*, removing Mg or adding Cu),

replacing one of the key elements with another metallic element (*i.e.*, replacing Mg with Cu), or moving away from the equiatomic composition with the original five elements (*i.e.*, increasing the amount of Ni present). The key takeaways from this literature review included the wide range of variations that could be applied to the Cantor alloy system, the complexity of the local atomic environment, the increased entropy of mixing of these alloy systems, and some of the potential uses of these alloys given their resulting mechanical, chemical, and electrical properties [85].

Because of the vast number of MPEA alloy systems (with only a fraction of those addressed by Miracle's or Cantor's literature review) and the vast areas of study (*i.e.*, mechanical, thermal, or electrical properties), Tang chose to focus his work on the dynamic mechanical behaviors of specific MPEA systems [99]. In 2023, Tang reviewed 61 distinct MPEA systems and their dynamic-mechanical properties [99]. Tang began his literature review with an overview of the theoretical models of the dynamic-mechanical behaviors of MPEAs. The classical understanding of plastic flow under dynamic conditions was modeled by Johnson and Cook (J-C model) [100]. The J-C model is a mathematic expression for the flow stress under uniaxial stress at room temperature (Equation 7-3):

$$\sigma = (A + B\varepsilon_p^n)(1 + Cln(\frac{\dot{\varepsilon}}{\dot{\varepsilon_0}})[1 - \left(\frac{T-T_r}{T_m-T_r}\right)^m] \qquad \text{Equation 7-3}$$

where σ is the uniaxial dynamic flow stress, ε_p is the uniaxial plastic strain, $\dot{\varepsilon}$ is the strain rate, $\dot{\varepsilon_0}$ is the reference strain rate (10^3/sec), *A*, *B*, and *C* are parameters, *n* is the strain hardening exponent, *m* is the model constant, T_m is the melting temperature, and T_r is a reference temperature (298 K).

The J-C model for flow stress under uniaxial stress at room temperature can be modified to include density (ρ), specific heat (C_p), and a material constant (*P*) (Equation 7-4) [101].

$$\sigma = (A + B\varepsilon^n)[1 + \left(\frac{\dot{\varepsilon}}{C}\right)^{\frac{1}{P}}]\exp\left[\frac{-0.9\left(1+\left(\frac{\dot{\varepsilon}}{C}\right)^{\frac{1}{P}}\right)}{(\rho C_p(T_m - T_0)}\left(A\varepsilon + \frac{B\varepsilon^{n+1}}{n+1}\right)\right) \quad \text{Equation 7-4}$$

Equation 7-4 has been known to agree with experimental results of various MPEA systems such as Al-Cr-Fe-Co-Ni alloys, CrMnFeCoNi, $AlTi_{0.5}Cr_{1.5}Fe_{1.5}CoNi$, and Ti-Zr-Nb-Mo-Hf-Ta alloys.

Other models have been derived for the dynamic flow stress (σ) of MPEAs, including the Zerilli-Armstrong (A-Z) model (Equations 7-5 and 7-6) [102] and the Khan and Liang (KHL) model (Equation 7-8) [103]:

$$\sigma = \left(C_1 + C_2\varepsilon_p^P\right)\exp\left[T(C_3 ln\dot{\varepsilon} - C_4)\right] \quad \text{Equation 7-5}$$

$$\sigma = \hat{Y}exp(-\beta_3 T + \beta_2 T ln\dot{\varepsilon}) + B\varepsilon^n + Y_1 \quad \text{Equation 7-6}$$

where C_1, C_2, C_3, C_4, P, β_3, β_2, B, and n are material constants, T is 298.15K, $\hat{Y}$ is the threshold yield stress, and Y_a represents the temperature-independent stress. Equation 7-5 and Equation 7-6 are A-Z models for FCC and BCC MPEAs, respectively. The KHL model for BCC metals is as follows:

$$\sigma = (A + B\varepsilon_p^{n0}\left(1 - \frac{ln\dot{\varepsilon}}{lnD_0^P}\right)^{n1})(\exp(Cln\dot{\varepsilon}))(1 - \left(\frac{T - T_r}{T_m - T_r}\right)^m) \quad \text{Equation 7-7}$$

where *n0* is the strain hardening exponent, *m* is related to thermal softening, and *n1* is a stress-strain exponent.

Understanding MPEAs under dynamic loads is necessary for potential uses as bulletproof armor and projectiles for high-speed damage [99]. Equiatomic WMoFeNi is an MPEA that has the potential for use as a high-speed projectile. Section 7.3 discusses some prior research on the characterization, mechanical properties, and mechanical behavior of WMoFeNi.

7.3 W-Mo-Fe-Ni Alloy Systems and Adiabatic Shear Banding

The work referenced in Part II of this work focuses on the W-Mo-Fe-Ni alloy system. This section mainly focuses on equiatomic WMoFeNi, an MPEA system that is equiatomic, multi-phased, and exhibits high density and high penetration depths. The high density and high penetration depths are typical of W-heavy and other refractory element alloys, and therefore, are generally utilized in high kinetic energy penetrators [104]. Adding Mo to W heavy alloys containing Fe and Ni results in increased strength of the alloy [105]. The more Mo added to a W-Fe-Ni alloy, the higher the hardness and tensile strength. However, increases in Mo content decrease the ductility within the matrix and overall alloy [105].

One main difference between W-heavy alloys and equiatomic WMoFeNi is that equiatomic WMoFeNi is known to "self-sharpen" when used as a projectile and results in a higher penetration depth (Figure 7-4) [104, 106, 107]. The term "self-sharpening" describes a material that is capable of maintaining its acute head shape during penetration instead of exhibiting the typical "mushrooming" effect of most alloy systems, including W-heavy alloys [106, 108]. Depleted uranium (DU) has historically been used for its self-sharpening characteristics; however, due to the environmental contamination DU causes, a replacement material is necessary [106, 109].

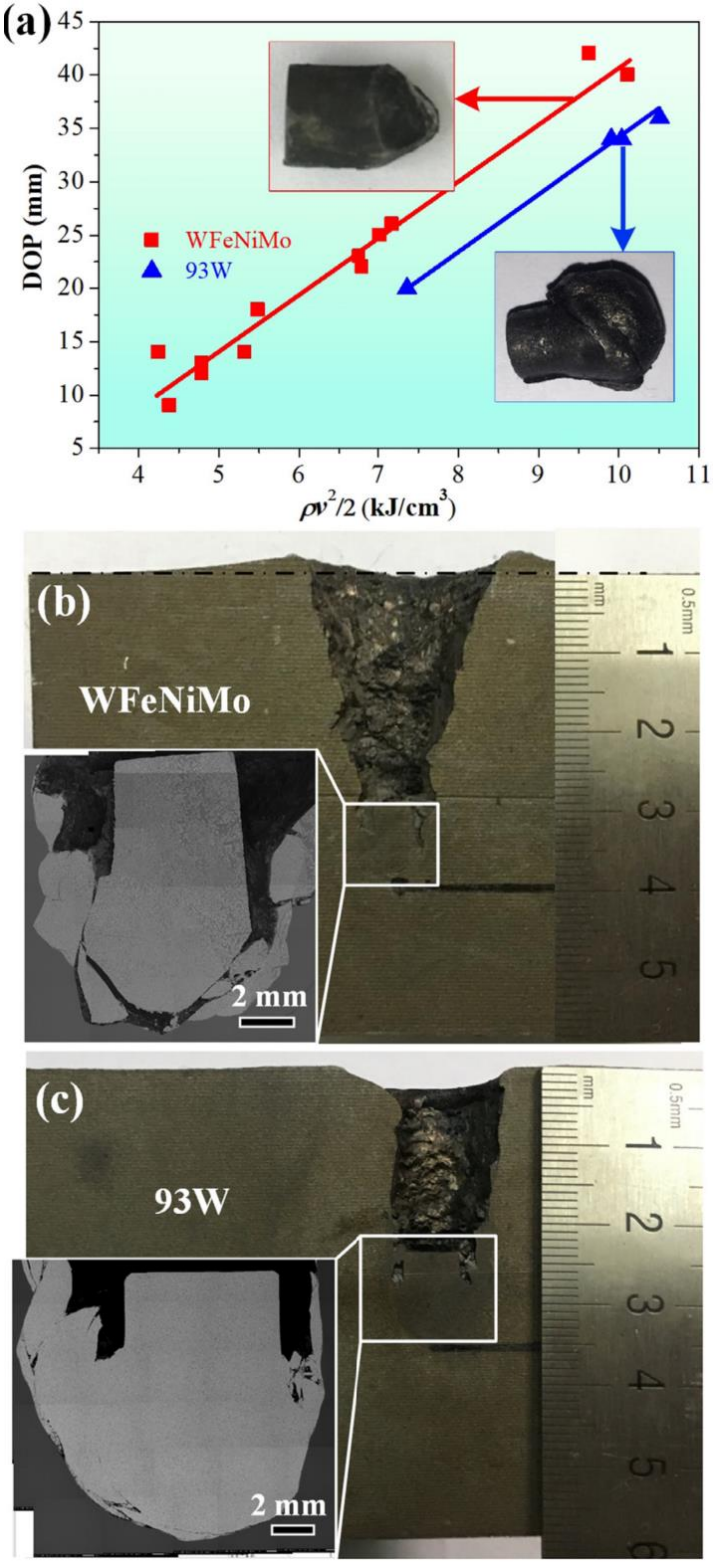

Figure 7-4 Previous work done showing how certain MPEAs keep their acute shape during penetration. The figure shows (a) the penetration of depth (DOP) of equiatomic WMoFeNi and a W-heavy alloy versus the kinetic energy per volume ($\rho v^2/2$) and the penetration depths of (b) WMoFeNi (c) 93W (reproduced from [106]).

Figure 7-4 shows the penetration depth of a WMoFeNi and a W-heavy alloy sample. At the same kinetic energy, the WMoFeNi sample penetrated deeper because it did not exhibit the mushrooming or blunting observed for the W-heavy alloy [106]. W heavy alloy samples were used for comparison purposes as they have a relatively high density and are frequently used as a projectile [110]. It has been shown that WMoFeNi alloys penetrate 10-20% deeper than the conventional W-heavy alloy [107].

Self-sharpening behavior has been attributed to adiabatic shear banding (ASB) which occurs along the direction of maximum shear stress when a viscoplastic material undergoes dynamic or impact loading [111]. The formation of ASB is typically found in metallic structures and causes rapid shearing when under impact conditions and leads to catastrophic failure due to concentrated shear deformation [112-114]. The failure mechanism occurs when a shear band is followed by a crack which is propagated through the shear band [115].

Chen found that the self-sharpening behavior in WMoFeNi only occurs when its velocity exceeds a certain threshold [116]. He reported that the WMoFeNi projectile penetration mode changed from mushrooming to self-sharpening between velocities of 1330-1531 m/s [116]. It has been hypothesized that ASB occurs in WMoFeNi because of deformation that occurs in its soft matrix phase which becomes pinned by the harder mu (μ) phase (Figure 7-5) [106].

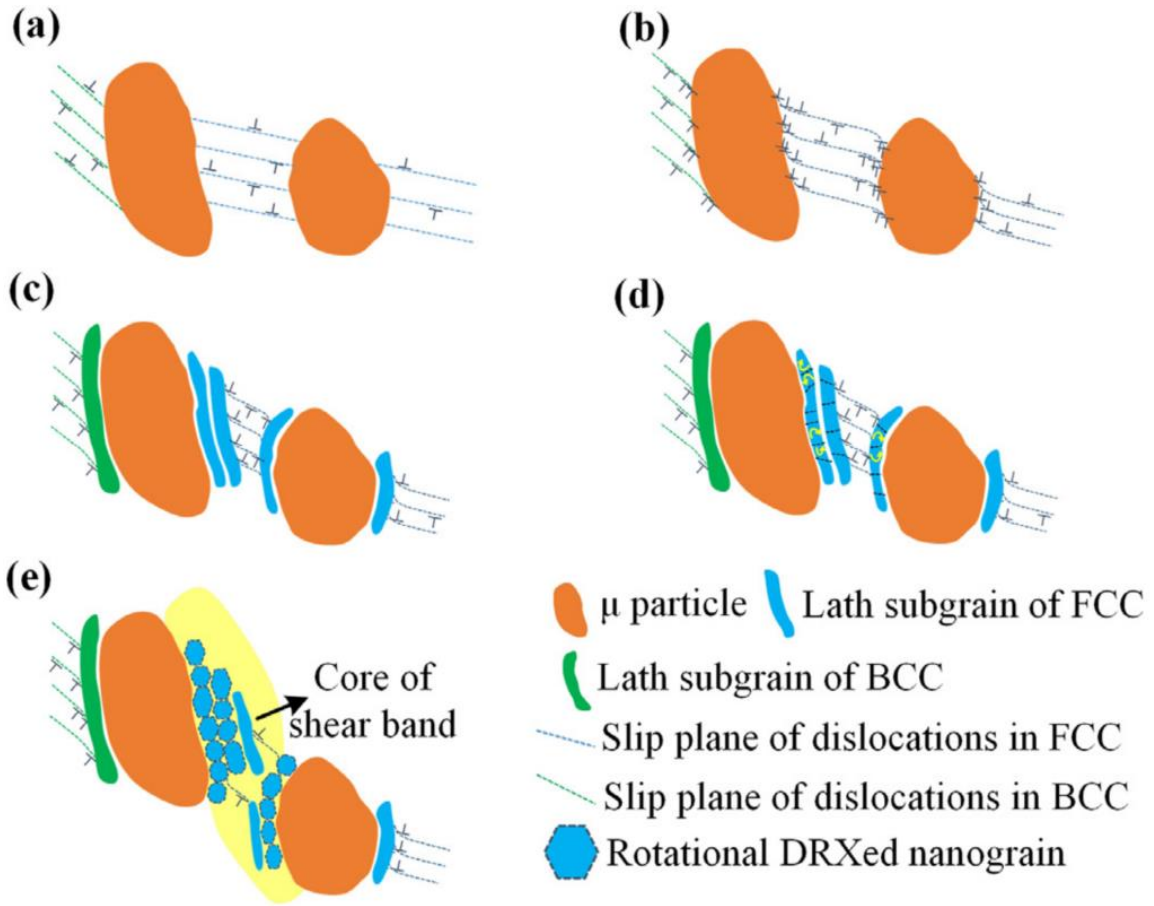

Figure 7-5 Schematic of shear banding in WMoFeNi showing (a) the initial microstructure with low dislocation density before deformation (b) formation of strain gradient near the phase boundaries (c) dislocations continual accumulation at the μ phase (d) elongation of lath subgrains and (e) formation of shear band (reproduced from [106]).

Figure 7-5 is a schematic created by Liu [106] to show the formation of shear bands that initiate self-sharpening behavior. The μ phase (shown in orange) dispersed throughout the FCC matrix causes inhomogeneous deformation and higher strain gradients stimulating the dynamic recrystallization that leads to shear band formation [106]. Dynamic recrystallization is often observed in conjunction with ASB [117]. Chen also noted the deformation beginning in the FCC matrix for self-sharpening W [116]. Note that Figure 7-5 shows ABS for the specific equiatomic WMoFeNi alloy which contains three different

phases (FCC matrix, BCC dendrites, and a μ phase). Another important note is that the FCC matrix in WMoFeNi alloys is softer than the μ phase [106].

To potentially increase the amount of ABS occurring in W-Mo-Fe-Ni alloys, additional work was performed done to enhance its μ phase. This work included the annealing of W-Mo-Fe-Ni samples to allow for precipitation strengthening [107]. In 2023, Li found that annealing an as-cast sample of $W_{30}Mo_7FeNi$ for 30 hours at 650 °C caused drastic differences in the tensile behavior (Figure 7-6) [107].

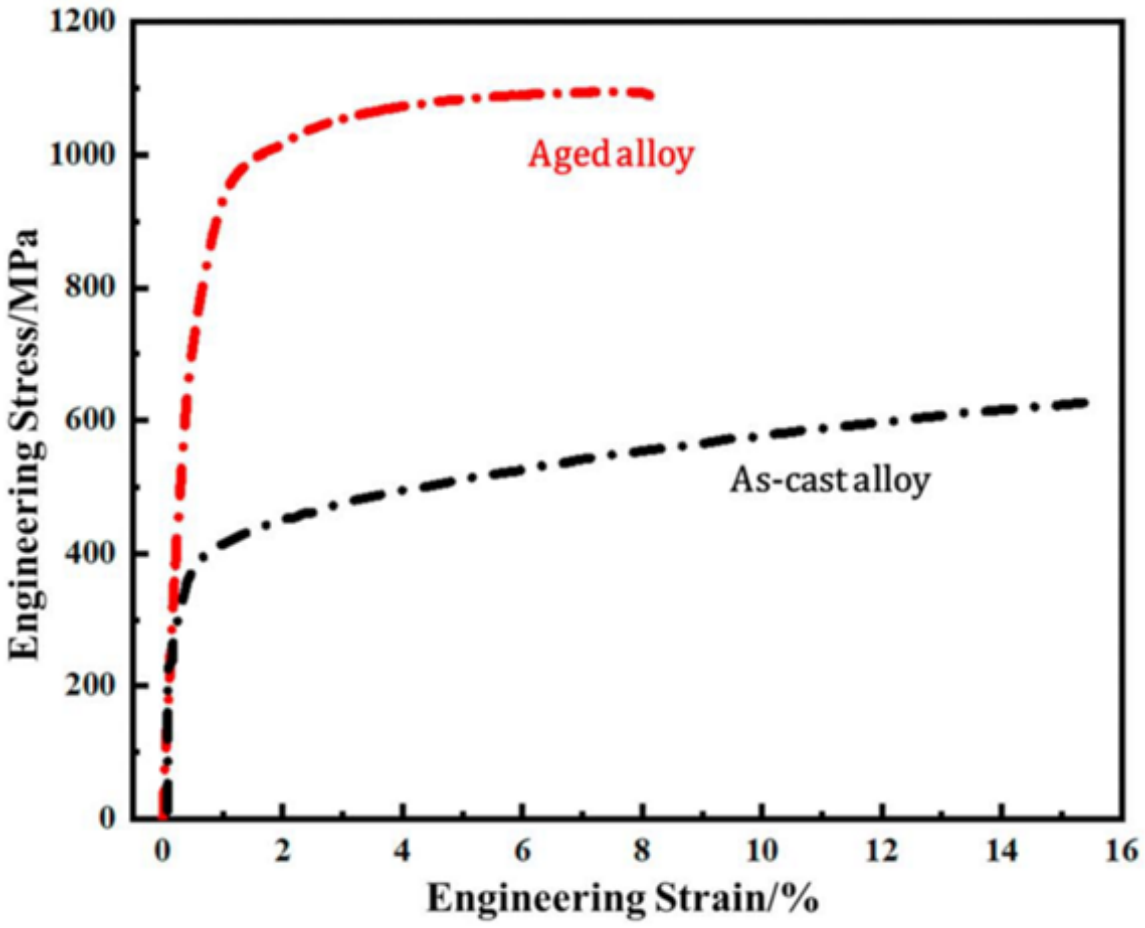

Figure 7-6 Quasi-static tensile test of $W_{30}Mo_7FeNi$ alloy comparing the as-cast alloy to annealed alloy (reproduced from [107]).

Annealing the sample for 30 hours at 650 °C resulted in the yield strength increasing from 350 MPa (as-cast) to 950 MPa. However, the ductility decreased from 15% to 8% [107]. While these tensile tests are promising, further experiments need to be conducted on this annealed sample to determine if the self-sharpening and penetrative properties were improved.

In 2021, Chen's continued research provided a theoretical hypothesis of the self-sharpening behavior of W-based MPEAs when used for penetration testing at various impact velocities [108]. His analysis derived a predictive model of the nose structure (*i.e.*, the tip of the penetration that hits the surface first) based on the instantaneous impact velocity and the penetration velocity. Chen's model predicted whether the nose structure would exhibit self-sharpening or mushrooming based on the dynamic stress the penetration caused. In order to determine the nose radius evolution, Chen's self-sharpening model used a nose self-sharpening coefficient derived from experimental results [108]. The nose self-sharpening coefficient was used to model the radius decrease as the projectile penetrated to deeper depths [108].

ASB has been found in various MPEA alloy systems when loaded under dynamic compression conditions. ASB is a crucial failure mechanism that occurs in WMoFeNi, which leads to self-sharpening behavior. While models and schematics of ABS in WMoFeNi have been proposed, further research is necessary to understand this failure mechanism. To aid in the understanding of ASB in WMoFeNi alloys, other MPEA systems that exhibited ABS should be studied.

In 2016, Dirras found that TiHfZrTaNb experienced dynamic recrystallization and the formation of ASB under high-impact velocities [118]. This alloy system had a yield

strength dependent on the strain rate. The yield strength was about 40% higher when the strain rate was 10^3/sec compared to when the strain rate was 10^{-3}/sec [118]. In 2020, Gwalani found similar results for alloy systems containing Al, Co, Cr, Fe, and Ni [119]. Similar to WMoFeNi, $Al_{0.7}$CoCrFeNi is a multi-phase system composed of an FCC phase and a harder second phase. The deformation of $Al_{0.7}$CoCrFeNi occurred within the FCC phase [119]. Many other MPEA systems formed ASB under dynamic compression. These MPEA systems include AlCoCrFeMnNi, CrMnFeCoNi, AlCoCrFeNi, TiZrNbV, AlCoCrFeNiMoC, and AlCrFeNiV [120-126].

The current theory under consideration by the MPEA community is that ASB in WMoFeNi occurs due to deformation in the FCC matrix that is pinned by the harder μ phase. ASB occurs in MPEA systems with various microstructure and phase compositions. Under dynamic loads, ASB was noted in MPEAs with the various phase(s): FCC, BCC, FCC + precipitants, FCC + BCC, FCC + BCC + precipitants, and FCC/BCC + precipitants [99]. It is interesting to note that ASB was also observed in single-phase MPEAs, which contradicts Liu's theory of ASB in WMoFeNi as that theory relies on WMoFeNi having two phases with different hardness values [106].

The following is a predictive model where the formation of ASB occurs if the equation is equal to or less than zero [99]:

$$\frac{d\tau}{d\gamma} = \left(\frac{d\tau}{d\gamma}\right)_{\dot{\gamma},T} + \left(\frac{d\tau}{d\gamma}\right)_{\gamma,T}\frac{d\dot{\gamma}}{d\gamma} + \left(\frac{d\tau}{dT}\right)_{\dot{\gamma},\gamma}\frac{dT}{d\gamma} \leq 0 \qquad \text{Equation 7-8}$$

where the shear stress (τ) is a function of stress (σ) and shear strain (γ) is a function of strain (ε) at a constant rate.

$$\tau = \frac{\sigma}{2} \qquad \text{Equation 7-9}$$

$$\gamma = \sqrt{2e^{2\varepsilon} - 1} - 1$$ Equation 7-10

These equations can allow us further insight as to how ASB occurs in projectile testing of various MPEAs including, W-Mo-Fe-Ni alloys. These models of the mechanical behavior are based on experimental results of MPEAs and classical models. Tang concluded that the dynamic deformation of MPEAs generally leads to ASB due to the lattice distortion seen in MPEAs [99].

As indicated by the recent dates of the above-referenced works, the understanding of ASB in MPEAs is still in its infancy. Work on ASB in MPEAS has only been published within the last ten years with the majority being published within the last five years. The following chapter continues the work done on W-Mo-Fe-Ni alloys to understand their mechanical behavior through nanoindentation and bulk compression tests.

CHAPTER 8. MATERIALS AND METHODS

The following section describes the methodologies utilized in the fabrication, characterization, and mechanical testing of MPEA samples, specifically W-Mo-Fe-Ni alloys. Note that the additional characterization and mechanical testing of these samples discussed here were performed using the same methodologies described in CHAPTER 2.

8.1 Synthesis of W-Mo-Fe-Ni Alloys via Arc Melting

Electric arc furnaces can melt and cast metals. They allow for high temperatures and are commonly used when creating alloys with refractory metals [127]. Electric furnaces have the unique ability to provide exact molten metal temperatures [127].

The Arcast 200 Cold Crucible Arc Melting Furnace and Casting Module was used to form MPEA samples. This Arcast 200, employed at the University of Kentucky, has one circular, three rectangular, and one long cylindrical cavity. The circular cavity was used for pure Ti as it helps remove oxygen from the chamber. The three rectangular cavities were used for making large samples, which were then cut into smaller samples for compression testing. The cylindrical cavity was used for making the samples for tensile testing as it provides a large enough volume to cut tensile samples. Table 8-1 details the compositional breakdown of the three samples used throughout Part II.

Table 8-1 Compositional breakdown of MPEA samples used in Part II of this work.

Sample Name	W (at %)	Mo (at %)	Fe (at %)	Ni (at %)
Equiatomic WMoFeNi	25	25	25	25
FCC Composition	5	15	40	40
μ Composition	10	29	34	27

The equiatomic sample was the primary sample used in Part II. The FCC and μ composition samples are compositional variations of W-Mo-Fe-Ni alloys and were used to assess their microstructural differences compared to the equiatomic sample.

8.2 X-Ray Diffractometry

X-ray diffractometry (XRD) is a characterization technique used to identify the long-range order of crystalline materials and the short-range order of non-crystalline materials [128]. XRD is a nondestructive technique that can isolate and help identify the different phases of samples [20]. XRD is based on X-ray wavelength interference when interacting with a crystalline structure. XRD is based on Bragg's Law (Equation 8-1), the basic law of diffraction [20, 129]:

$$n\lambda = 2dsin\theta \qquad \text{Equation 8-1}$$

where $n\lambda$ is the phase difference with n being an integer, λ is the wavelength of the X-ray, d is the plane spacing within a crystal, and θ is the incident angle. The diffracted X-rays are detected, processed, and counted. Samples were scanned through a range of 2θ angles so all possible diffraction directions of the lattice are attained [129]. A schematic of an XRD is diagrammed in Figure 8-1.

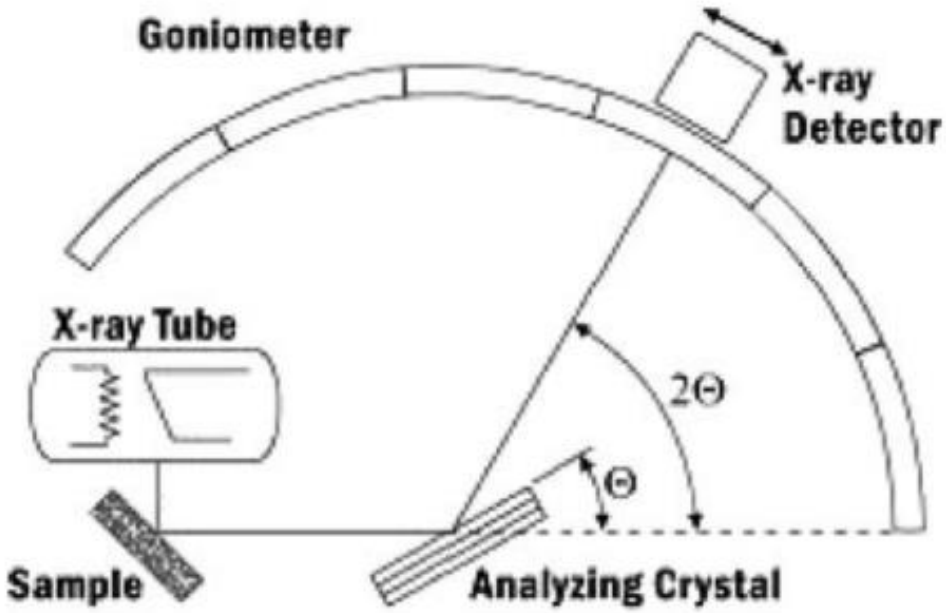

Figure 8-1Schematic of diffractometer system (reproduced from [129]).

Crystalline materials have a three-dimensional regularity of atoms, which form the crystal structure [128]. These crystal structures are based on one of the fourteen Bravais lattices. With the use of Bragg's law and the d spacing (Equation 8-2), the crystal structure can be determined (reproduced from [20]).

$$d_{hkl} = \frac{a}{\sqrt{h^2+k^2+l^2}} \qquad \text{Equation 8-2}$$

Where a is the lattice parameter and h, k, and l are the Miller indices. When determining the crystal structure, knowing which Miller indices can be observed is important in identifying the crystal structure. Some of the rules of extinction (*i.e.*, which crystal structures are allowed, and which are forbidden) are outlined in Table 8-2.

.

Table 8-2 Structure extinction rules for the crystallographic plane (hkl) [20].

Lattice Type	Diffraction Possibly Present	Diffraction Forbidden
Simple	All	None
Base-Centered	h and k are unmixed	h and k are mixed
Base-Centered	(h+k+l) are even	(h+k+l) are odd
Face-Centered	h, k, and l are unmixed	h, k, and l are mixed

Mixed and unmixed diffraction possibilities refer to the Miller indices values in the *h*, *k*, or *l* space that are even or odd. If *h* and *k* are both even or both odd, the indices are unmixed. However, if *h* is even and *k* is odd (or vice versa) then the indices are mixed. Structure extinction refers to the interference between scattering atoms in a crystal unit cell. If there is more than one atom in a unit cell, the intensity from certain crystallographic planes can become extinct due to interference between atoms on different planes [20]. The detectable crystallographic planes for BCC are (1 1 0), (2 0 0), (2 1 1), (2 2 0), etc., and for FCC are (1 1 1), (2 0 0), (3 1 1), (2 2 2), etc.

For this work, a Thermo ARL Equinox 100 or a Bruker D8 Advance was used at the University of Kentucky to perform XRD and crystal analysis of the W-Mo-Fe-Ni samples.

8.3 Gleeble

The Gleeble, which allows for physical simulations, was designed and constructed by Dynamic Systems Inc (DSI). DSI was founded over 50 years ago and manufactures equipment that allows for physical simulations [130]. In addition to characterizing different material properties, physical simulation can aid in the design of manufacturing systems and the development and optimization of production processes [131]. The Gleeble applies

thermal and mechanical stresses on samples and it is a useful tool in the study of metallurgical processes, the development of new materials, and the evaluation of industrial processes [130].

A Gleeble 3500 Thermomechanical Stimulator (Figure 8-2) was used for this work.

Figure 8-2 Gleeble 3500 Thermomechanical Simulator (photograph courtesy of Alyssa Stubbers).

The Gleeble at the University of Kentucky has two units: the main control unit and the hydrowedge unit. The main control unit is used for heating, tension tests, compression tests, and strain-induced crack opening tests. The hydrowedge simulates rolling and compressing testing. Samples can be heated with induction or resistive heating. However, for this work, compression tests were conducted at room temperature.

CHAPTER 9. MECHANICAL BEHAVIOR OF THE COMPLEX MICROSTRUCTURE OF W-MO-FE-NI ALLOY SYSTEMS

This section discusses the mechanical behavior of the individual phases of W-Mo-Fe-Ni alloys as well as bulk samples. Three samples (equiatomic WMoFeNi, μ composition, and FCC composition) with varying amounts of W, Mo, Fe, and Ni were created and compared using characterization and mechanical property techniques. Each W-Mo-Fe-Ni alloy sample exhibited three phases: FCC, BCC, and μ phase. XRD (Figure 9-1) and SEM (Figure 9-2) were used to characterize the distinct crystal patterns and morphology of each phase.

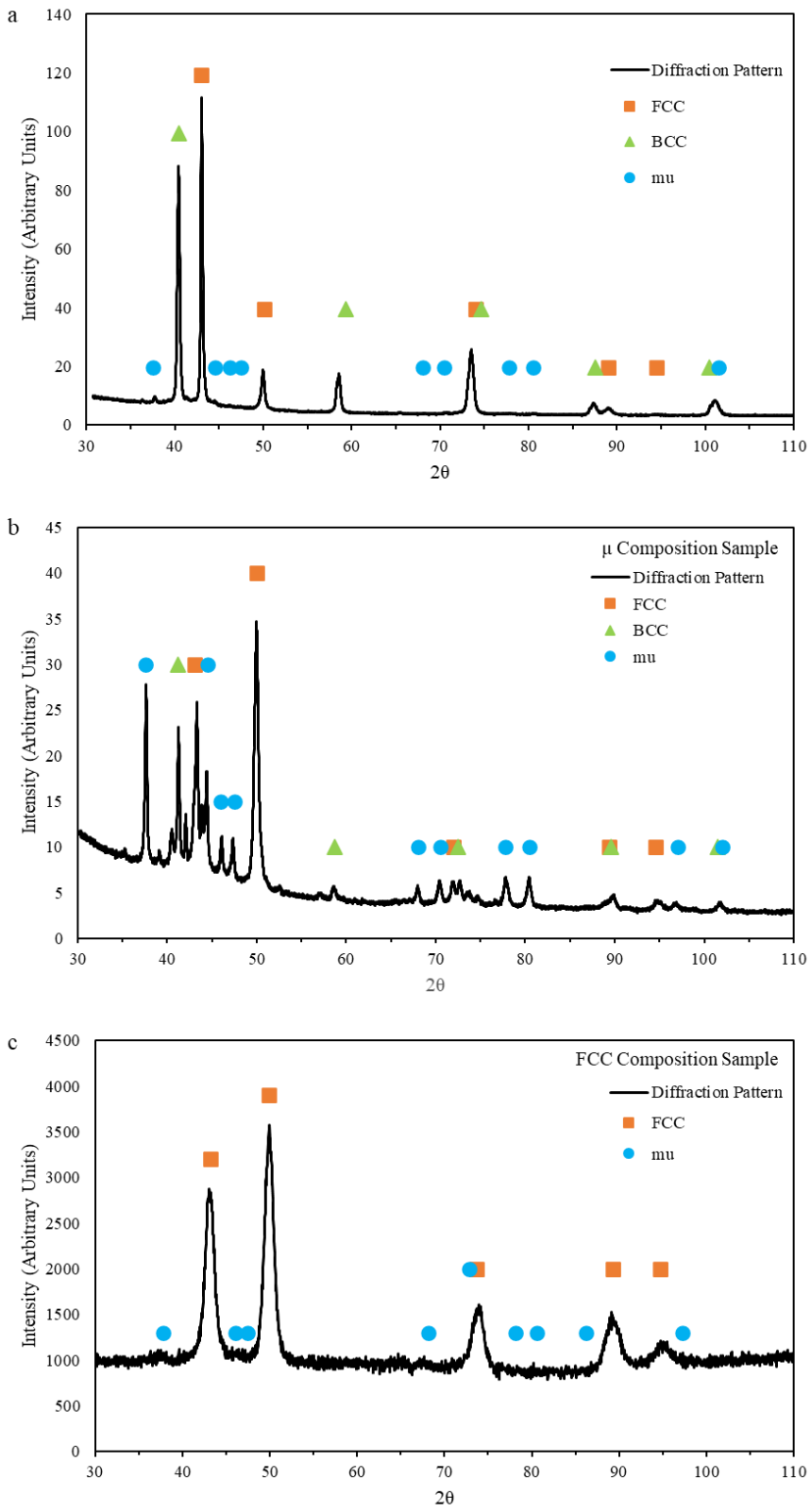

Figure 9-1 XRD scan of W-Mo-Fe-Ni alloy samples (a) equiatomic WMoFeNi, (b) μ composition, (c) FCC composition (figure courtesy of Michael J. Detisch).

In Figure 9-1, the green triangles denote the BCC for the (1 1 0), (2 0 0), (2 1 1), and (2 2 0) planes. The orange squares denote the FCC peaks for the (1 1 1), (2 0 0), (2 2 0), (3 1 1), and (2 2 2) planes. The peaks that do not correspond with the planar peaks for BCC or FCC structures are assumed to be the μ phase and are represented by the blue circles. To date, the μ phase crystal structure has not been identified, however, it is hypothesized to resemble a rhombohedral crystal structure.

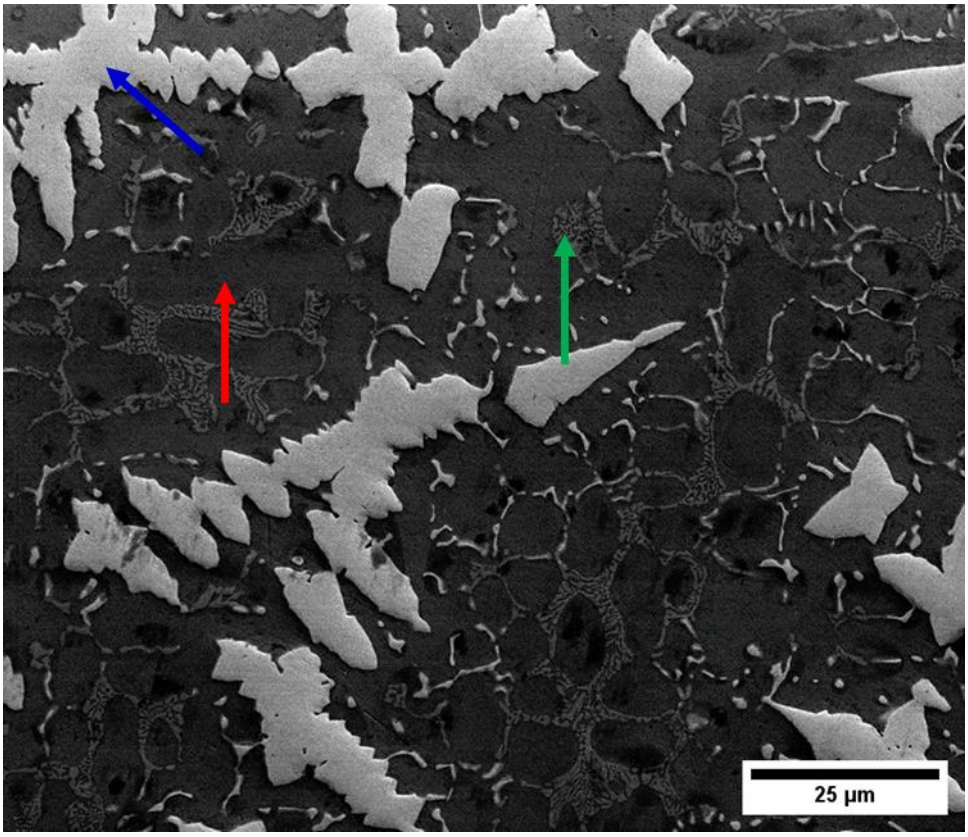

Figure 9-2 SE micrograph of the equiatomic WMoFeNi sample (figure courtesy of Alexandra Allamon).

In Figure 9-2, the blue arrow points to the BCC phase, the red arrow points to the FCC phase, and the green arrow points to the μ phase. The BCC phase is comprised of dendritic structures, the FCC phase is the matrix of the sample, and the μ phase has a lamellar structure.

Each phase within the sample varies in length scale, thus creating its complex microstructure. For example, the lamellae of the μ phase are nanometers in length while the BCC dendrites are microns in length. The FCC matrix is interspersed throughout the sample. Note that while the lamellae and dendritic structures are the most common structures in the sample, there are smaller BCC phase regions that are encapsulated by the μ phase. The blue arrow in Figure 9-3 references a BCC phase encapsulated by the μ phase.

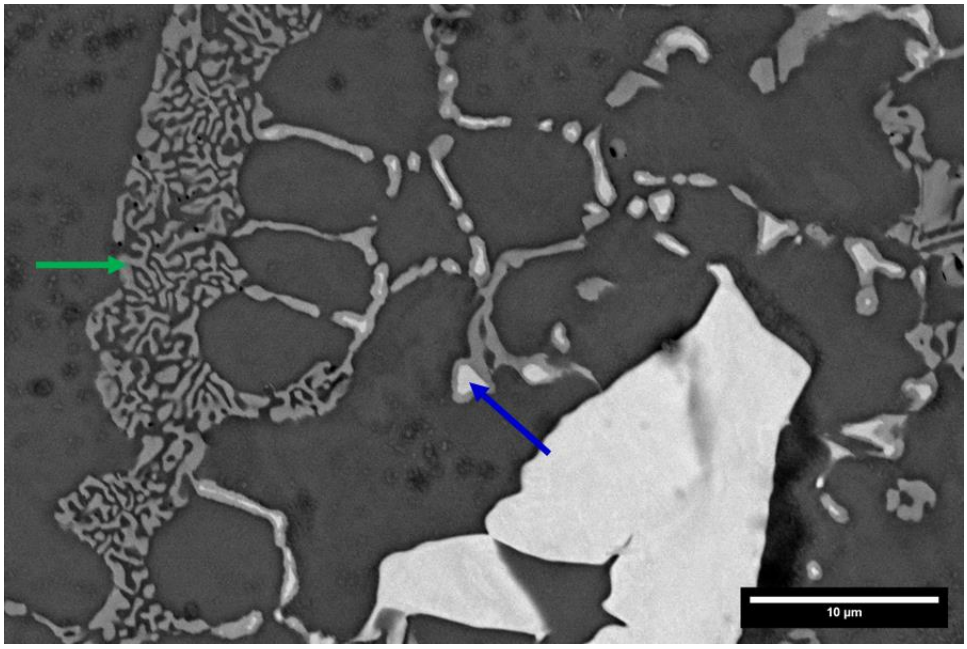

Figure 9-3 BSE micrograph of the equiatomic WMoFeNi sample at increased magnification.

Similar to Figure 9-2, the blue arrow in Figure 9-3 points to W-rich regions encased in μ phase, and the green arrow points to the μ lamellae structure. This micrograph is at a higher magnification than Figure 9-2 to better show the lamellae structure of the μ phase.

Each phase within the sample comprises different atomic percentages of W, Mo, Fe, and Ni. EDS analysis mapped the elemental composition of each phase Figure 9-4.

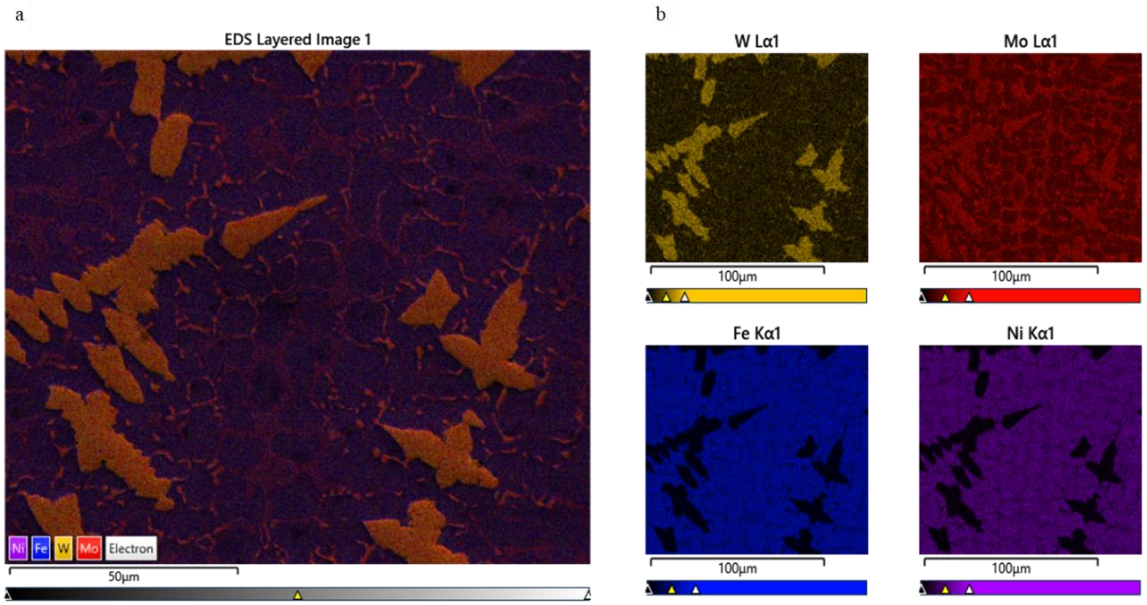

Figure 9-4 EDS composition maps of the equiatomic WMoFeNi sample where (a) has all four elements (W, Mo, Fe, Ni) overlapped and (b) has individual elemental maps shown (figure courtesy of Alexandra Alloman).

The three phases of the equiatomic WMoFeNi sample are distinctly observed in the elemental map (Figure 9-4). The elemental breakdown of each phase is shown in Table 9-1.

Table 9-1 Atomic percentage of W, Mo, Fe, Ni in each phase of the equiatomic WMoFeNi sample.

Phase	**W (at %)**	**Mo (at %)**	**Fe (at %)**	**Ni (at %)**
W Dendrite	57	38	4	1
FCC Matrix	6	13	40	41
μ Phase	10	29	41	27

The majority of the W dendrite is composed of W, with a lesser amount of Mo and small traces of Fe and Ni. The FCC matrix is equally composed of Fe and Ni, with lesser amounts of Mo, and small amounts of W. The μ phase has Fe as its main element, closely followed with similar amounts of Mo and Ni and lesser amounts of W.

It is hypothesized that WMoFeNi's self-sharpening behavior is caused by deformations occurring in the FCC matrix, which are then pinned by the harder μ phase. Since this hypothesis is dependent on the mechanical properties of the phases present in WMoFeNi, their mechanical properties are further explored in Section 9.1.

9.1 Mechanical Properties of W-Mo-Fe-Ni Alloys' Individual Phases

The mechanical properties of each phase within WMoFeNi's complex microstructure were measured using Nanoblitz 3D and 4D. The resulting mechanical property maps show relative differences in hardness and modulus.

9.1.1 Nanoblitz 3D

To further understand the properties of the three phases of the W-Mo-Fe-Ni alloy samples, indent arrays of at least 50x50 indent array were performed, with each indent array set to a depth of 50nm or 200 nm and a d/*h* ratio of 10. In order to create a high-resolution mechanical property map, the equiatomic sample was indented to a depth of 50 nm (Figure 9-5).

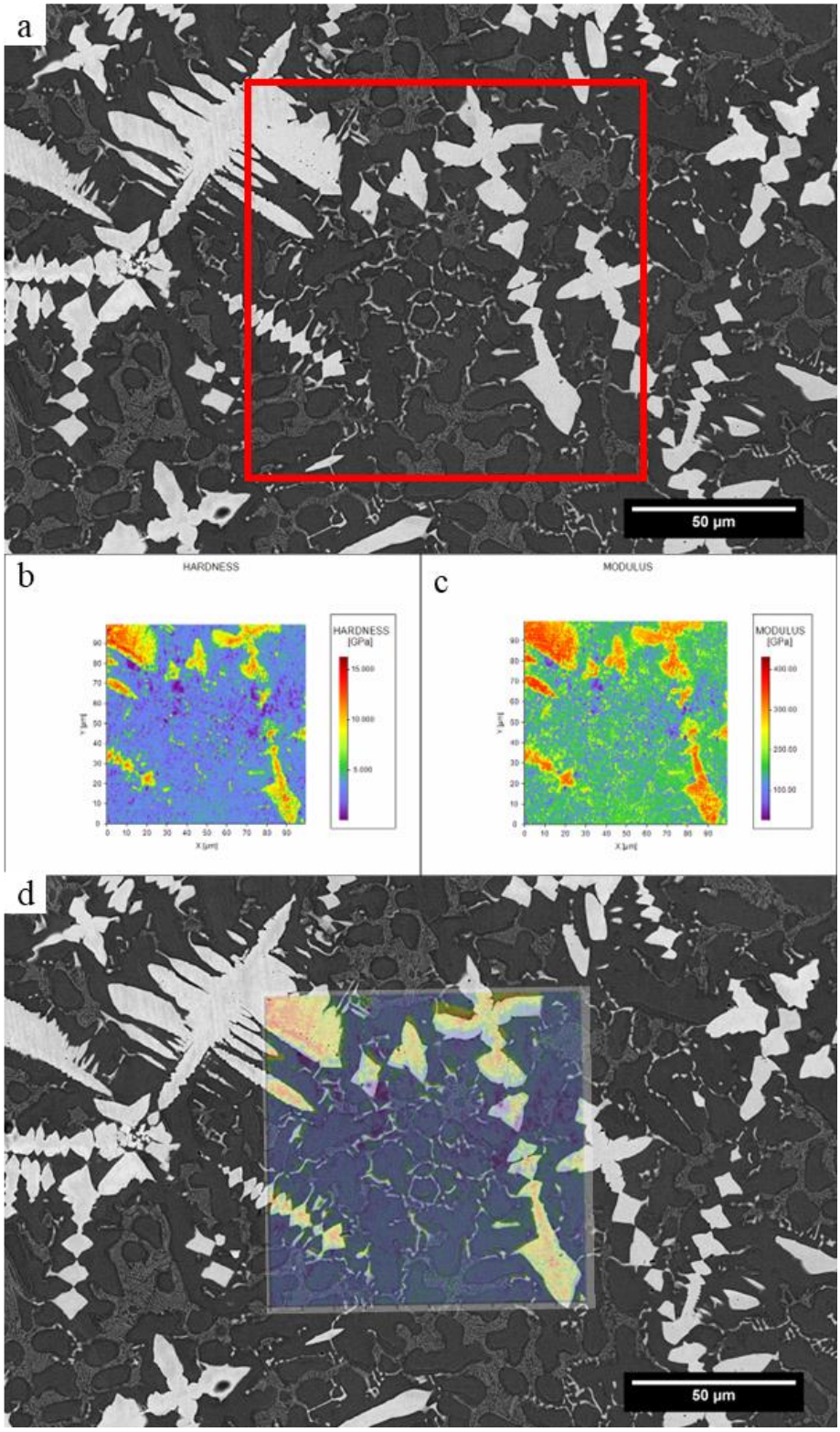

Figure 9-5 Composed of (a) BSE micrograph of WMoFeNi after indentation where the indent array is within the red box, heat maps of (b) hardness and (c) modulus for a 200x200 indent array to 50 nm in depth, and (d) an overlay of the hardness map on the BSE micrograph.

The hardness and modulus heat maps in Figure 9-5(b) and Figure 9-5(c) are remarkably similar to the SEM micrograph (Figure 9-5(a)), with the outline of the W dendrites easily visible. Note that the heat maps vary in color from blue to red, with blue indicating a lower value and red indicating a higher value. Specifically, the red regions on the hardness map indicate a relatively high hardness, and the blue regions indicate a relatively low hardness. The modulus heat map employs the same color schemes and represents similar relative values.

Due to their higher hardness and modulus, the W dendrites are prominently displayed in red. However, it is more difficult to distinguish between the differences in mechanical properties of the FCC matrix and the μ phase. In the hardness map, the FCC matrix is mainly blue with some small areas of yellow and green. These yellow and green areas are either the μ phase or small W regions. Due to the visual similarity between the green and yellow coloring, it becomes even more difficult to see the differences in the modulus map, with the FCC matrix shown in green and the μ phase shown in yellow.

To provide a more quantitative understanding of each phase, deeper indents were performed to obtain an average hardness and modulus for each phase. These larger indents assist in making one-to-one comparisons between the indents and points on the mechanical property heat maps. Figure 9-6 shows Nanoblitz 3D results for indents going to a depth of 200 nm rather than 50 nm depth as depicted in Figure 9-5.

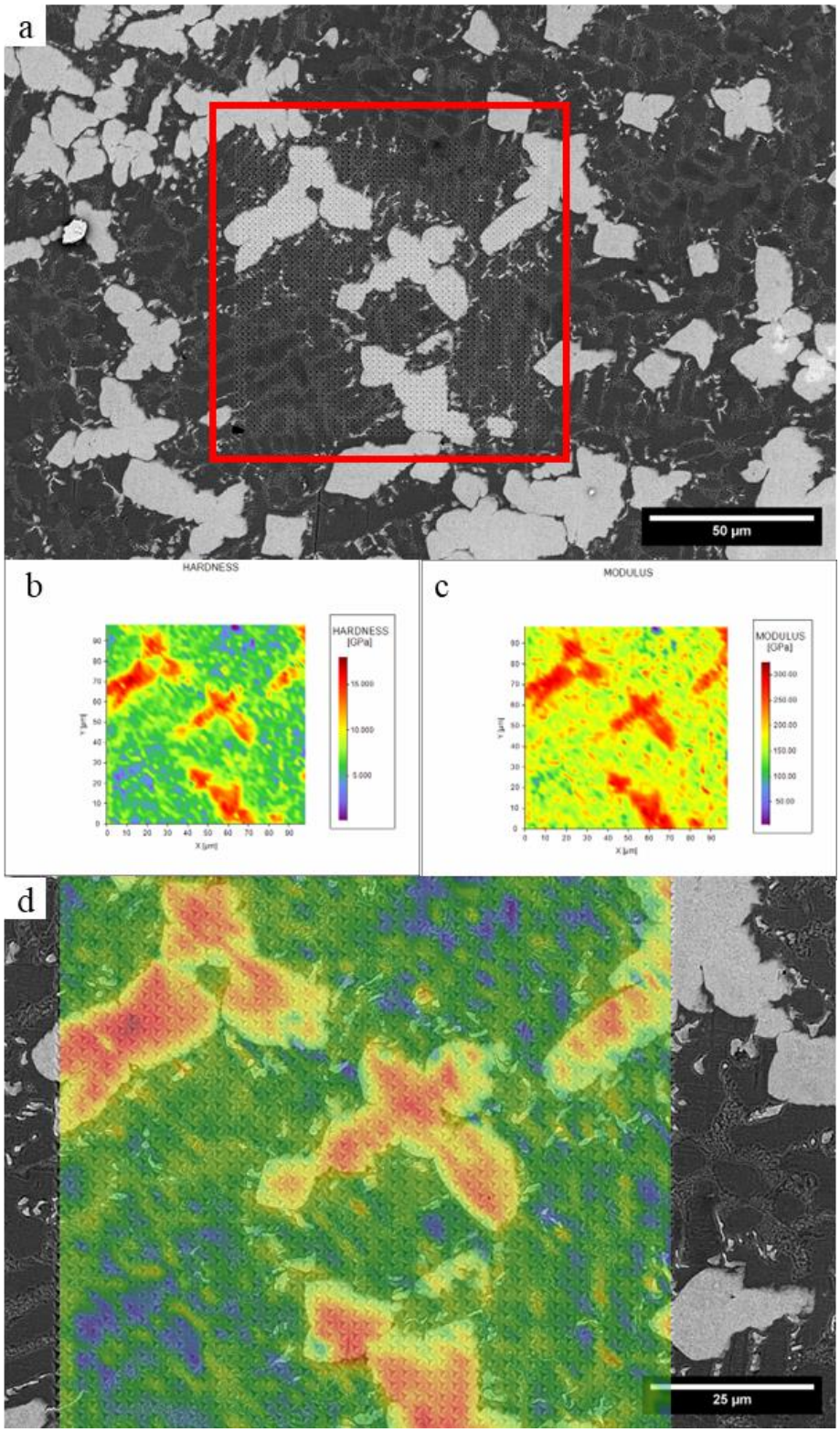

Figure 9-6 Composed of (a) BSE micrograph of WMoFeNi after indentation where the indent array is within the red box, heat maps of (b) hardness and (c) modulus for a 50x50 indent array to 200 nm in depth, and (d) an overlay of the hardness map on the BSE micrograph.

Due to the deeper indents, the heat maps in Figure 9-6 do not have as high a resolution as the heat maps in Figure 9-5. The reduction in resolution occurs because as the indents become deeper, the elastic and plastic deformation zones around the indents also increase, resulting in a larger area of influence on the mechanical properties reported for each indent. The increase in deformation zones can cause changes in mechanical properties as indents may cause a composite response rather than a singular response to the individual phase. However, deeper indentation allows for the matching of individual indents from the heat maps to indents on the BSE micrograph. Since the Berkovich tip is pyramidal, each indent left a triangular area that is visible in the top-down view of the sample. From the top-down view, as the indent depth increased, the triangular area, or contact area, became larger. These triangular areas helped identify which indents were fully in one phase and which indents covered two or more phases. This identification process is explained in Appendix 3. Each indent was carefully identified as to which phase(s) it encompasses and manually selected to find the average mechanical properties of each phase. At least 50 indents per phase were used to calculate the average hardness and modulus which are presented in Table 9-2.

Table 9-2 Average hardness and modulus of each phase seen in the equiatomic WMoFeNi sample.

Phase	**Hardness (GPa)**	**Modulus (GPa)**
W Dendrite	12.5 +/- 1.9	240 +/- 35
FCC Matrix	5.9 +/- 1.1	154 +/- 17
μ Phase and FCC Matrix	6.8 +/- 1.2	176 +/- 22

Table 9-2.

Table 9-2 illustrates that the W dendrites were the hardest phase with an average hardness of 12.5 GPa, and the FCC matrix was the softest phase with an average hardness of 5.9 GPa. Interestingly, based on previous research by Liu [106], it was expected that the μ phase would be the hardest. However, the hardness of the μ phase was only slightly higher than the FCC matrix at 6.8 GPa. This lower hardness was due to indents being larger and wider than the actual μ phase (Figure 9-7). The larger indents resulted in the properties extrapolated from the indent to be a composite response of both the μ lamellae and the FCC matrix.

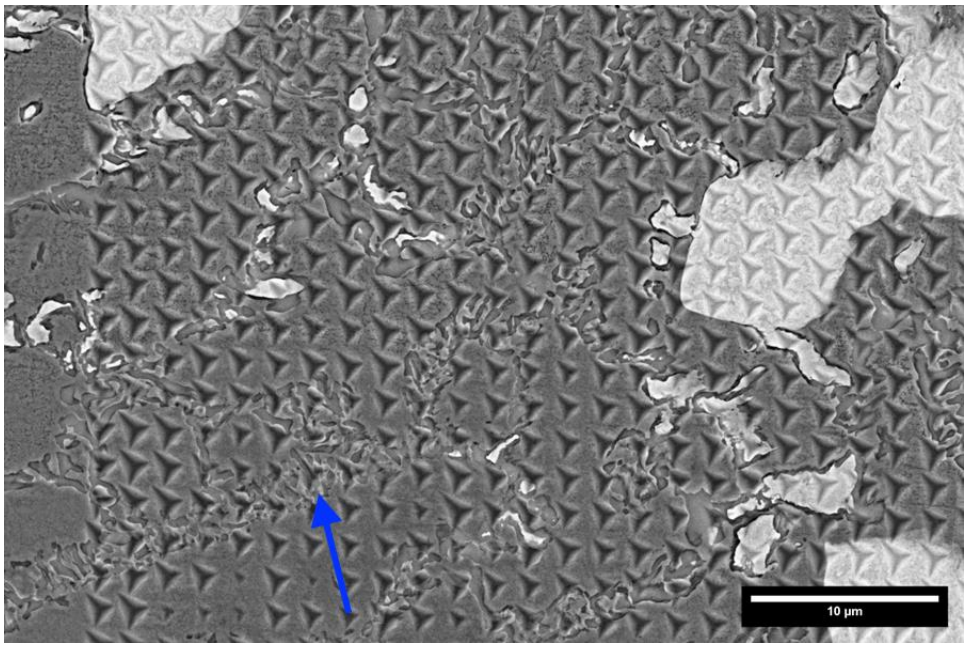

Figure 9-7 Higher magnification of BSE micrograph post Nanoblitz 3D indentation array.

The blue arrow in Figure 9-7 points to an indent encompassing both the μ phase and the FCC matrix. The indent overlaps occur because the μ structure is smaller than the actual individual indents and thus are too small for individual indents to only be influenced by the μ phase.

To better understand the μ phase, the other W-Mo-Fe-Ni samples were tested to provide more precise and accurate mechanical property values for each phase. First, the μ composition sample comprised of 10 at% W, 29 at% Mo, 34 at% Fe, and 27 at% Ni was tested. This sample had a larger μ phase but still had W dendrites and FCC matrix present (Figure 9-8).

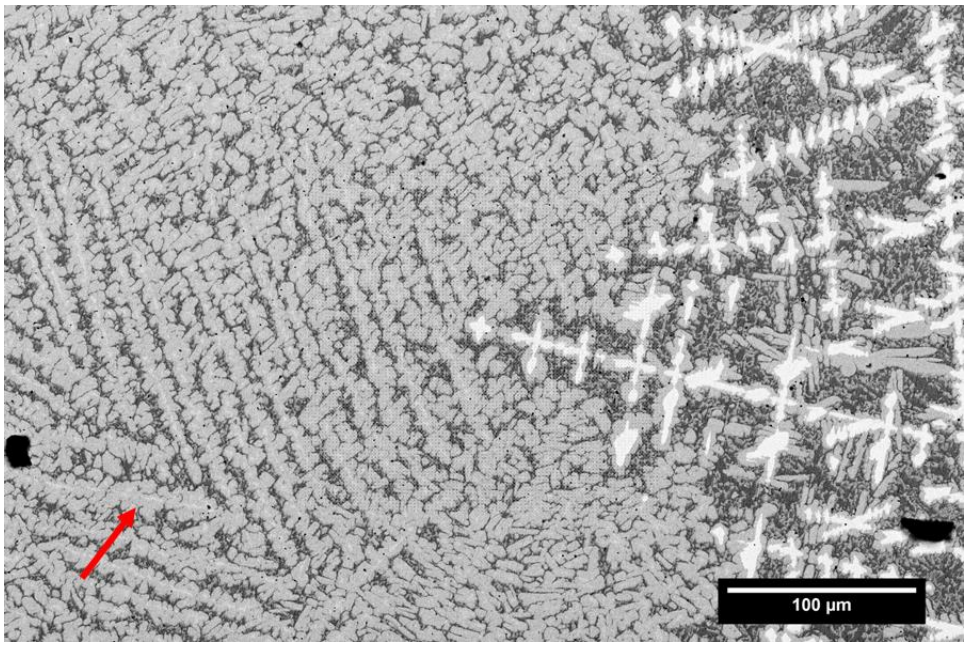

Figure 9-8 BSE micrograph of μ composition sample and the red arrow is pointed at the μ phase.

In Figure 9-8, the μ phase on the left-hand side of the micrograph can be seen as larger structures that encapsulate the W dendrites on the right-hand side of the micrograph. With a higher percentage of the μ phase present in the μ composition sample, the μ phase did not retain its lamellae structure as was observed in the equiatomic WMoFeNi sample. EDS and XRD were used to confirm that the μ phase present in both samples was similar in composition and crystal structure. The XRD results can be seen in Figure 9-1(b).

The same BCC and FCC peaks from Figure 9-1(a) (equiatomic sample) can be seen in Figure 9-1(b) (μ composition sample), indicating the presence of the BCC dendritic

phase and the FCC matrix. The XRD scan of the μ composition sample also showed the same peaks labeled as μ peaks with higher intensity. The μ composition sample was indented using Nanoblitz 3D to obtain the mechanical property heat maps (Figure 9-9) and average hardness and modulus of the three phases (Table 9-3).

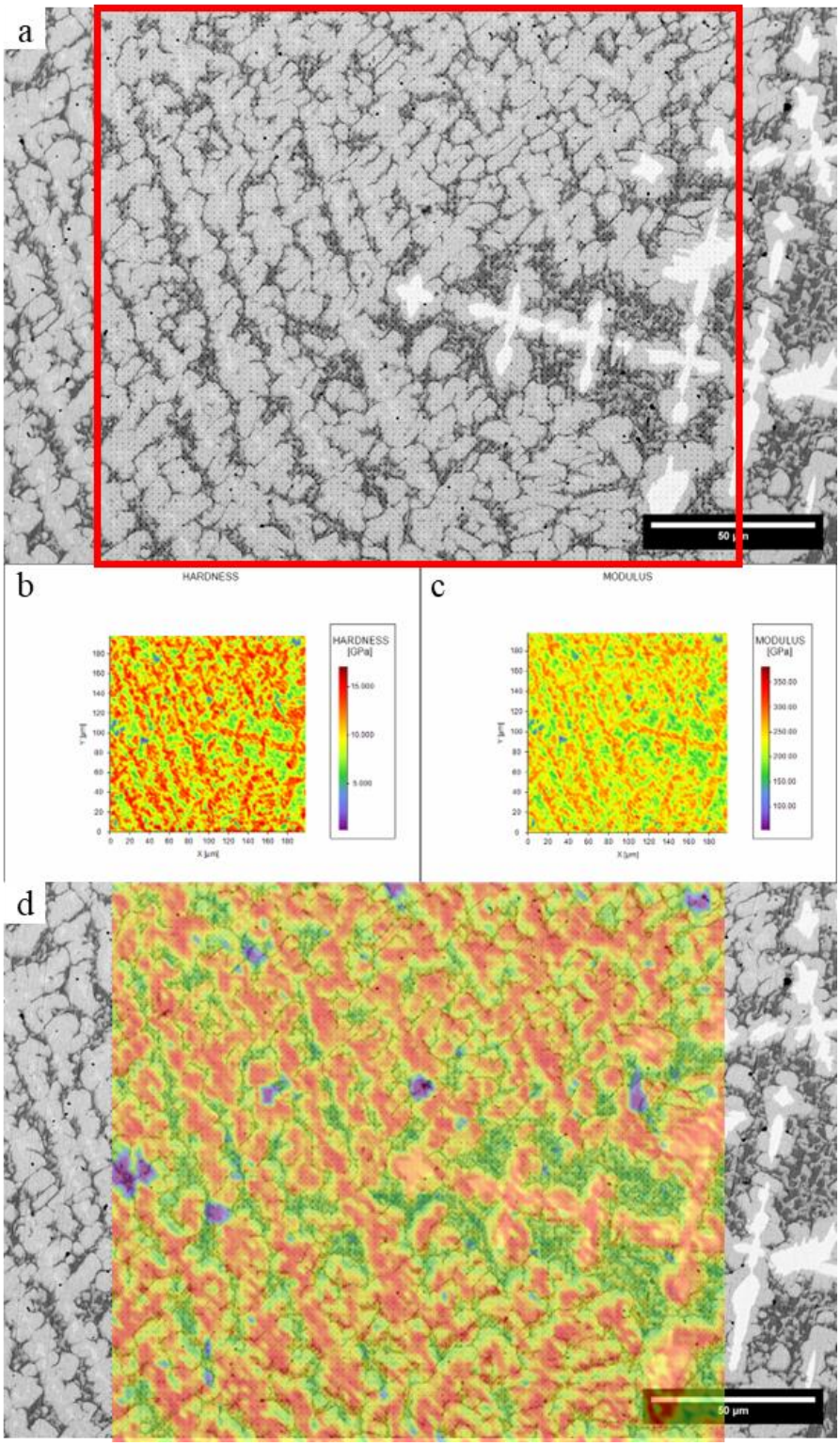

Figure 9-9 Composed of (a) BSE micrograph of μ composition sample after indentation where the indent array is within the red box, heat maps of (b) hardness and (c) modulus for a 100x100 indent array to 200 nm in depth, and (d) an overlay of the hardness map on the BSE micrograph.

It can be observed in Figure 9-9 that the μ phase has a similar hardness and modulus as the W dendrites as both phases are red, indicating a higher relative value. The matrix appears green, indicating a lower relative hardness and modulus than the W dendrites and μ phase.

Table 9-3 Average hardness and modulus of each phase seen in the μ composition phase.

Phase	Hardness (GPa)	Modulus (GPa)
W Dendrite	11.2 +/- 2.2	253 +/- 34
FCC Matrix	7.1 +/- 1.1	184 +/- 17
μ Phase	12.5 +/- 1.8	260 +/- 27

The average hardness for the W dendrites and the FCC matrix within the μ composition sample were very similar to the equiatomic WMoFeNi sample values (Table 9-2). For both the mu composition and the equiatomic WMoFeNi sample, the hardness of the FCC matrix and the W dendrites were within one standard deviation of each other. There were slight variances in the moduli as all the modulus values were higher in the μ composition sample than in the equiatomic WMoFeNi sample. These higher modulus values were most likely due to the size of the elastic deformation zone compared to the smaller plastic deformation zone. With the elastic zone being larger and encompassing a larger volume of the sample below the indenter at deeper depths, there is a higher probability that the elastic zone was influenced by the phases that surround it. This can cause a higher chance for the surrounding phases to influence the modulus which may not influence the hardness values. The higher FCC matrix modulus value might be due to more matrix indents being adjacent to harder phases in the μ composition sample. In the equiatomic sample, there were more

matrix indents surrounded by adjacent matrix indents, thus lowering the chance of the indents being influenced by the other phases present. The higher modulus of the W dendrites could be due to the μ phase surrounding the W dendrites, thus creating a mu shell on the dendrites. Note that the μ composition sample has less of the soft FCC matrix present than the equiatomic sample, which would cause an increase in the modulus. The percentages of each phase can be found in Appendix 5.

The FCC composition sample comprised of 5 at% W, 15 at% Mo, 40 at% Fe, and 40 at% Ni was also tested. As confirmed by XRD (Figure 9-1(c)), this sample only had the FCC matrix and the μ phase present. The small atomic percentage of W did not allow for W dendrites to form. The FCC composition sample was indented using Nanoblitz 3D (Figure 9-11).

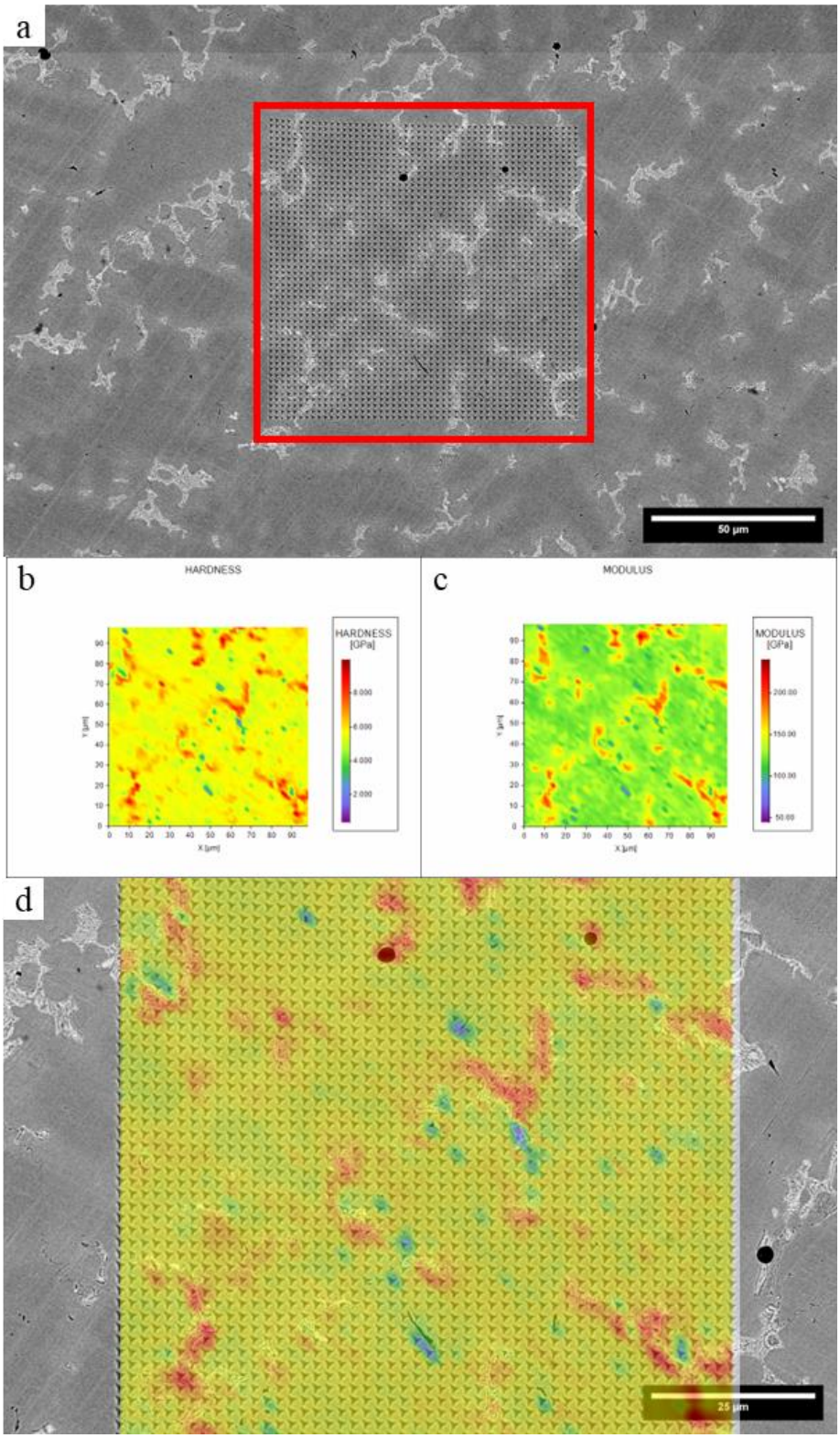

Figure 9-10 Composed of (a) BSE micrograph of FCC composition sample after indentation where the indent array is within the red box, heat maps of (b) hardness and (c) modulus for a 50x50 indent array to 200 nm in depth, and (d) an overlay of the hardness map on the BSE micrograph.

The FCC composition sample was comprised of the FCC matrix and the μ phase. The average hardness and modulus of these phases are shown in Table 9-4. Note that in the FCC composition sample, there is slight color modulation within the FCC matrix. This color modulation is seen within the property heat maps. In the hardness heat map, the FCC matrix varies from yellow to light orange. The variation in the hardness heat map correlates with the variation within the FCC matrix.

Table 9-4 Average hardness and modulus of each phase seen in the FCC composition phase.

Phase	**Hardness (GPa)**	**Modulus (GPa)**
FCC Matrix	5.6 +/- 0.3	132 +/- 7
μ Phase + FCC Matrix	6.6 +/- 1.1	161 +/- 22

Although the hardness and modulus of the FCC composition phase sample's FCC matrix and the μ phase + FCC matrix values are similar to those of the equiatomic sample seen in Table 9-2, there is a smaller standard deviation of the FCC matrix in the FCC composition sample. This is most likely due to the abundance of FCC matrix indents that are surrounded by other FCC matrix indents than the harder μ phase.

An overall look at the average hardness and modulus of each sample can be seen in Table 9-5.

Table 9-5 Overall summary of average hardness and modulus of equiatomic, μ composition, and FCC composition sample.

Phase	Hardness (GPa)			Modulus (GPa)		
	Equiatomic Sample	**μ Composition Sample**	**FCC Composition Sample**	**Equiatomic Sample**	**μ Composition Sample**	**FCC Composition Sample**
W Dendrites	12.5 +/- 1.9	11.2 +/- 2.2		240 +/- 35	253 +/- 34	
FCC Matrix	5.9 +/- 1.1	7.1 +/- 1.1	5.6 +/- 0.3	154 +/- 17	184 +/- 17	132 +/- 7
μ Phase + FCC Matrix	6.8 +/- 1.2		6.6 +/- 1.1	176 +/- 22		161 +/- 22
μ phase		12.5 +/- 1.8			260 +/- 27	

9.1.2 Nanoblitz 4D

Nanoblitz 4D was used to understand the relationship between hardness and modulus within the equiatomic WMoFeNi sample as indentation was performed to deeper depths. Indents were probed to a depth of 300 nm with a heat map generated every 50 nm (Figure 9-12).

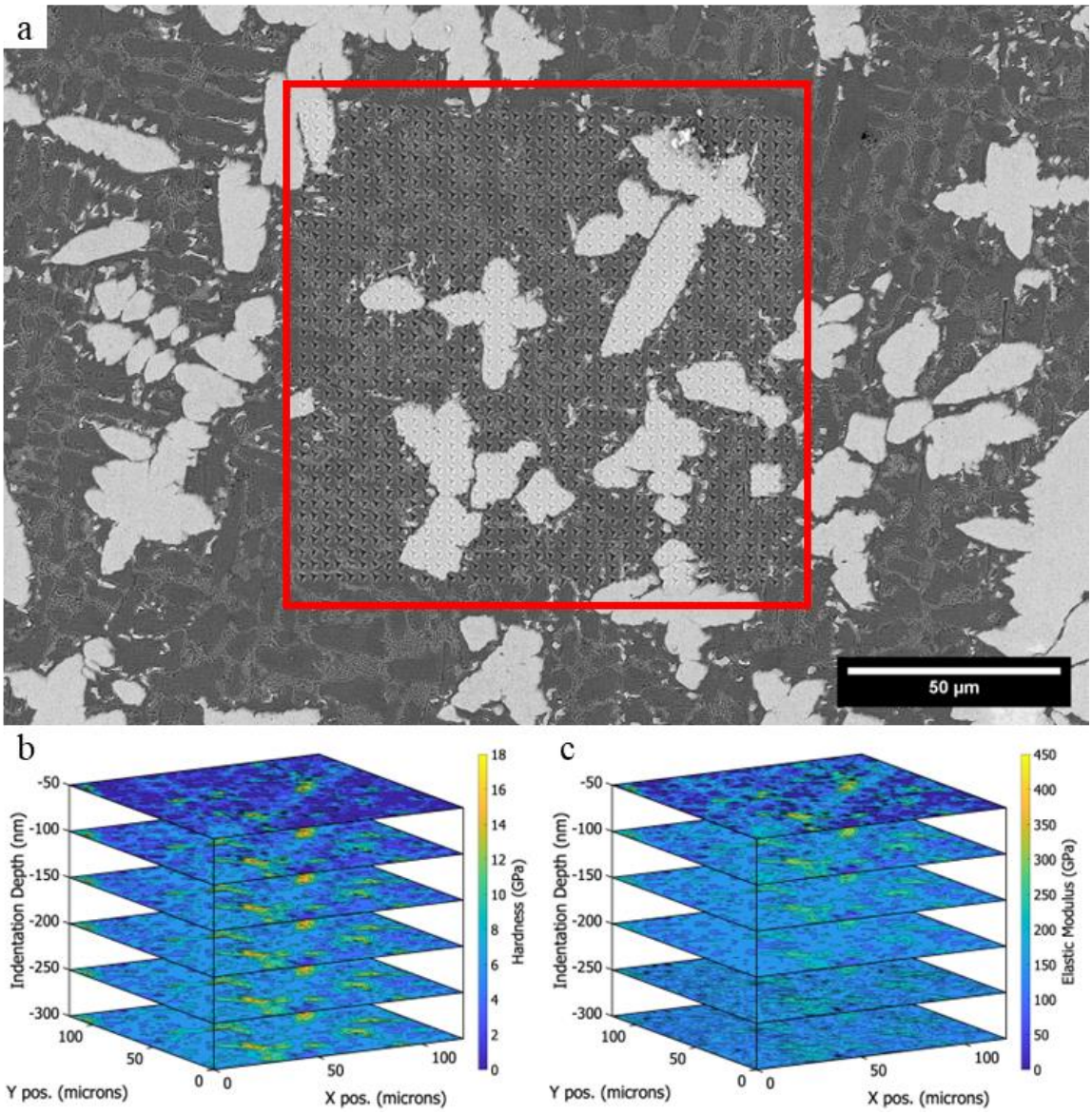

Figure 9-11 Composed of (a) BSE micrograph of the equiatomic WMoFeNi sample after indentation where the indent array is within the red box and heat maps of (b) hardness and (c) modulus for a 40x40 indent array to 300 nm in depth layers at every 50 nm.

While the individual heat maps were similar to those shown in Figure 9-6, slight differences are noted as the indents probed deeper into the sample. The heat maps are composed of more blue regions (or lower relative values) as the indent depth increases. As it is difficult to visualize these differences, a histogram of the data is presented in Figure 9-12.

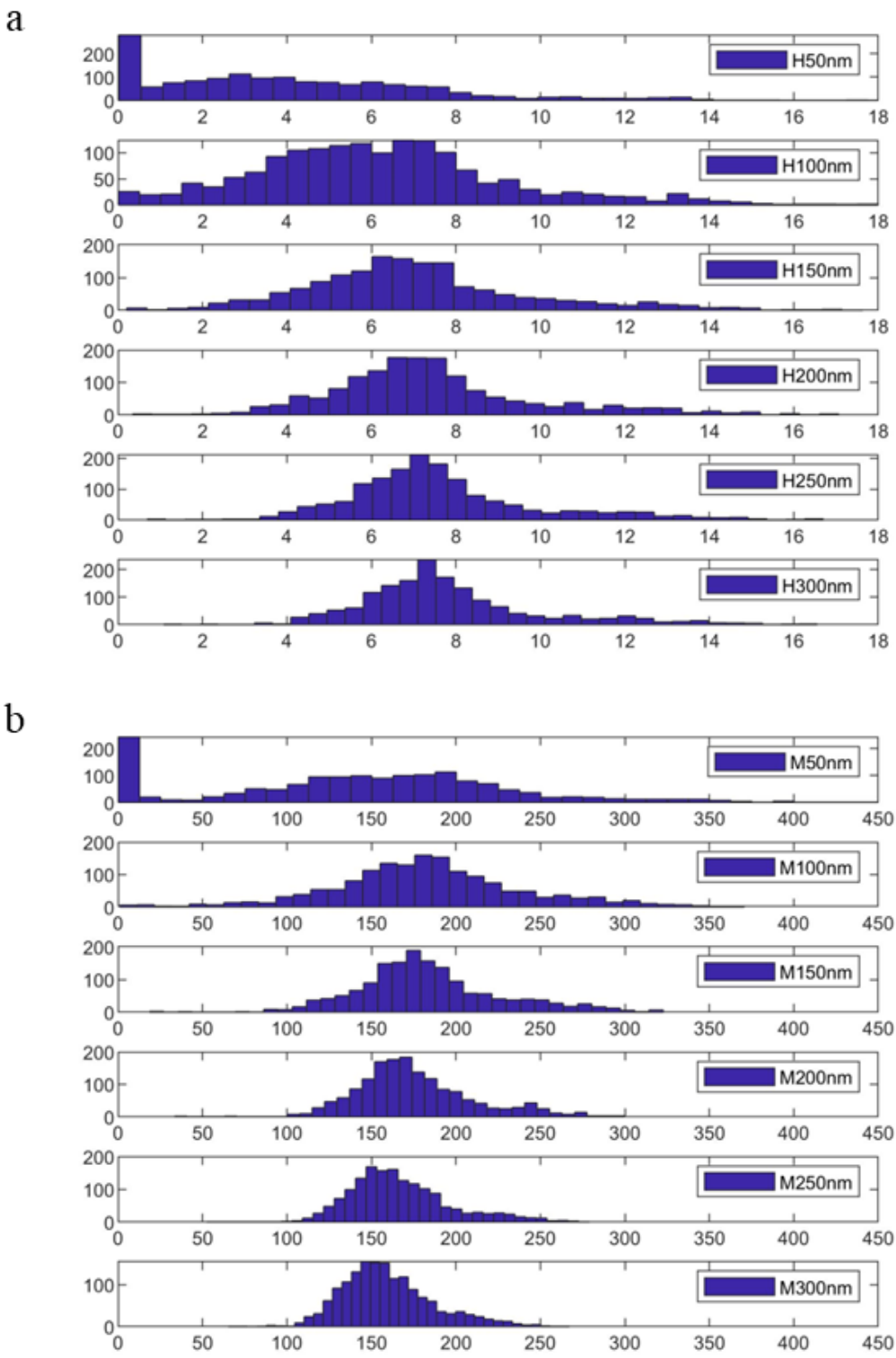

Figure 9-12 Nanoblitz 4D data from indents to 300 nm on the equiatomic WMoFeNi represented in a histogram plot for all 1,600 indents at each layer for the (a) hardness and (b) modulus.

At depths under 150 nm, the histogram plot shows a wider range of hardness and modulus data points as each phase is indented independently of surrounding phases. As the indent depth increases, the hardness and modulus begin to converge to an average value. The hardness converges around 7 GPa and the modulus converges at around 150 GPa. These values are similar to those found in Table 9-2.

Table 9-2 for the FCC matrix, which shows a hardness of 5.9 GPa and a modulus of 154 GPa for the equiatomic WMoFeNi sample. The similarity in these results indicates that as the indent depth increases, the mechanical behavior reflects more of a composite response than the separate mechanical behavior of the individual phases. Specifically, it appears that the values are converging to the FCC matrix properties since this phase makes up 75% of the equiatomic WMoFeNi sample.

While some of the decrease in modulus as the depth increases is due to the composite response, there is also a potential for an artificial decrease. This decrease in the modulus stems from an issue with the Nanoblitz 4D method when applied to metallic samples. The Nanoblitz 4D method assumes how the tip oscillates as it gathers data at each layer. It is assumed that the superimposed oscillation is entirely elastic, which is not the case for most metals. For metallic systems, both elastic and plastic deformation occurs when the tip is oscillated. The addition of plastic deformation leads to the Nanoblitz 4D method deriving an erroneous derived stiffness. To compensate for this issue, when the Nanoblitz 4D method was employed, a strain rate of 1/sec was used rather than the typical strain rate of 2/sec. The lower strain rate helped mitigate the amount of plastic deformation during oscillation. Note, however, that the use of a strain rate of 1/sec does not remove all

the plastic deformation caused by the tip oscillation. KLA is currently working to rectify this issue.

9.2 Future Work: Mechanical Behavior of Bulk W-Mo-Fe-Ni Alloy Samples

With a greater understanding of the mechanical properties of the W dendrites, FCC matrix, and the μ phase, it is essential to understand how these phases interact when analyzed as a bulk material. W-Mo-Fe-Ni alloy samples were cut to 6x6x9 mm samples for compression testing in the Gleeble. The first set of experiments tested the equiatomic WMoFeNi samples at various strain rates to determine if strain rate influenced the mechanical response (Figure 9-13).

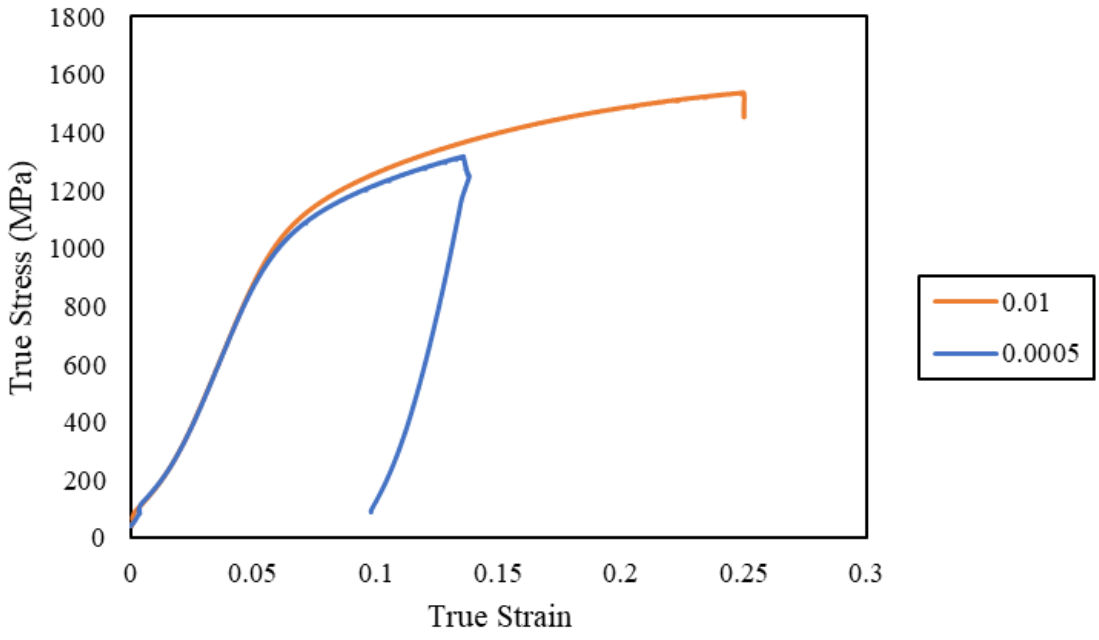

Figure 9-13 Stress-strain curve for compression testing of the equiatomic WMoFeNi samples at 0.0005/sec and 0.01/sec.

Figure 9-13 shows minimal changes in the mechanical response at the higher strain rate. Both the yield points and the work hardening-curves were similar. The yield point for

the equiatomic WMoFeNi sample was approximately 850 MPa for both stress-strain curves. Further studies at higher strain rates need to be completed to fully understand the strain rates that would impact the equiatomic WMoFeNi's mechanical behavior.

The compression tests run in the Gleeble were not done to failure, rather, the samples were loaded to a specific strain, held for 20 seconds, and then unloaded. The WMoFeNi samples were compressed at a quasi-static strain rate of 0.0005/sec and 0.01/sec. Future work would ramp up the testing to include higher strain rates and higher total strains to induce failure of the compression samples.

As it is hypothesized that WMoFeNi's self-sharpening behavior occurs in the FCC matrix phase and is pinned by the harder μ phase, Gleeble tests were run using samples composed of the FCC matrix composition. The microstructure of the FCC composition sample is less complex than the equiatomic WMoFeNi sample as it does not have the W dendrites present. The FCC composition sample only had two phases present, the FCC matrix and the μ phase lamellae structure. These samples were also cut to 6x6x9 mm samples for compression testing at a quasi-static rate of 0.0005/sec.

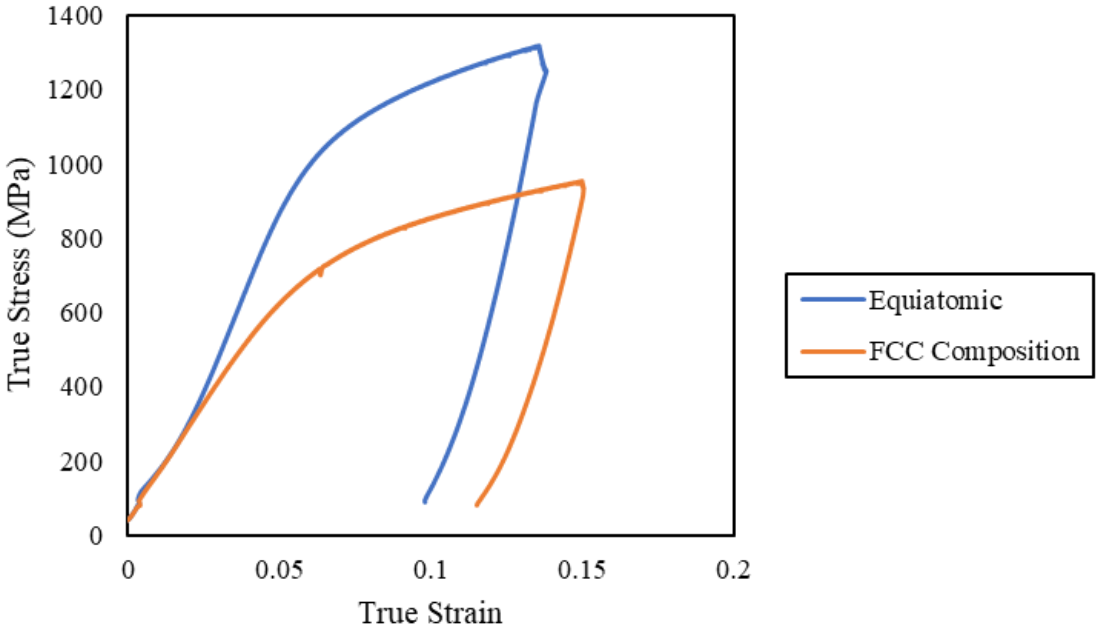

Figure 9-14 Stress-strain curves for quasi-static (0.005/sec) compression testing of the equiatomic WMoFeNi sample and the FCC composition sample.

As seen in Figure 9-14, the yield strength of the equiatomic WMoFeNi sample was higher than the FCC composition sample. The yield strength of the equiatomic WMoFeNi sample was approximately 850 MPa versus approximately 550 MPa for the FCC composition sample. The lower yield strength may be due to the higher percentage of FCC matrix in the FCC composition sample and/or the lack of W dendrites. The FCC matrix comprised of 89% of the FCC composition sample and 75% of the WMoFeNi sample.

Similar to the tests presented in Figure 9-13, the samples were not compressed until failure, rather, they were compressed to a specific strain, held for 20 seconds, and then unloaded. There was a slight dip in the FCC composition sample stress-strain curve above 5% strain due to a 20-second hold before loading to 15% strain.

The slope of the initial loading curve is lower than expected for each compression curve. Stubbers and Starr are currently working on this issue aims to rectify this apparent

error and obtain accurate elastic moduli from the stress-strain curves. When loading samples into the Gleeble, paste and foil are used for lubrication between the sample and anvils. When compressing only the paste and foil, approximately 1 mm is compressed. This compression accounts for a significant percentage of the total compressed area when the 9 mm samples were compressed to strains below 30% (or 2.7 mm). The yield point and work hardening curves were not impacted by the compression of the foil and paste as it only impacted the elastic region of the curve. It should be noted that steel samples, which have well documented steel curves, were tested to confirm the understanding of the issues seen in the stress-strain curves. It was found that the elastic loading curve had a slope lower than expected however the yield point and plastic region of the curve was unaffected.

While this section begins to explore the bulk mechanical behavior of the W-Mo-Fe-Ni alloy samples, there is still work to be done in this area. For example, tests need to be repeated once the compliance issue noted above has been resolved to ensure more accurate modulus values. More experiments should also be conducted at higher strain rates and total strain for both the equiatomic WMoFeNi and FCC composition samples.

9.3 Conclusions

Through the exploration of the mechanical properties of W-Mo-Fe-Ni's three distinct phases (W dendrites, FCC matrix, and μ lamellae) it was concluded that the μ phase and the W dendrites have higher hardness and modulus values as compared to the soft FCC matrix. The μ phase and W dendrites are almost twice as hard as the FCC matrix and, thus supports the theory that deformation occurs in the matrix and is pinned by the harder μ phase. Note that the differing samples allowed for the most accurate hardness and modulus

values for various reasons. The recommended sample type to test for accurate and precise hardness and modulus values is summarized in Table 9-6.

Table 9-6 Recommended sample for retrieving appropriate hardness and modulus readings for various phases found in WMoFeNi samples.

Phase	Hardness (GPa)	Modulus (GPa)	From Sample	Reasoning
W Dendrite	12.5	240	Equiatomic Sample	Large W dendrites, no μ shell
FCC Matrix	5.6	132	FCC Composition Sample	Substantial matrix without hard phases nearby
μ Phase	12.5	260	μ Composition Sample	Large μ phase, no influence of matrix

When exploring the mechanical properties of the W dendrites, it is recommended to use the equiatomic WMoFeNi sample's hardness and modulus values. This is due to the large dendritic structures and the absence of the μ shell which was found in the μ composition sample. When exploring the mechanical properties of the FCC matrix, it is recommended to use the FCC composition sample. This is because the FCC matrix within the FCC composition sample has large areas of matrix that are not near the harder dendritic and lamellae structures. These larger FCC matrix areas lead to hardness and modulus values with the smallest standard deviation resulting in a more precise measurement of the FCC matrix. The final recommendation is to use the μ composition sample's hardness and modulus of the μ phase. This recommendation is because the μ composition sample has μ phase present which is large enough to be indented without a composite response of indenting multiple phases under one indent. The μ phase present in the equiatomic WMoFeNi and FCC composition sample was a lamellae structure with a nanometer length scale which is smaller than the indents created.

The beginning exploration of Nanoblitz 4D was performed on the equiatomic WMoFeNi sample. This allowed for high-speed mechanical property mapping as indents reached deeper depths. At shallow depths, the mechanical property heat maps showed a larger distribution of hardness and modulus readings than at deeper depths. This is most likely due to indents encompassing a larger area as it indents to deeper depths. As this area increases, the plastic and elastic deformation zones also increase. As more area below the indent tip is used to calculate the hardness and modulus, a composite reading of multiple phases may occur.

After the exploration of individual phases within W-Mo-Fe-Ni samples, bulk compression tests were completed on the equiatomic WMoFeNi and FCC composition samples. First, the equiatomic WMoFeNi sample was tested at two low-strain rates. These compression tests did not show a mechanical dependence on strain rate. Next, the equiatomic WMoFeNi and FCC composition samples were tested at a quasi-static strain rate. These compression tests showed differences in the stress-strain curves. This is most likely due to the FCC composition sample not having any W dendrites which causes a lower yield point.

Future Nanoblitz 4D experiments should be performed on the other W-Mo-Fe-Ni alloys to see if similar composite responses occur at deeper depths. Nanoblitz 4D could aid in determining which depth would allow for the best resolution when utilizing Nanoblitz 3D. The current Nanoblitz 3D tests explored depths at 50 nm which provided high resolution but a depth at 200 nm was necessary to calculate the average hardness and modulus of individual phases. Nanoblitz 4D could be employed to create additional slices between the 50 nm and 200 nm depth range to help determine which indentation depth

provides both high resolution and indents large enough to calculate average mechanical properties.

Bulk testing is in its infancy and more compression tests need to be run. Compression tests of both the equiatomic WMoFeNi and FCC composition samples should be run at high strain rates. Tests should also be completed to failure to determine if any ABS occurs when compressed to failure. Once the foil and paste issues are resolved, the modulii of samples should be compared.

CHAPTER 10. CONCLUSIONS AND FUTURE WORK

10.1 Nanoporous Gold

As np-Au has many applications at elevated temperatures, it is essential to quantify the effect operating temperatures have on its porous structure. Np-Au had a high thermal stability when heated below 400 °C in a low vacuum. Little to no changes in the ligament structure were seen over a 60-minute heating period. However, ligament coarsening in a low vacuum was achieved at temperatures above 400 °C. It is important to note that if np-Au is used in low vacuum conditions above 400 °C, its structure will change. These structural changes will affect the surface area-to-volume ratio as well as the mechanical behavior of np-Au.

In-situ experiments of annealing np-Au allowed for a more detailed analysis of how the nanoporous microstructure changed throughout the heating process. Micrographs were captured at scheduled intervals and stitched together to form a clearer picture of how the ligaments and pores expanded.

While the ability to conduct coarsening experiments *in-situ* has its advantages versus *ex-situ* experiments, it was noted that when conducting *in-situ* experiments in an SEM, the electron beam affected the sample's ligament coarsening. At temperatures above 500 °C, the electron beam enhanced surface diffusion and increased the growth rate of np-Au's ligament diameter. It was noted that the initial rate of growth was higher than the final rate of growth due to the influence of the electron beam.

When using the high-speed mapping nanoindentation technique on np-Au to determine changes in its mechanical properties, it was found that the optimal ratio of indent spacing to indent depth is 10. This ratio minimizes any influence of plastic strain from prior indents

and utilizes the smallest required area for testing. The optimal *d/h* ratio found for np-Au was also the same optimal *d/h* ratio for fully dense material found in previous research. Note that the optimal *d/h* ratio of 10 was found regardless of the np-Au sample's ligament length, film thickness, or relative density. The optimal *d/h* ratio was also confirmed at various indent depths.

It is suggested that future work in this area include *in-situ* heating experiments for longer durations given the change in np-Au's growth rate after heating for 30 minutes. This work should also include *in-situ* heating experiments at higher temperatures as coarsening was only seen in the three highest heating conditions. Further analysis also needs to determine the exact impact the electron beam had on coarsening.

Finally, it is suggested that future work on other nanoporous materials be performed to ensure that the optimal *d/h* ratio found for np-Au is a universal ratio for all nanoporous materials.

10.2 Multi-Principal Element Alloys

Equiatomic WMoFeNi has three phases: FCC matrix, BCC W dendrites, and μ phase. The mechanical properties of each phase were explored to determine how they would affect the bulk properties of the alloy. It was found that the W dendrites and the μ phase were the hardest and stiffest phases. The softest and least stiff phase was the FCC matrix with a hardness and modulus that was only half of that found for the W dendrites and μ phase. These findings support the theory that ASB deformation occurs in the matrix and is pinned by the harder μ phase.

The compression tests of bulk WMoFeNi samples showed little to no mechanical behavior strain rate dependence at low strain rates (*i.e.*, 0.0005/sec and 0.01/sec). There

were, however, differences between quasi-static testing of the bulk equiatomic WMoFeNi and the FCC composition samples. The FCC composition sample had a lower yield point than the equiatomic WMoFeNi sample. However, further work must be conducted at higher strain rates for both samples as well as compression tests to failure.

APPENDICES

APPENDIX A

Gibson and Ashby derived multiple equations for a two-dimensional structure. The full table can be seen in Table A-1.

Table A-1 Two -Dimensional properties (reproduced from [34]).

		General 2D Hexagonal Cellular Structure	Regular Hexagonal Structure (θ=30°, h/l=1)
Linear Elastic Properties	E_1	$E_s \frac{t^3}{l^3} \frac{cos\theta}{\left(\frac{h}{l} + sin\theta\right) sin^2\theta}$	$\frac{4}{\sqrt{3}} E_s \frac{t^3}{l^3}$
	E_2	$E_s \frac{t^3}{l^3} \frac{(\frac{h}{l} + sin\theta)}{cos^3\theta}$	$\frac{4}{\sqrt{3}} E_s \frac{t^3}{l^3}$
	ν_1	$\frac{cos^2\theta}{\left(\frac{h}{l} + sinc\theta\right) sin\theta}$	1
	ν_2	$\frac{(\frac{h}{l} + sin\theta) sin\theta}{cos^2\theta}$	1
	G	$E_s \frac{t^3}{l^3} \frac{(\frac{h}{l} + sin\theta)}{(\frac{h}{l})^2 \left(\frac{2h}{l} + 1\right) cos\theta}$	$\frac{1}{\sqrt{3}} E_s \frac{t^3}{l^3}$
Elastic Buckling	σ_{el}^*	$E_s \frac{t^3}{l^3} \frac{(\beta^*)^2}{6(\frac{h}{l})^2 cos\theta}$	$0.22 E_s \frac{t^3}{l^3}$
Plastic Collapse	$(\sigma_1^*)_{pl}$	$\sigma_y \frac{t^2}{l^2} \frac{1}{2\left(\frac{h}{l} + sin\theta\right) sin\theta}$	$\frac{2}{3} \frac{t^2}{l^2} \sigma_y$
	$(\sigma 2^*)_{pl}$	$\sigma_y \frac{t^2}{l^2} \frac{1}{2cos^2\theta}$	$\frac{2}{3} \frac{t^2}{l^2} \sigma_y$

APPENDIX B

The tip area is based on a calibration using indents into a known sample. The known sample for this work was fused silica. 25 indents were performed then a curve fit was completed by KLA software to find the C terms for Equation B-1.

$$A(h_c) = C_0 h_c^2 + C_1 h_c^1 + C_2 h_c^{1/2} + C_3 h_c^{1/4} + \cdots C_8 h_c^{1/128} \quad \text{Equation B-1}$$

Where $A(h_c)$ is the tip contact area and C are area constants. Note for a perfect Berkovich tip, C_0 would be 24.5 however each tip has its own flaws so C_0 is calculated in the curve fit. Table B-1 is an example of a tip calibration for our Berkovich tip using five constants as recommended by KLA.

Table B-1 First five constant terms for a Berkovich tip area calibration.

Constant	**Constant Value**
C0	21.518
C1	3,662.431
C2	-16,028.082
C3	103,898.878
C4	-88,840.493

Table B-2 is the tip contact area for indent depths used in this work. The indent width was calculated based on the tip contact area assuming the Berkovich tip is a perfect equilateral triangle.

Table B-2 List of tip contact area for indent depths used in this work.

Indent Depth (nm)	**Tip Contact Area (μm^2)**	**Indent Width (μm)**
50	0.255	0.66
100	0.592	1.01
200	1.585	1.66
300	3.009	2.28
400	4.864	2.90
500	7.150	3.52

APPENDIX C

To identify which indents in a Nanoblitz 3D array corresponded with which phase present in the microstructure SEM micrographs were used post indentation. Knowing the number of indents in each array, indents were counted to find the corresponding residual indents and points on heat maps. The following is an example of this method.

A Nanoblitz 3D array was conducted on the WMoFeNi sample. The array was 50x50 indents with a 2 μm spacing between each indent resulting in an array that was 100x100 μm (Figure A2-1).

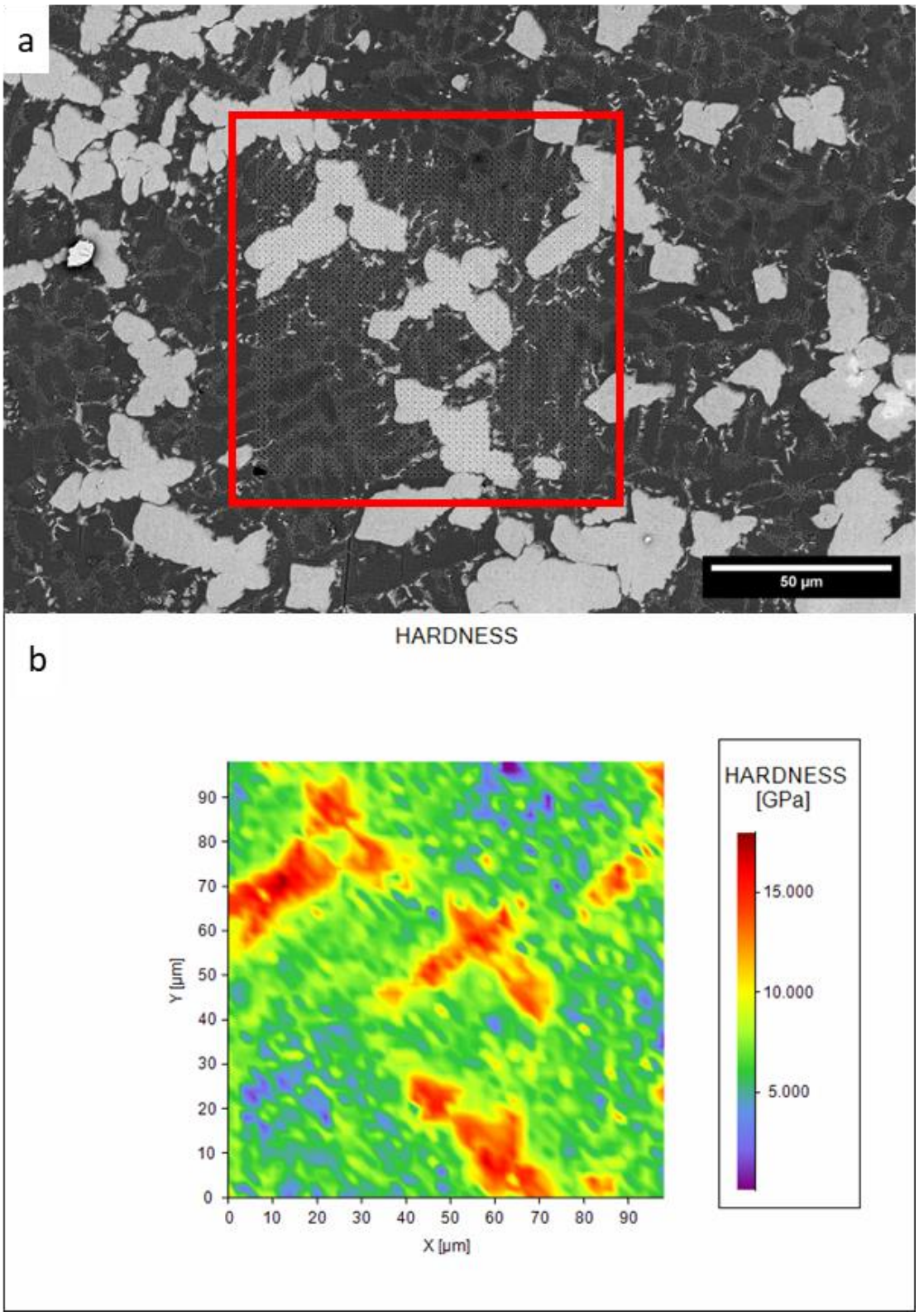

Figure C-1 (a) BSE micrograph of WMoFeNi where the red box indicates where the Nanoblitz 3D array was indented. The array is composed of 50x50 indents and (b) a hardness heat map from the resulting 50x50 indent array.

If the mechanical properties of a W dendrite were needed, an indent fully within the W dendrite was identified. Note that Figure C-2 shows the same region as Figure C-1 but at a higher magnification.

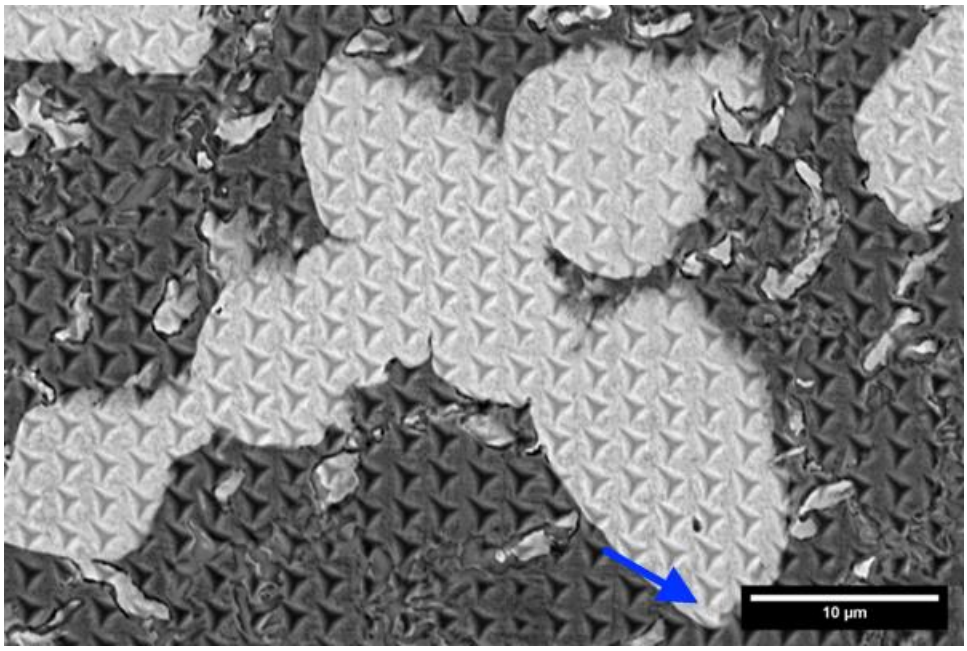

Figure C-2 BSE micrograph of WMoFeNi sample at increased magnification post Nanoblitz 3D. The blue arrow indicates an indent fully within the W dendrite.

The blue arrow points to the 35th indent from the left and the 20th indent from the bottom. Due to the 2 µm spacing that indent would be at 70 µm in the x direction and 40 µm in the y direction. This point could then be identified within the heat maps (Figure C-3).

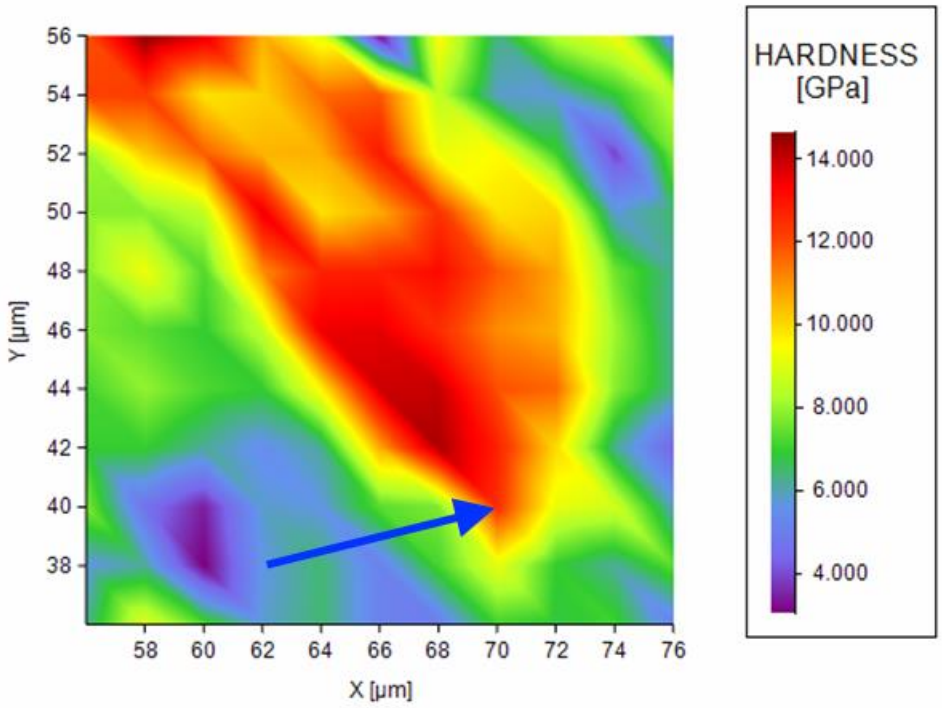

Figure C- 1 Hardness heat map magnified to identify the point at (70, 40) µm.

The data that formulates the heat maps was stored within a spreadsheet. This allows the user to determine the exact value that makes up each point. Once data points were connected to a phase in the micrograph the average hardness and modulus for each phase was calculated.

APPENDIX D

For easier readability, the figures presented in this work only included the hardness heat maps overlayed onto the corresponding micrograph. This appendix includes both the hardness and modulus overlays.

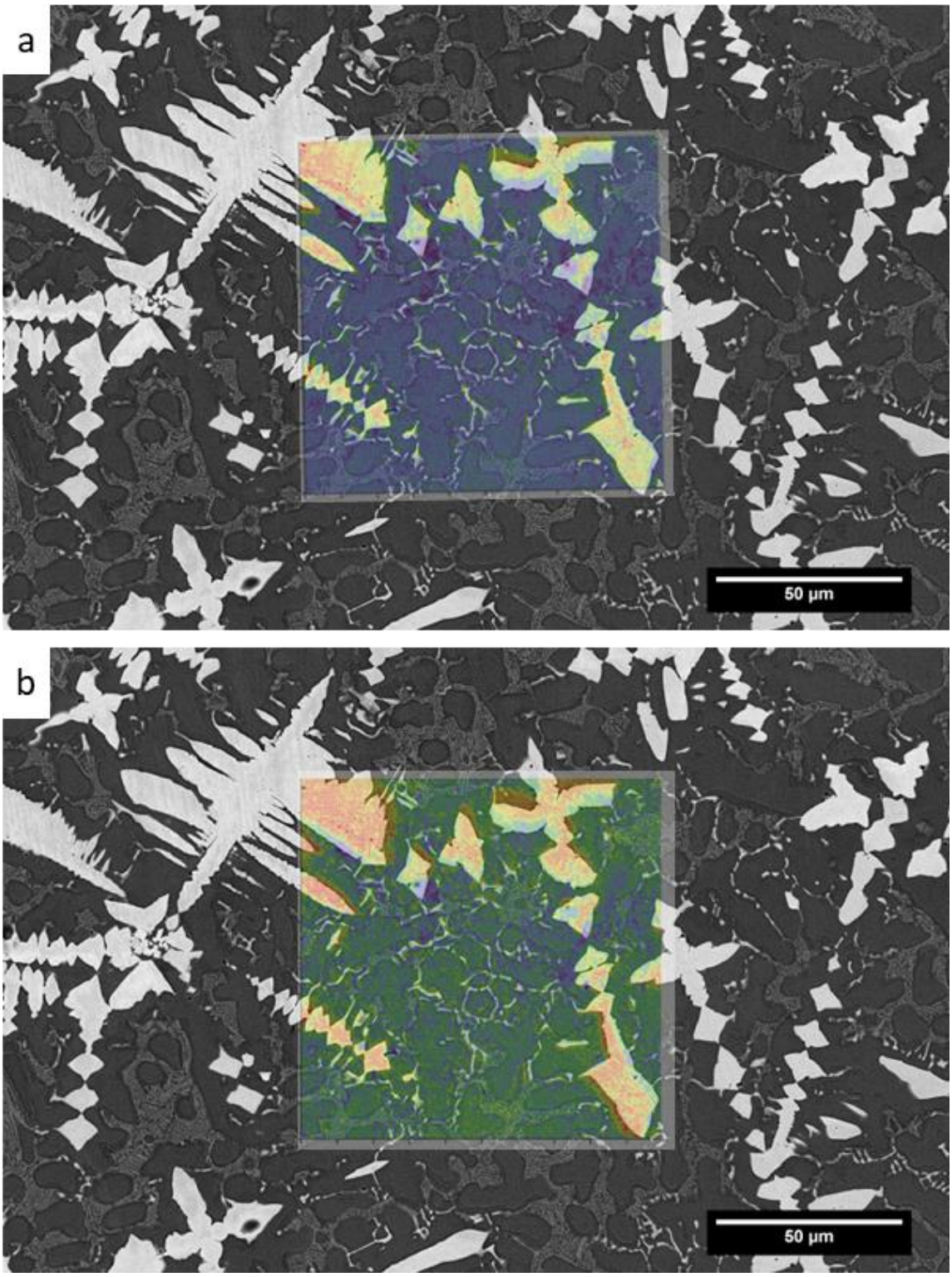

Figure D-1 BSE micrograph of WMoFeNi sample with the overlay of (a) hardness and (b) modulus heat map from a 200x200 indent array at 50 nm depth.

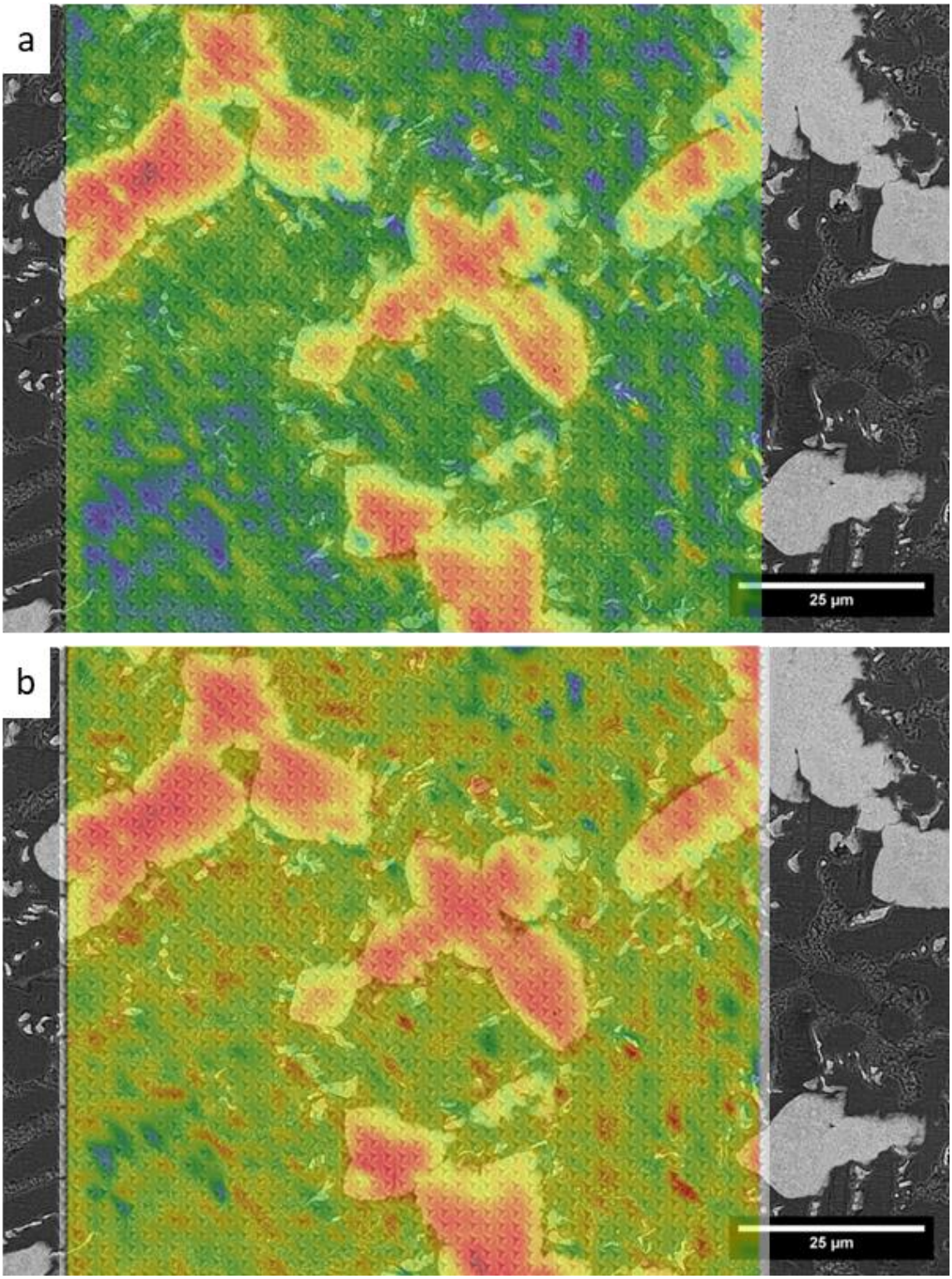

Figure D-2 BSE micrograph of WMoFeNi sample with the overlay of (a) hardness and (b) modulus heat map from a 50x50 indent array at 200 nm depth.

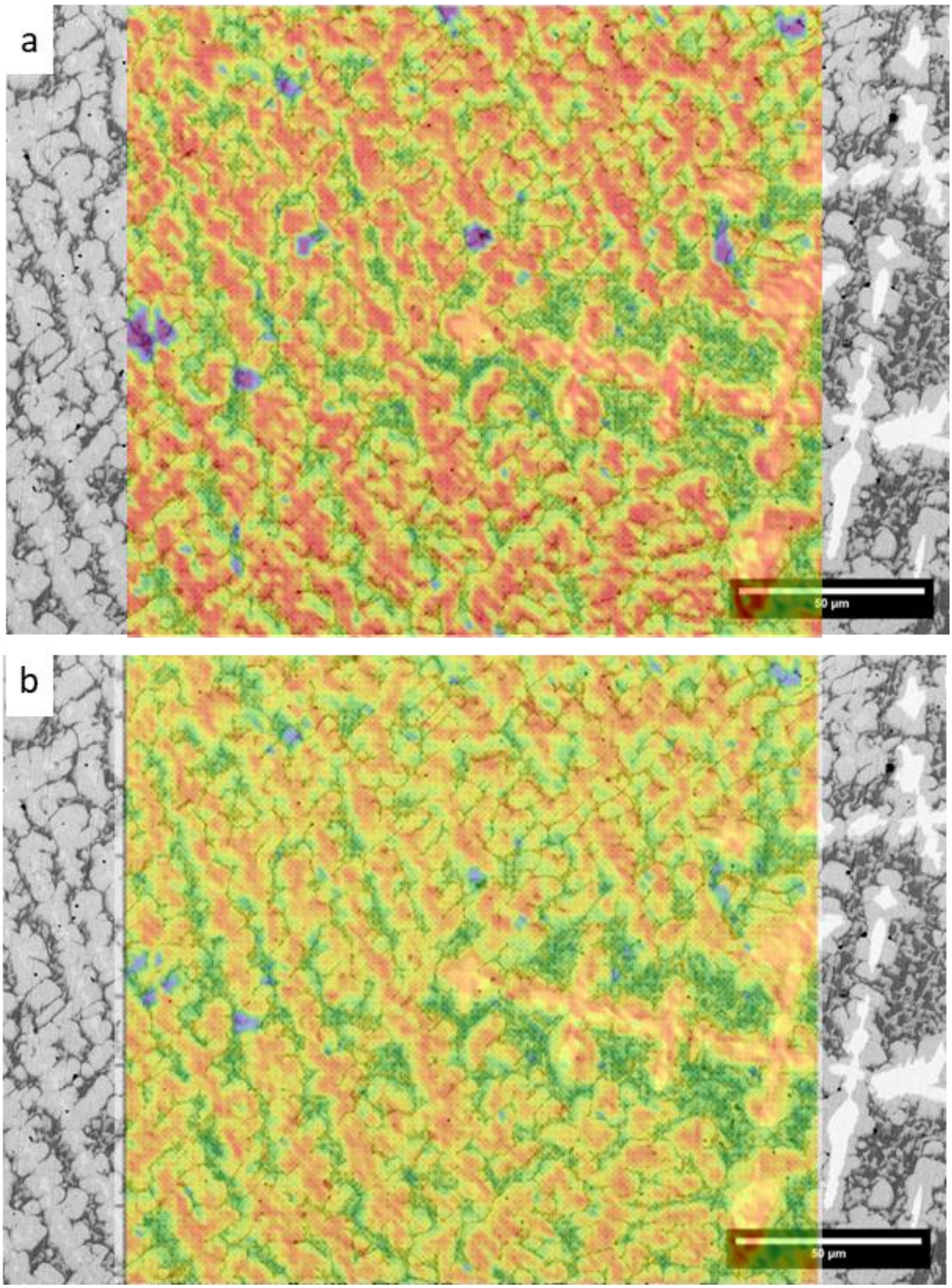

Figure D-3 BSE micrograph of µ composition sample with the overlay of (a) hardness and (b) modulus heat map from a 50x50 indent array at 200 nm depth.

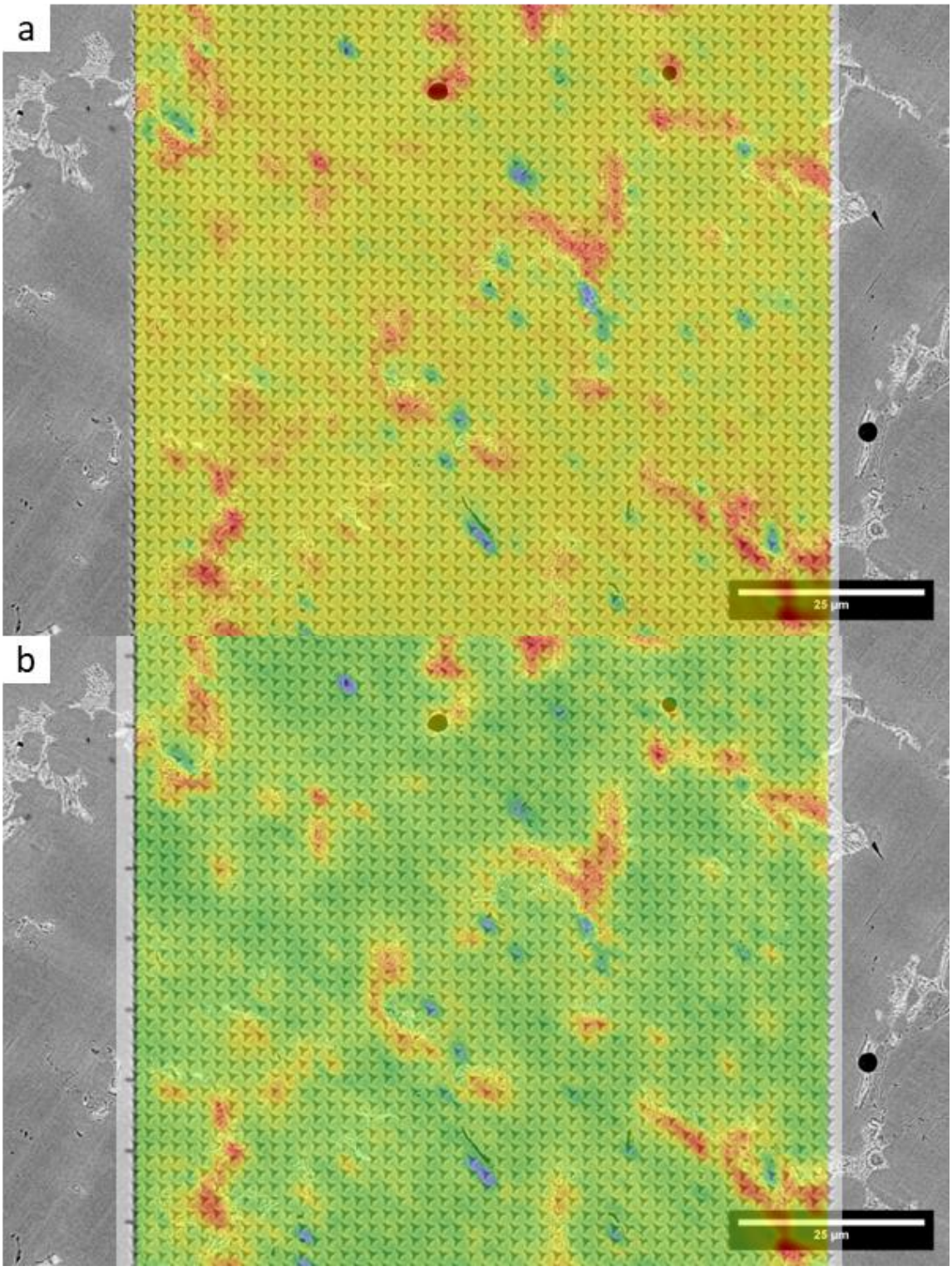

Figure D-4 BSE micrograph of FCC composition sample with the overlay of (a) hardness and (b) modulus heat map from a 50x50 indent array at 200 nm depth.

APPENDIX E

The phase percentages of different samples were determined by loading a micrograph of a sample in Image J, an imaging software program. Image J has a threshold tool that takes a grey-scale image and turns it into a black-and-white image. The threshold tool allows for only certain levels of grey scale to be converted into black and the rest of the image is turned white. Image J determines how much of the sample was black versus white. The following explains how to determine the percentage of each phase in a sample.

If the amount of W dendrites in a WMoFeNi sample is needed, a low magnification micrograph of the sample is used. Once that sample is in Image J the color threshold can be adjusted to only include the level of grey scale that indicates the W dendrites (Figure D-1).

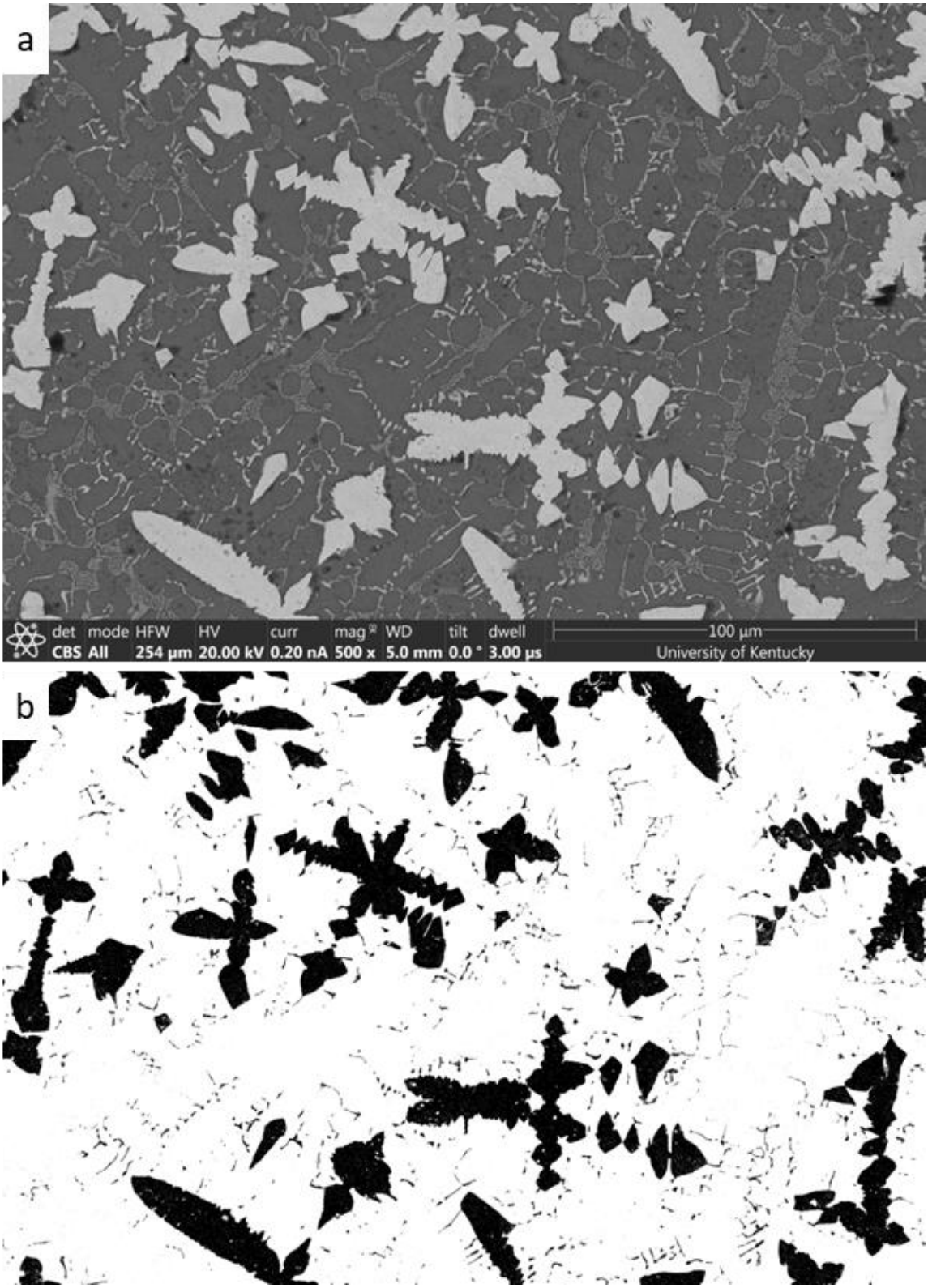

Figure E-1 (a) SE micrograph of WMoFeNi (b) threshold tool in Image J to show W dendrites in black and the rest in white.

The bright W dendrites are separated from the rest of the image and shown in black in Figure E-1(b). Image J can calculate the percentage of black from the image. This percentage was used for the percent of W dendrites in the sample. This process was used for each phase and each sample used throughout this work. The percentages are tabulated in Table E-1.

Table E-1 Percentage of each phase in different samples.

	Phase		
Sample	**W Dendrite**	**FCC Matrix**	**M Phase**
Equiatomic WMoFeNi	20%	75%	5%
FCC Composition	-	89%	11%
M composition-μ heavy region	5%	24%	71%
M composition-W heavy region	17%	33%	50%

Note the μ composition sample has two distinct regions. One region has more μ phase present (on the left-hand side), and one has large W dendrites (on the right-hand side). These regions are noted in Figure D-2.

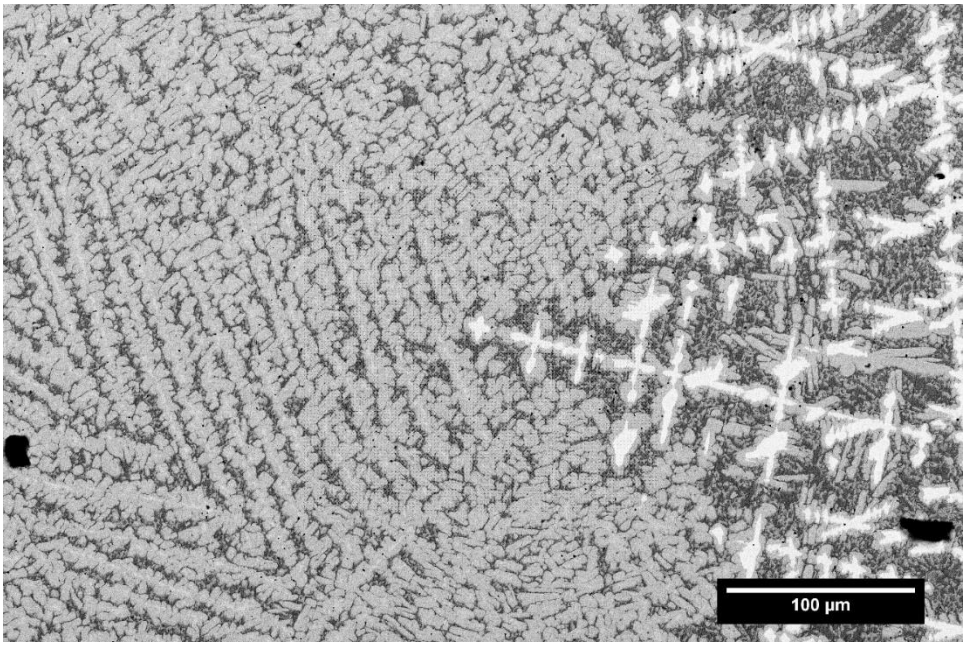

Figure E-2 BSE micrograph of the µ composition sample where the µ heavy region is located on the left-hand side and the W dendrite heavy region is located on the right-hand side.

BIBLIOGRAPHY

[1] J. D. Muhly, "Chrysokamino in the History of Early Metallurgy," *Hesperia Supplements,* vol. 36, pp. 155-177, 2006. [Online]. Available: http://www.jstor.org/stable/20066735.

[2] T. A. Wertime, "Man's First Encounters With Metallurgy: Man's discovery of ores and metals helped to shape his sense of science, technology, and history," *Science,* vol. 146, no. 3649, pp. 1257-1267, 1964.

[3] C. S. Smith, "The Interaction of Science and Practice in the History of Metallurgy," *Technology and Culture,* vol. 2, no. 4, pp. 357-367, 1961, doi: 10.2307/3100891.

[4] J. W. Yeh *et al.*, "Nanostructured High-Entropy Alloys with Multiple Principal Elements: Novel Alloy Design Concepts and Outcomes," *Advanced Engineering Materials,* vol. 6, no. 5, pp. 299-303, 2004, doi: 10.1002/adem.200300567.

[5] A. Wittstock, J. Biener, and M. Bäumer, "Nanoporous gold: a new material for catalytic and sensor applications," *Physical Chemistry Chemical Physics,* vol. 12, no. 40, p. 12919, 2010, doi: 10.1039/c0cp00757a.

[6] Y. Ding, Y. J. Kim, and J. Erlebacher, "Nanoporous Gold Leaf: ?Ancient Technology?/Advanced Material," *Advanced Materials,* vol. 16, no. 21, pp. 1897-1900, 2004, doi: 10.1002/adma.200400792.

[7] J. Erlebacher, M. J. Aziz, A. Karma, N. Dimitrov, and K. Sieradzki, "Evolution of nanoporosity in dealloying," *Nature,* vol. 410, no. 6827, pp. 450-453, 2001, doi: 10.1038/35068529.

[8] H. W. Pickering, "Characteristic features of alloy polarization curves," *Corrosion Science,* vol. 23, no. 10, pp. 1107-1120, 1983.

[9] H. Pickering and P. Swann, "Electron metallography of chemical attack upon some alloys susceptible to stress corrosion cracking," *Corrosion,* vol. 19, no. 11, pp. 373t-389t, 1963.

[10] P. Swann and H. Pickering, "Implications of the stress aging yield phenomenon with regard to stress corrosion cracking," *Corrosion,* vol. 19, no. 11, pp. 369t-372t, 1963.

[11] A. Forty, "Corrosion micromorphology of noble metal alloys and depletion gilding," *Nature,* vol. 282, pp. 597-598, 1979.

[12] A. Forty and P. Durkin, "A micromorphological study of the dissolution of silver-gold alloys in nitric acid," *Philosophical magazine A,* vol. 42, no. 3, pp. 295-318, 1980.

[13] D. B. Miracle and O. N. Senkov, "A critical review of high entropy alloys and related concepts," *Acta Materialia,* vol. 122, pp. 448-511, 2017, doi: 10.1016/j.actamat.2016.08.081.

[14] J.-W. Yeh, "Overview of High-Entropy Alloys," Springer International Publishing, 2016, pp. 1-19.

[15] M. C. Gao, C. S. Carney, Ö. N. Doğan, P. D. Jablonksi, J. A. Hawk, and D. E. Alman, "Design of Refractory High-Entropy Alloys," *JOM,* vol. 67, no. 11, pp. 2653-2669, 2015, doi: 10.1007/s11837-015-1617-z.

[16] A. Mohammed and A. Abdullah, "Scanning electron microscopy (SEM): A review," in *Proceedings of the 2018 International Conference on Hydraulics and Pneumatics—HERVEX, Băile Govora, Romania*, 2018, vol. 2018, pp. 7-9.

[17] W. Zhou, R. Apkarian, Z. L. Wang, and D. Joy, "Fundamentals of scanning electron microscopy (SEM)," *Scanning Microscopy for Nanotechnology: Techniques and Applications,* pp. 1-40, 2007.

[18] J. I. Goldstein, D. E. Newbury, J. R. Michael, N. W. Ritchie, J. H. J. Scott, and D. C. Joy, *Scanning electron microscopy and X-ray microanalysis*. Springer, 2017.

[19] R. E. Smallman and A. Ngan, *Physical metallurgy and advanced materials*. Elsevier, 2011.

[20] Y. Leng, *Materials characterization: introduction to microscopic and spectroscopic methods*. John Wiley & Sons, 2009.

[21] D. R. Askeland, P. P. Phulé, W. J. Wright, and D. Bhattacharya, "The science and engineering of materials," 2003.

[22] W. C. Oliver and G. M. Pharr, "An improved technique for determining hardness and elastic modulus using load and displacement sensing indentation experiments," *Journal of Materials Research,* vol. 7, no. 6, pp. 1564-1583, 1992, doi: 10.1557/jmr.1992.1564.

[23] S. R. Cohen and E. Kalfon-Cohen, "Dynamic nanoindentation by instrumented nanoindentation and force microscopy: a comparative review," *Beilstein Journal of Nanotechnology,* vol. 4, pp. 815-833, 2013, doi: 10.3762/bjnano.4.93.

[24] I. N. Sneddon, "The relation between load and penetration in the axisymmetric Boussinesq problem for a punch of arbitrary profile," *International journal of engineering science,* vol. 3, no. 1, pp. 47-57, 1965.

[25] J. Hay, P. Agee, and E. Herbert, "CONTINUOUS STIFFNESS MEASUREMENT DURING INSTRUMENTED INDENTATION TESTING," *Experimental Techniques,* vol. 34, no. 3, pp. 86-94, 2010, doi: 10.1111/j.1747-1567.2010.00618.x.

[26] S. Zak, C. O. W. Trost, P. Kreiml, and M. J. Cordill, "Accurate measurement of thin film mechanical properties using nanoindentation," *Journal of Materials Research,* vol. 37, no. 7, pp. 1373-1389, 2022, doi: 10.1557/s43578-022-00541-1.

[27] H. Bückle, "Use of the hardness test to determine other material properties," *The science of hardness testing and its research applications,* vol. 453, 1973.

[28] P. Sudharshan Phani and W. C. Oliver, "A critical assessment of the effect of indentation spacing on the measurement of hardness and modulus using instrumented indentation testing," *Materials & Design,* vol. 164, p. 107563, 2019, doi: 10.1016/j.matdes.2018.107563.

[29] L. E. Samuels and T. O. Mulhearn, "An experimental investigation of the deformed zone associated with indentation hardness impressions," *Journal of the Mechanics and Physics of Solids,* vol. 5, no. 2, pp. 125-134, 1957, doi: 10.1016/0022-5096(57)90056-x.

[30] K. Mohan, N. Shahane, R. Liu, V. Smet, and A. Antoniou, "A Review of Nanoporous Metals in Interconnects," *JOM,* vol. 70, no. 10, pp. 2192-2204, 2018, doi: 10.1007/s11837-018-3081-z.

[31] X. Xiao, P. Si, and E. Magner, "An overview of dealloyed nanoporous gold in bioelectrochemistry," *Bioelectrochemistry,* vol. 109, pp. 117-126, 2016, doi: 10.1016/j.bioelechem.2015.12.008.

[32] T. Juarez, J. Biener, J. Weissmüller, and A. M. Hodge, "Nanoporous Metals with Structural Hierarchy: A Review," *Advanced Engineering Materials,* vol. 19, no. 12, p. 1700389, 2017, doi: 10.1002/adem.201700389.

[33] I. Gibson and M. F. Ashby, "The mechanics of three-dimensional cellular materials," *Proceedings of the royal society of London. A. Mathematical and physical sciences,* vol. 382, no. 1782, pp. 43-59, 1982.

[34] L. J. Gibson, M. F. Ashby, G. Schajer, and C. Robertson, "The mechanics of two-dimensional cellular materials," *Proceedings of the Royal Society of London. A. Mathematical and Physical Sciences,* vol. 382, no. 1782, pp. 25-42, 1982.

[35] M. F. Ashby, "The Properties of Foams and Lattices," *Philosophical Transactions: Mathematical, Physical and Engineering Sciences,* 2006.

[36] L. J. Gibson, "Mechanical Behavior of Metallic Foams," *Annual Review of Materials Science,* vol. 30, no. 1, pp. 191-227, 2000, doi: 10.1146/annurev.matsci.30.1.191.

[37] H.-J. Jin, J. Weissmüller, and D. Farkas, "Mechanical response of nanoporous metals: A story of size, surface stress, and severed struts," *Mrs Bulletin,* vol. 43, no. 1, pp. 35-42, 2018.

[38] A. Hodge, R. Doucette, M. Biener, J. Biener, O. Cervantes, and A. Hamza, "Ag effects on the elastic modulus values of nanoporous Au foams," *Journal of Materials Research,* vol. 24, no. 4, pp. 1600-1606, 2009.

[39] M. F. Ashby and L. J. Gibson, "Cellular solids: structure and properties," *Press Syndicate of the University of Cambridge, Cambridge, UK,* pp. 175-231, 1997.

[40] N. J. Briot, M. Kosmidou, R. Dingreville, K. Hattar, and T. J. Balk, "In situ TEM investigation of self-ion irradiation of nanoporous gold," *Journal of Materials Science,* vol. 54, no. 9, pp. 7271-7287, 2019, doi: 10.1007/s10853-019-03385-z.

[41] N. Mameka, K. Wang, J. Markmann, E. T. Lilleodden, and J. Weissmüller, "Nanoporous Gold—Testing Macro-scale Samples to Probe Small-scale Mechanical Behavior," *Materials Research Letters,* vol. 4, no. 1, pp. 27-36, 2016, doi: 10.1080/21663831.2015.1094679.

[42] T. J. Balk, C. Eberl, Y. Sun, K. J. Hemker, and D. S. Gianola, "Tensile and compressive microspecimen testing of bulk nanoporous gold," *JOM,* vol. 61, no. 12, pp. 26-31, 2009, doi: 10.1007/s11837-009-0176-6.

[43] R. N. Viswanath, V. A. Chirayath, R. Rajaraman, G. Amarendra, and C. S. Sundar, "Ligament coarsening in nanoporous gold: Insights from positron annihilation study," *Applied Physics Letters,* vol. 102, no. 25, p. 253101, 2013, doi: 10.1063/1.4812290.

[44] N. Briot, "NANOMECHANICAL AND SCALING BEHAVIOR OF NANOPOROUS GOLD," Chemical and Materials Engineering, 2015.

[45] N. J. Briot and T. J. Balk, "Focused ion beam characterization of deformation resulting from nanoindentation of nanoporous gold," *MRS Communications,* vol. 8, no. 1, pp. 132-136, 2018.

[46] J. Biener *et al.*, "Size Effects on the Mechanical Behavior of Nanoporous Au," *Nano Letters,* vol. 6, no. 10, pp. 2379-2382, 2006, doi: 10.1021/nl061978i.

[47] V. Zielasek *et al.*, "Gold Catalysts: Nanoporous Gold Foams," *Angewandte Chemie International Edition,* vol. 45, no. 48, pp. 8241-8244, 2006, doi: 10.1002/anie.200602484.

[48] X. Zhang and Y. Ding, "Unsupported nanoporous gold for heterogeneous catalysis," *Catalysis Science & Technology,* vol. 3, no. 11, p. 2862, 2013, doi: 10.1039/c3cy00241a.

[49] J. Rouquerol *et al.*, "Recommendations for the characterization of porous solids (Technical Report)," *Pure and applied chemistry,* vol. 66, no. 8, pp. 1739-1758, 1994.

[50] H. J. Jin, D. Kramer, Y. Ivanisenko, and J. Weissmüller, "Macroscopically Strong Nanoporous Pt Prepared by Dealloying," *Advanced Engineering Materials,* vol. 9, no. 10, pp. 849-854, 2007, doi: 10.1002/adem.200700177.

[51] H. Li and A. Misra, "A dramatic increase in the strength of a nanoporous Pt–Ni alloy induced by annealing," *Scripta Materialia,* vol. 63, no. 12, pp. 1169-1172, 2010, doi: 10.1016/j.scriptamat.2010.08.026.

[52] M. Hieda, R. Garcia, M. Dixon, T. Daniel, D. Allara, and M. H. W. Chan, "Ultrasensitive quartz crystal microbalance with porous gold electrodes," *Applied Physics Letters,* vol. 84, no. 4, pp. 628-630, 2004, doi: 10.1063/1.1643531.

[53] M. Haruta, "New Generation of Gold Catalysts: Nanoporous Foams and Tubes—Is Unsupported Gold Catalytically Active?," *ChemPhysChem,* vol. 8, no. 13, pp. 1911-1913, 2007, doi: 10.1002/cphc.200700325.

[54] Y. Ding, M. Chen, and J. Erlebacher, "Metallic Mesoporous Nanocomposites for Electrocatalysis," *Journal of the American Chemical Society,* vol. 126, no. 22, pp. 6876-6877, 2004, doi: 10.1021/ja0320119.

[55] M. D. Scanlon *et al.*, "Characterization of Nanoporous Gold Electrodes for Bioelectrochemical Applications," *Langmuir,* vol. 28, no. 4, pp. 2251-2261, 2012, doi: 10.1021/la202945s.

[56] A. Leitner *et al.*, "Interface dominated mechanical properties of ultra-fine grained and nanoporous Au at elevated temperatures," *Acta materialia,* vol. 121, pp. 104-116, 2016.

[57] E. M. Bringa *et al.*, "Are Nanoporous Materials Radiation Resistant?," *Nano Letters,* vol. 12, no. 7, pp. 3351-3355, 2012, doi: 10.1021/nl201383u.

[58] S. Kuwano-Nakatani *et al.*, "Environment-Sensitive Thermal Coarsening of Nanoporous Gold," *MATERIALS TRANSACTIONS,* vol. 56, no. 4, pp. 468-472, 2015, doi: 10.2320/matertrans.mf201403.

[59] Y. Sun, S. A. Burger, and T. J. Balk, "Controlled ligament coarsening in nanoporous gold by annealing in vacuum versus nitrogen," *Philosophical Magazine,* vol. 94, no. 10, pp. 1001-1011, 2014, doi: 10.1080/14786435.2013.876113.

[60] N. J. Briot, T. Kennerknecht, C. Eberl, and T. J. Balk, "Mechanical properties of bulk single crystalline nanoporous gold investigated by millimetre-scale tension and compression testing," *Philosophical Magazine,* vol. 94, no. 8, pp. 847-866, 2014, doi: 10.1080/14786435.2013.868944.

[61] L. He, M. Hadi, H. Liu, and N. Abdolrahim, "Mechanism of coarsening and deformation behavior of nanoporous Cu with varying relative density," *Journal of*

Materials Research, vol. 35, no. 19, pp. 2620-2628, 2020, doi: 10.1557/jmr.2020.68.

[62] N. J. Briot and T. J. Balk, "Developing scaling relations for the yield strength of nanoporous gold," *Philosophical Magazine,* vol. 95, no. 27, pp. 2955-2973, 2015.

[63] G. N. Haidemenopoulos, *Physical metallurgy: principles and design*. CRC Press, 2018.

[64] M. Shaw and T. Sata, "The plastic behavior of cellular materials," *International Journal of Mechanical Sciences,* vol. 8, no. 7, pp. 469-478, 1966.

[65] L. H. Qian and M. W. Chen, "Ultrafine nanoporous gold by low-temperature dealloying and kinetics of nanopore formation," vol. 91, no. 8, p. 083105, 2007, doi: 10.1063/1.2773757.

[66] Z. Lu *et al.*, "Three-dimensional bicontinuous nanoporous materials by vapor phase dealloying," *Nature Communications,* vol. 9, no. 1, 2018, doi: 10.1038/s41467-017-02167-y.

[67] D. R. Peale and B. H. Cooper, "Adsorbate-promoted mass flow on the gold (111) surface observed by scanning tunneling microscopy," *Journal of Vacuum Science & Technology A: Vacuum, Surfaces, and Films,* vol. 10, no. 4, pp. 2210-2215, 1992, doi: 10.1116/1.578006.

[68] Y. Sun and T. J. Balk, "Evolution of Structure, Composition, and Stress in Nanoporous Gold Thin Films with Grain-Boundary Cracks," *Metallurgical and Materials Transactions A,* vol. 39, no. 11, pp. 2656-2665, 2008, doi: 10.1007/s11661-008-9625-z.

[69] H.-J. Jin and J. Weissmüller, "Bulk Nanoporous Metal for Actuation," *Advanced Engineering Materials,* vol. 12, no. 8, pp. 714-723, 2010, doi: 10.1002/adem.200900329.

[70] A. J. Forty, "Micromorphological Studies of the Corrosion of Gold Alloys," vol. 14, no. 1, pp. 25-35, 1981, doi: 10.1007/bf03216556.

[71] X. Wang, Z. Qi, C. Zhao, W. Wang, and Z. Zhang, "Influence of Alloy Composition and Dealloying Solution on the Formation and Microstructure of Monolithic Nanoporous Silver through Chemical Dealloying of Al−Ag Alloys," *The Journal of Physical Chemistry C,* vol. 113, no. 30, pp. 13139-13150, 2009, doi: 10.1021/jp902490u.

[72] J. Erlebacher, "An Atomistic Description of Dealloying," *Journal of The Electrochemical Society,* vol. 151, no. 10, p. C614, 2004, doi: 10.1149/1.1784820.

[73] Q. Sang, S. Hao, J. Han, and Y. Ding, "Dealloyed nanoporous materials for electrochemical energy conversion and storage," *EnergyChem,* p. 100069, 2022.

[74] U. Helmersson, M. Lattemann, J. Bohlmark, A. P. Ehiasarian, and J. T. Gudmundsson, "Ionized physical vapor deposition (IPVD): A review of technology and applications," *Thin Solid Films,* vol. 513, no. 1-2, pp. 1-24, 2006, doi: 10.1016/j.tsf.2006.03.033.

[75] S. M. Rossnagel, "Thin film deposition with physical vapor deposition and related technologies," *Journal of Vacuum Science & Technology A: Vacuum, Surfaces, and Films,* vol. 21, no. 5, pp. S74-S87, 2003, doi: 10.1116/1.1600450.

[76] A. Baptista, F. Silva, J. Porteiro, J. Míguez, G. Pinto, and L. Fernandes, "On the physical vapour deposition (PVD): evolution of magnetron sputtering processes for industrial applications," *Procedia Manufacturing,* vol. 17, pp. 746-757, 2018.

[77] J. A. Smeltzer *et al.*, "Achieving ultra hard refractory multi-principal element alloys via mechanical alloying," *Materials Science and Engineering: A,* vol. 763, p. 138140, 2019.

[78] O. N. Senkov, D. B. Miracle, K. J. Chaput, and J.-P. Couzinie, "Development and exploration of refractory high entropy alloys—A review," *Journal of Materials Research,* vol. 33, no. 19, pp. 3092-3128, 2018, doi: 10.1557/jmr.2018.153.

[79] D. Miracle, J. Miller, O. Senkov, C. Woodward, M. Uchic, and J. Tiley, "Exploration and Development of High Entropy Alloys for Structural Applications," *Entropy,* vol. 16, no. 1, pp. 494-525, 2014, doi: 10.3390/e16010494.

[80] W. Jiang, S. Yuan, Y. Cao, Y. Zhang, and Y. Zhao, "Mechanical properties and deformation mechanisms of a Ni2Co1Fe1V0.5Mo0.2 medium-entropy alloy at elevated temperatures," *Acta Materialia,* vol. 213, p. 116982, 2021, doi: 10.1016/j.actamat.2021.116982.

[81] C. M. Liu, H. M. Wang, S. Q. Zhang, H. B. Tang, and A. L. Zhang, "Microstructure and oxidation behavior of new refractory high entropy alloys," *Journal of Alloys and Compounds,* vol. 583, pp. 162-169, 2014, doi: 10.1016/j.jallcom.2013.08.102.

[82] O. N. Senkov, C. Woodward, and D. B. Miracle, "Microstructure and Properties of Aluminum-Containing Refractory High-Entropy Alloys," *JOM,* vol. 66, no. 10, pp. 2030-2042, 2014, doi: 10.1007/s11837-014-1066-0.

[83] Z. Leong, U. Ramamurty, and T. L. Tan, "Microstructural and compositional design principles for Mo-V-Nb-Ti-Zr multi-principal element alloys: a high-throughput first-principles study," *Acta Materialia,* vol. 213, p. 116958, 2021, doi: 10.1016/j.actamat.2021.116958.

[84] O. N. Senkov, J. D. Miller, D. B. Miracle, and C. Woodward, "Accelerated exploration of multi-principal element alloys with solid solution phases," *Nature Communications,* vol. 6, no. 1, p. 6529, 2015, doi: 10.1038/ncomms7529.

[85] B. Cantor, "Multicomponent high-entropy Cantor alloys," *Progress in Materials Science*, vol. 120, p. 100754, 2021, doi: 10.1016/j.pmatsci.2020.100754.

[86] C.-C. Chen, K. M. Koh, and K. Khee-Meng, *Principles and techniques in combinatorics*. World Scientific, 1992.

[87] Y. Zhang *et al.*, "Microstructures and properties of high-entropy alloys," *Progress in Materials Science*, vol. 61, pp. 1-93, 2014, doi: 10.1016/j.pmatsci.2013.10.001.

[88] S. El-Hadad, "High Entropy Alloys: The Materials of Future," *International Journal of Materials Technology and Innovation*, vol. 2, no. 1, pp. 67-84, 2022, doi: 10.21608/ijmti.2022.118565.1046.

[89] J.-W. Yeh, "Recent Progress in High Entropy Alloys," *European Journal of Control*, 2006.

[90] J.-W. Yeh, S.-Y. Chang, Y.-D. Hong, S.-K. Chen, and S.-J. Lin, "Anomalous decrease in X-ray diffraction intensities of Cu–Ni–Al–Co–Cr–Fe–Si alloy systems with multi-principal elements," *Materials chemistry and physics*, vol. 103, no. 1, pp. 41-46, 2007.

[91] Y. Zhang, X. Yang, and P. K. Liaw, "Alloy Design and Properties Optimization of High-Entropy Alloys," *JOM*, vol. 64, no. 7, pp. 830-838, 2012, doi: 10.1007/s11837-012-0366-5.

[92] Y. J. Zhou, Y. Zhang, Y. L. Wang, and G. L. Chen, "Solid solution alloys of AlCoCrFeNiTix with excellent room-temperature mechanical properties," *Applied Physics Letters*, vol. 90, no. 18, p. 181904, 2007, doi: 10.1063/1.2734517.

[93] Y. Zhang, Y. Zhou, X. Hui, M. Wang, and G. Chen, "Minor alloying behavior in bulk metallic glasses and high-entropy alloys," *Science in China Series G: Physics, Mechanics and Astronomy*, vol. 51, no. 4, pp. 427-437, 2008, doi: 10.1007/s11433-008-0050-5.

[94] S. Ranganathan, "Alloyed pleasures: Multimetallic cocktails," *Current science*, vol. 85, no. 10, pp. 1404-1406, 2003.

[95] X. Wang, Y. Zhang, Y. Qiao, and G. Chen, "Novel microstructure and properties of multicomponent CoCrCuFeNiTix alloys," *Intermetallics*, vol. 15, no. 3, pp. 357-362, 2007.

[96] S. Singh, N. Wanderka, B. S. Murty, U. Glatzel, and J. Banhart, "Decomposition in multi-component AlCoCrCuFeNi high-entropy alloy," *Acta Materialia*, vol. 59, no. 1, pp. 182-190, 2011/01/01/ 2011, doi: https://doi.org/10.1016/j.actamat.2010.09.023.

[97] M. C. Troparevsky, J. R. Morris, M. Daene, Y. Wang, A. R. Lupini, and G. M. Stocks, "Beyond atomic sizes and Hume-Rothery rules: understanding and predicting high-entropy alloys," *JOM,* vol. 67, pp. 2350-2363, 2015.

[98] O. N. Senkov, S. V. Senkova, and C. Woodward, "Effect of aluminum on the microstructure and properties of two refractory high-entropy alloys," *Acta Materialia,* vol. 68, pp. 214-228, 2014, doi: 10.1016/j.actamat.2014.01.029.

[99] Y. Tang *et al.*, "A review on the dynamic-mechanical behaviors of high-entropy alloys," *Progress in Materials Science,* p. 101090, 2023.

[100] G. R. Johnson and W. H. Cook, "Fracture characteristics of three metals subjected to various strains, strain rates, temperatures and pressures," *Engineering fracture mechanics,* vol. 21, no. 1, pp. 31-48, 1985.

[101] X. Zhong *et al.*, "Mechanical properties and microstructure of the Al0. 3CoCrFeNiTi0. 3 high entropy alloy under dynamic compression," *Materials Science and Engineering: A,* vol. 812, p. 141147, 2021.

[102] F. J. Zerilli and R. W. Armstrong, "Dislocation-mechanics-based constitutive relations for material dynamics calculations," *Journal of applied physics,* vol. 61, no. 5, pp. 1816-1825, 1987.

[103] R. Liang and A. S. Khan, "A critical review of experimental results and constitutive models for BCC and FCC metals over a wide range of strain rates and temperatures," *International Journal of Plasticity,* vol. 15, no. 9, pp. 963-980, 1999.

[104] T.-W. Liu, T. Li, and L.-H. Dai, "Near-Equiatomic μ Phase in Self-Sharpening Tungsten-Based High-Entropy Alloys," *Metals,* vol. 12, no. 7, p. 1130, 2022, doi: 10.3390/met12071130.

[105] S. Natarajan, V. Gopalan, R. A. A. Rajan, and C.-P. Jen, "Effect of rare earth metals (Y, La) and refractory metals (Mo, Ta, Re) to improve the mechanical properties of W–Ni–Fe Alloy—A Review," *Materials,* vol. 14, no. 7, p. 1660, 2021.

[106] X.-F. Liu *et al.*, "“Self-sharpening” tungsten high-entropy alloy," *Acta Materialia,* vol. 186, pp. 257-266, 2020, doi: 10.1016/j.actamat.2020.01.005.

[107] T. Li, J. Chen, F. Chen, Y. Chen, and L. Dai, "Enhancing plasticity of ‘self-sharpening’tungsten high-entropy alloy via tailoring μ-precipitation," *Materials Research Express,* vol. 10, no. 7, p. 076511, 2023.

[108] H. Chen, X. Zhang, C. Liu, W. Xiong, M. Tan, and L.-H. Dai, "Theoretical analysis for self-sharpening penetration of tungsten high-entropy alloy into steel target with elevated impact velocities," *Acta Mechanica Sinica,* 2021, doi: 10.1007/s10409-021-01086-y.

[109] D. P. Arfsten, K. R. Still, and G. D. Ritchie, "A review of the effects of uranium and depleted uranium exposure on reproduction and fetal development," *Toxicology and industrial health,* vol. 17, no. 5-10, pp. 180-191, 2001.

[110] D.-K. Kim, S. Lee, and W. Hyung Baek, "Microstructural study of adiabatic shear bands formed by high-speed impact in a tungsten heavy alloy penetrator," *Materials Science and Engineering: A,* vol. 249, no. 1-2, pp. 197-205, 1998, doi: 10.1016/s0921-5093(98)00565-6.

[111] K. Jiang *et al.*, "Adiabatic shear localization induced by dynamic recrystallization in an FCC high entropy alloy," *International Journal of Plasticity,* vol. 162, p. 103550, 2023.

[112] D. Grady, "Properties of an adiabatic shear-band process zone," *Journal of the Mechanics and Physics of Solids,* vol. 40, no. 6, pp. 1197-1215, 1992.

[113] P. Landau, S. Osovski, A. Venkert, V. Gärtnerová, and D. Rittel, "The genesis of adiabatic shear bands," *Scientific Reports,* vol. 6, no. 1, p. 37226, 2016, doi: 10.1038/srep37226.

[114] S. Nemat-Nasser, Y.-F. Li, and J. B. Isaacs, "Experimental/ computational evaluation of flow stress at high strain rates with application to adiabatic shear banding," *Mechanics of Materials,* vol. 17, no. 2-3, pp. 111-134, 1994, doi: 10.1016/0167-6636(94)90053-1.

[115] B. Dodd and Y. Bai, *Adiabatic shear localization: frontiers and advances*. Elsevier, 2012.

[116] H.-h. Chen, X.-f. Zhang, L.-h. Dai, C. Liu, W. Xiong, and M.-t. Tan, "Experimental study on WFeNiMo high-entropy alloy projectile penetrating semi-infinite steel target," *Defence Technology,* vol. 18, no. 8, pp. 1470-1482, 2022.

[117] C. K. C. Lieou and C. A. Bronkhorst, "Dynamic recrystallization in adiabatic shear banding: Effective-temperature model and comparison to experiments in ultrafine-grained titanium," *International Journal of Plasticity,* vol. 111, pp. 107-121, 2018, doi: 10.1016/j.ijplas.2018.07.011.

[118] G. Dirras *et al.*, "Mechanical behavior and microstructure of Ti20Hf20Zr20Ta20Nb20 high-entropy alloy loaded under quasi-static and dynamic compression conditions," *Materials Characterization,* vol. 111, pp. 106-113, 2016, doi: 10.1016/j.matchar.2015.11.018.

[119] B. Gwalani *et al.*, "Dynamic Shear Deformation of a Precipitation Hardened Al0.7CoCrFeNi Eutectic High-Entropy Alloy Using Hat-Shaped Specimen Geometry," *Entropy,* vol. 22, no. 4, p. 431, 2020, doi: 10.3390/e22040431.

[120] W. J. Kim, H. T. Jeong, H. K. Park, K. Park, T. W. Na, and E. Choi, "The effect of Al to high-temperature deformation mechanisms and processing maps of

Al0.5CoCrFeMnNi high entropy alloy," *Journal of Alloys and Compounds*, vol. 802, pp. 152-165, 2019, doi: 10.1016/j.jallcom.2019.06.099.

[121] Z. Li, S. Zhao, S. M. Alotaibi, Y. Liu, B. Wang, and M. A. Meyers, "Adiabatic shear localization in the CrMnFeCoNi high-entropy alloy," *Acta Materialia*, vol. 151, pp. 424-431, 2018/06/01/ 2018, doi: https://doi.org/10.1016/j.actamat.2018.03.040.

[122] M. R. Rahul, S. Samal, S. Venugopal, and G. Phanikumar, "Experimental and finite element simulation studies on hot deformation behaviour of AlCoCrFeNi2.1 eutectic high entropy alloy," *Journal of Alloys and Compounds*, vol. 749, pp. 1115-1127, 2018, doi: 10.1016/j.jallcom.2018.03.262.

[123] K. Ren *et al.*, "Compression properties and impact energy release characteristics of TiZrNbV high-entropy alloy," *Materials Science and Engineering: A*, vol. 827, p. 142074, 2021, doi: 10.1016/j.msea.2021.142074.

[124] B. Wang, C. Wang, B. Liu, and X. Zhang, "Dynamic Mechanical Properties and Microstructure of an (Al0.5CoCrFeNi)0.95Mo0.025C0.025 High Entropy Alloy," *Entropy*, vol. 21, no. 12, p. 1154, 2019, doi: 10.3390/e21121154.

[125] S. Yang and Y. Yang, "Thermodynamics-kinetics of twinning/martensitic transformation in Fe50Mn30Co10Cr10 high-entropy alloy during adiabatic shearing," *Scripta Materialia*, vol. 181, pp. 115-120, 2020, doi: 10.1016/j.scriptamat.2020.02.024.

[126] S. Zhou *et al.*, "High entropy alloy: A promising matrix for high-performance tungsten heavy alloys," *Journal of Alloys and Compounds*, vol. 777, pp. 1184-1190, 2019, doi: 10.1016/j.jallcom.2018.11.089.

[127] C. Edgerley, L. Smith, and C. Wilford, "Electric metal melting-a review," *Power Engineering Journal*, vol. 2, no. 2, pp. 83-92, 1988.

[128] H. Khan, A. S. Yerramilli, A. D'Oliveira, T. L. Alford, D. C. Boffito, and G. S. Patience, "Experimental methods in chemical engineering: X-ray diffraction spectroscopy— <scp>XRD</scp>," *The Canadian Journal of Chemical Engineering*, vol. 98, no. 6, pp. 1255-1266, 2020, doi: 10.1002/cjce.23747.

[129] A. A. Bunaciu, E. G. UdriȘTioiu, and H. Y. Aboul-Enein, "X-ray diffraction: instrumentation and applications," *Critical reviews in analytical chemistry*, vol. 45, no. 4, pp. 289-299, 2015.

[130] D. Ferguson, W. Chen, T. Bonesteel, and J. Vosburgh, "A look at physical simulation of metallurgical processes, past, present and future," *Materials Science and Engineering: A*, vol. 499, no. 1-2, pp. 329-332, 2009.

[131] P. Bereczki, B. Fekete, V. Szombathelyi, and F. Misjak, "Different Applications of the Gleeble Thermal–Mechanical Simulator in Material Testing, Technology

Optimization, and Process Modeling," *Materials Performance and Characterization*, vol. 4, p. MPC20150006, 07/20 2015, doi: 10.1520/MPC20150006.

VITA

Kerry Baker was born in Fairfax, Va. She graduated from Bucknell University in 2018 with a Bachelor of Science degree in Chemical Engineering. She joined Dr. T. John Balk's research group at the University of Kentucky in 2018 to pursue a Ph.D. in Materials Science and Engineering.

Peer-Reviews Papers

1. **Baker, K.A.**, Balk, T.J. Optimal indent spacing for instrumented nanoindentation of nanoporous gold. MRS Communications (2023).